Comparison of the Geomechanical behavior of sandstones from different reservoirs in northern Europe and North Sea

Stress history and reservoir pressure project for CO_2 storage (SHARP storage project)
MSc Thesis

Barbara Perez Salgado 4802888
Thesis Committee:
Auke Barnhoorn (TU Delft)
Anne Pluymakers (TU Delft)
Allard W. Martinius (Equinor / TU Delft)

Department of Civil Engineering and Geosciences
TUDelft

Friday 7th July, 2023

Contents

1 Acknowledgements

During the period I have been doing this thesis I have experienced many ups and downs, I have faced challenges that have taught me many things about myself and it has tested my limits many times. I am very lucky to say that I have had the unconditional support of my partner Cody Owen who helped me in all moments with his love, care and also patience throughout my entire MSc degree.

Without the guidance of my supervisor Auke Barnhoorn this, literally, wouldn't have been possible, thank you for taming those moments where I didn't see the light at the end of the tunnel.

To Anne Pluymakers and Evgeniia Martuganova for being the confidants of my mental health and inner demons and for giving me the security and push for me to finish this chapter of my life.

Special thanks to Marc Friebel, technician of the Rock Mechanics laboratory, for all the help with the equipment, the great ideas to carry out the experiments, and the awesome environment you bring with you. And, of course, to PhDs Milad Narderloo and Aukje Veltmeijer for their supervision during the experiments and their help. In general, the whole department is filled with incredible people.

Thank you to my friends Lujain, John, Javier, Fiorela, Natalia, and the ones not mentioned who know the struggles and dramas and they have always listened and comforted me with their wise perspectives.

Last but not least, to my family, thank you for all the support even when kilometers separate us and long periods of time without seeing them, they always manage to uplift my spirit.

2 Abstract

Following the 2015 Paris Agreement, many countries are switching from fossil fuel to a more renewable energy supply. However, the CO_2 concentration in the atmosphere keeps increasing which makes difficult to accelerate the transition to a net-zero emission. In 2020, a new record of CO_2 concentration at 412.5 ppm was achieved, the highest concentration seen in the last 800,000 years. For this reason, several technologies have been in the focus to help reducing the amount of CO_2 in the atmosphere as well as keeping it from increasing.

One effective technique in the mitigation of these emissions is called Carbon Capture and Storage (CCS). It is not a new technology, in fact, it has been used in the Oil & Gas industry since the early 1970s for the purpose of Enhanced Oil Recovery (EOR). In very general terms, when CO_2 is mixed with petroleum in the subsurface, its viscosity decreases making it easier to extract more oil. In addition, some of the CO_2 gets trapped in the rock which introduced the idea to use the mechanism to reduce CO_2 concentrations in the atmosphere.

However, this technique is not absent of risks and it is one of the main drawbacks experienced with activities that involved the subsurface, the surrounding uncertainties are too great sometimes. Some of the risks that could be encountered when producing, injecting or drilling a well in the subsurface are: under or over pressurization, leakage, uplift or subsidence, induced seismicity, and fault reactivation. In order to reduce the mentioned risks, geomechanical studies help with the understanding of the rock behavior and their response to applied stresses.

In this thesis, UCS and Triaxial laboratory experiments were carried out to test the geomechanical behavior of different rocks coming from Norway, Denmark and Germany. For the triaxial tests, five different cycles at different and increasing P_c were performed. Doing so, some main insights were obtained: the modulus of elasticity increases with depth and confining pressure more significantly with P_c lower than 30 MPa, and plateauing at higher P_c; the Young's modulus decreases with increasing porosity and increases with increasing cohesion; the P and S waves velocities change when the yield point is surpassed; with low porosity and high cohesion the acoustic velocities are not dependent on the P_c, and vice versa; the SYM and DYM follow similar trends; and the elastic modulus is negatively dependent on the Poisson's ratio.

The information and data obtained from this geomechanical study will be of use to model predictions involving CCS projects to avoid reaching the risks factors mentioned. An example of the lack of knowledge and understanding about rock behavior could be the induced seismicity caused by the extraction of gas from the Groningen gas field. These seismic events acted as a turning point, sparking a necessary shift in perspective and paving the way for a more informed and balanced perception of activities involving the use of the subsurface.

3 Introduction

3.1 Climate change and carbon emissions

Most human activities are fueled by energy, both from fossil fuels and more recently from sustainable energies, such as wind or geothermal energy. However, the latter is not nearly the main energy supply—being only 11% of the primary source (Hannah Ritchie et al. (2022))—and therefore, we currently rely on oil and natural gas for the majority of our energy supply. Since the 1970s, the greenhouse effect became a concern for human welfare; several factors were the source of the rise of carbon dioxide (CO_2) emissions, such as aerosols or the use of fossil fuels (Le Treut et al. (2007)). Since then, the emissions have done nothing but increase which this has been a strong motivation for several technologies to be either developed or improved rapidly. One could say that CO_2 is a natural compound that exists in the atmosphere; however, the issue resides in the quantity rather than its presence. In 2020, a new record of CO_2 concentration at 412.5 ppm was achieved, the highest concentration seen in the last 800,000 years (Figure 3.1 shows data collected up to 2018). and this has been a strong motivation for technologies to be either developed or improved rapidly.

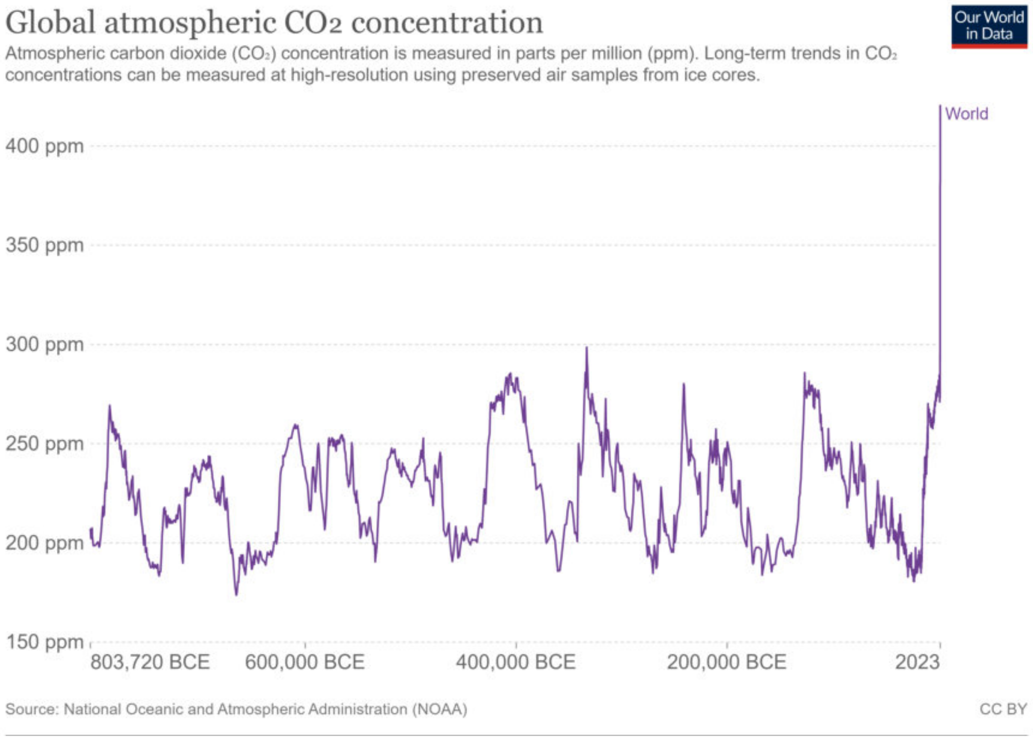

Figure 3.1: Concentration of CO_2 over the past 800,000 years (obtained from the Our World in Data webpage).

The vast amount of scientific information (Pörtner et al. (2022)) pointing towards a rise in the global temperature has not accelerated solutions to combat the climate change, and people became more skeptical of not only conventional but also certain sustainable technologies. This trend results in phenomenon such as NIMBY: 'Not In My Back Yard' (Pol - et al. (2006)). This skepticism is fueled by the lobbying from powerful corporations wanting to maintain the 'status quo' and not helping the transition which ultimately divides the population.

3.2 Carbon capture and storage

Carbon capture and storage (CCS) is one effective technique for mitigating the concentration and emissions of CO_2 involving the utilization of subsurface storage. This approach capitalizes on the valuable knowledge gained through the extraction of fossil fuels. It also enables more sophisticated and comprehensive investigations into various risks associated with gas injection into geological formations. These risks encompass induced seismicity and fault reactivation, ground uplift, as well as potential leakage, among other factors (Oraee-Mirzamani et al.

2013).

Carbon storage projects started in the late 1970s, but not to reduce carbon dioxide in the atmosphere. The main purpose was for Enhanced Oil Recovery (EOR) in the subsurface to reduce the viscosity of oil, thereby making it easier to extract (Martin-Roberts et al. (2021)). Nevertheless, with the introduction of the Paris Agreement in 2015 to keep the global average temperature rise below 2°C above pre-industrial levels (UNFCCC 2015), nowadays, carbon capture and storage projects are being developed all over the world with the purpose of reducing carbon emissions in the atmosphere. In order to reach general acceptance of these projects, knowledge about the subsurface is crucial.

Figure 3.2 shows a sketch of how CCS processes are carried out. In broad terms, the chain starts with industries emitting CO_2 from which it is captured and transported through pipelines to platforms from where it's injected to reservoirs in the subsurface.

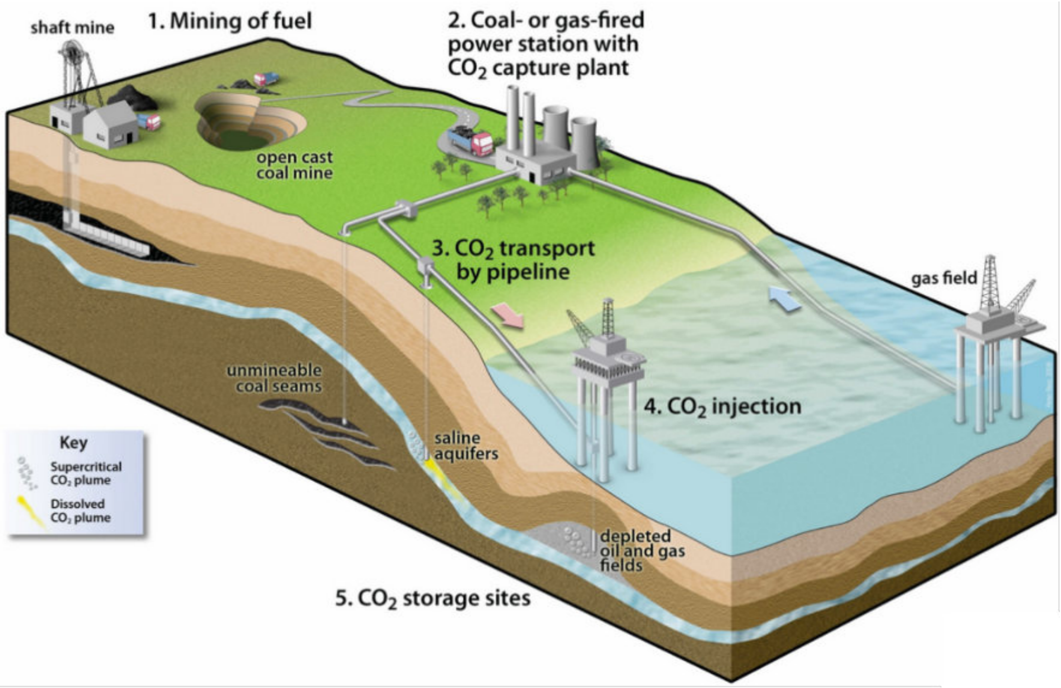

Figure 3.2: Carbon capture and storage process - From emission source to CO_2 injection (Source: Scottish Carbon Capture & Storage).

The potential storage sites should have enough porous volume and good permeability to store the necessary amount of CO_2 at a reasonable rate, and the reservoir and surroundings need to be properly characterized to avoid the risks mentioned earlier (STEMM-CCS 2016).

3.3 Subsurface material modeling

The geological modeling of the subsurface helps to better understand and define the risks caused by injecting a compound into a reservoir. Fault networks, reservoir connectivity, caprock, and tectonic structures can be defined through seismic imaging at a large scale. This information is used partially to characterize a reservoir and to make predictions about the integrity of the subsurface.

Factors such as the history of the different formations, heterogeneity, state of stress, pressure gradient, and temperature are necessary variables to take into account when drilling a well and assessing the risks associated with injection activities. These and many more properties are needed to build a robust and reliable model.

Here is where geomechanics comes into play. Geomechanics focuses on the mechanical behavior of rocks under applied stress, providing insights into their stress state, deformation parameters, failure characteristics, and stiffness. By studying the geomechanical properties of the geological material, it becomes possible to assess their response to injected fluids, potential geomechanical risks such as induced seismicity, and the overall integrity of the subsurface. Geomechanics is a multidisciplinary field highly relevant to various industries, including civil engineering, petroleum engineering, and mining. Its application for injecting compounds into reservoirs allows for a better understanding of the mechanical behavior of rocks and the associated risks, ultimately leading to improved decision-making and risk mitigation strategies (De Jager 2007).

3.4 Research topic

The SHARP project (Stress History And Reservoir Pressure) aims at improving quantification of CO_2 storage containment risks for different reservoirs within the North Sea (Skurtveit et al. (2022)). Several companies are involved: Shell, BP, Equinor; and the research organizations Delft University of Technology (TU Delft) and the Norwegian Geotechnical Institute (NGI). This project is divided into five Work Packages (WP). This thesis is part of WP3: 'Experimental characterization of rock mechanical behaviour, stress history and related monitoring attributes'.
The main objective from Work Package 3 of the SHARP project (Skurtveit et al. 2022) is as follows:

> "The objective of WP3 is the characterization of the rheology and constitutive behaviour of rock material from North Sea caprock and reservoir rock in relation to stress history and operational stress changes and its sensitivity to a selection of observable monitoring attributes, validated against field observations. Laboratory experiments allow for direct quantification of the actual deformation behaviour of the reservoir and overburden rocks and estimates of burial and stress history. Translating the experimentally learned deformation behaviour to field scale in situ conditions and changes requires appropriate upscaling and variational statistics as well as a proper design of relevant and quantifiable attributes that can be extracted from field scale monitoring campaigns."

Specifically for this thesis, the aim is to characterize the geomechanical properties of the rock samples from the different storage sites in the North Sea, as identified by the SHARP project, by performing laboratory experiments.

3.4.1 Research question

For the purpose of carbon storage, what are the rheology and constitutive behavior of sandstones forming the reservoirs in the North Sea?

3.4.2 Research objectives

To answer the research question, the following research objectives are set:

1. Organize sample rock from different sites in Northern Europe.
2. Assess the constitutive behavior of sandstones forming the reservoirs in the North Sea with the following types of tests:
   - Brazilian test.
   - Unconfined compressive strength.
   - Triaxial compression.
   - Active-source acoustics.
3. Explore spatial variability in elastic and inelastic behavior of different reservoirs in the North Sea with and without reaching failure.
4. Quantify of acoustic properties with varying stress conditions.
5. Assess waveform changes due to stress variations.
6. Compare static and dynamic elastic modulus.
7. Assess the effect of the porosity on the geomechanical behavior.

3.5 Thesis outline

This MSc thesis is structured as follows: Sections 2 and 3 helps understanding the context and motivation of this research. Section 4 gives a geological context of the North Sea, where all the samples were obtained and from which wells. Section 5 is dedicated to the materials and methodology used during the laboratory experiments. Sections 6 and 7 are dedicated to the results and the discussion of these results. To finalize, a conclusion with all the main findings is provided in Section 8.
Lastly, the Appendicces section with complementary figures summarizes all the data used in this thesis.

4 Geological setting

The SHARP project is a collective effort to study the mechanical behavior of multiple depleted reservoirs in the North Sea. Not all of the storage sites are targeting the same geological group. For instance, the Netherlands is focusing in the Rotliegend Sandstone (Permian), while Denmark is interested in the Upper Triassic Gassum Fm. (Fm. = Formation). To make a structured and comprehensible reading, firstly, a broad introduction of the geological history of the North Sea is given in order to understand the tectonics and stratigraphy involved in the formation of the present subsurface. To follow, different subsections are focused on the target reservoirs of each location.

4.1 North Sea geological history

The North Sea is situated between Norway (North East), Denmark (East), Germany (South East), the Netherlands (South), Belgium (South) and Great Britain (West). This area comprises the vast majority of the oil and gas fields of western Europe (Kombrink et al. (2022)). Figure 4.1 shows the division of the North Sea, the surrounding countries, and the location of the basins where the main oil and gas fields have been discovered.

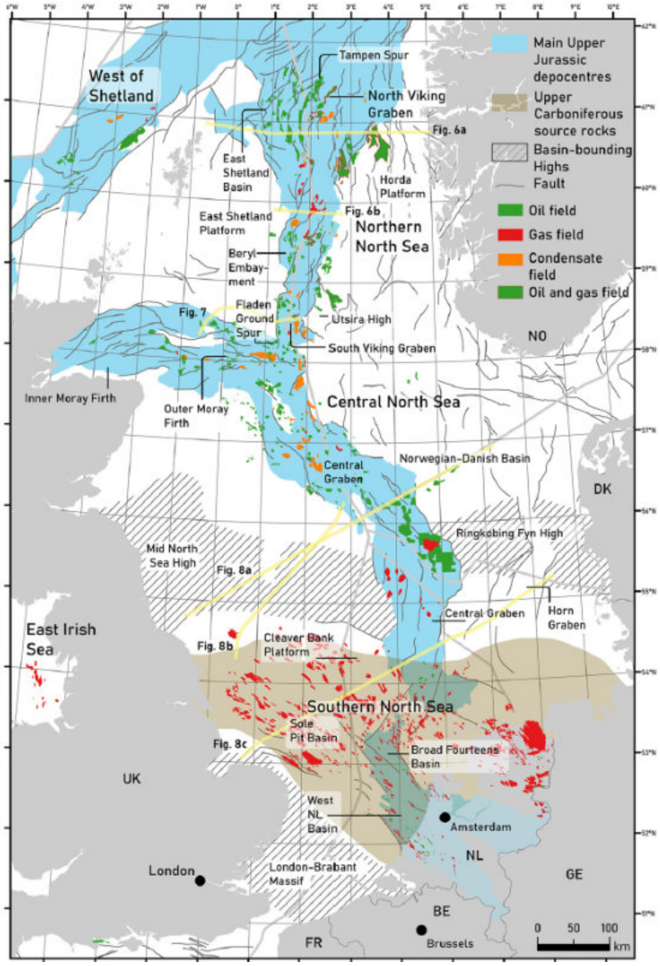

Figure 4.1: Map of the North Sea including the main basins and oil and gas fields (from Patruno et al. (2022)). In addition, it shows the main source rocks linked to those fields which date of the Late Carboniferous and Late Jurassic.

The North Sea tectono-stratigraphic complex history comprises many phases of deformation starting during the middle Paleozoic when Laurentia, Baltica and Avalonia collided and formed the Caledonian Orogeny (see Figure 4.2), shaping the super terraine of Laurussia (Cocks et al. (2006)).

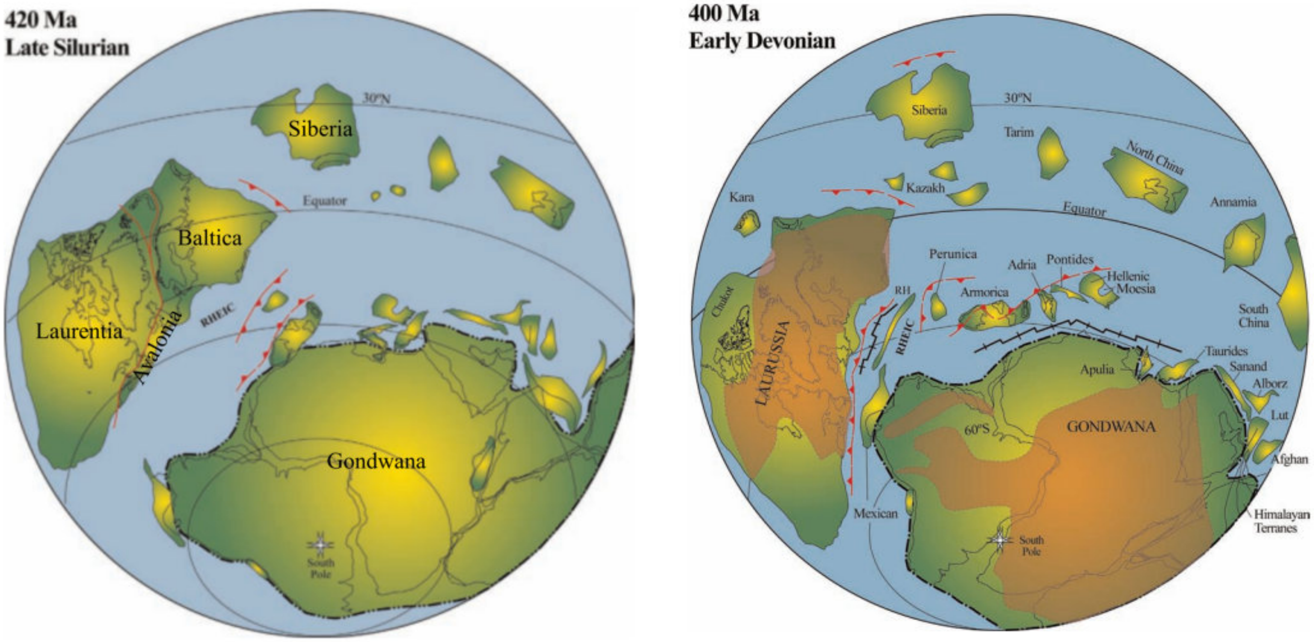

Figure 4.2: Reconstruction of the landmasses in the Late Silurian and early Devonian (modified from Cocks et al. (2006)).

During the Late Carboniferous, a second event of compression (Variscan Orogeny) unified the continents of Laurussia and Gondwana, forming the well known supercontinent of Pangea situated mostly in the South Hemisphere. This collision developed thrust structures verging towards the north which can be observed via outcropping on Southern England in the present (Patruno et al. (2022)). Foreland basins (see Figure 4.3)—developed as a result of this orogenic event—made possible the deposition of source rocks (Westphalian coal) which fed some of the oil and gas reservoirs at later stages.

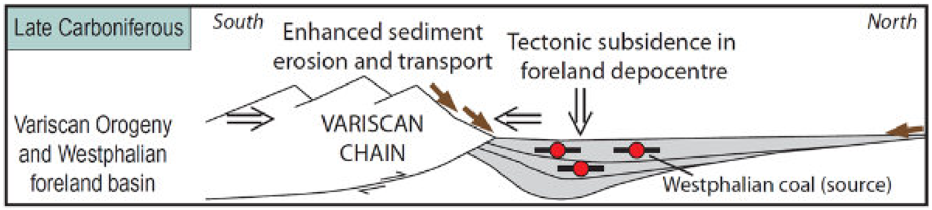

Figure 4.3: Schematic regional situation during the Late Carboniferous in the North Sea basin (from Patruno et al. (2022)).

Thereafter, an intra-plate rifting event occurred during the Permo-Triassic period, creating the Permian Basins which were separated by the North Sea High (see Figure 4.4). The majority of the Permian Basins were occupied by a saline sea called Zechstein Sea where evaporites and siliciclastic sediments were deposited in different environments such as sabkha, aeolian, fluvial and alluvial. These groups of formations are called Rotliegend Group and are of extreme importance for the accumulation of hydrocarbons. Given the position of this region in the Equator and the warm climate, the sea evaporated, thereby depositing a vast amount of evaporites which formed the Zechstein Group (Geluk 2005).

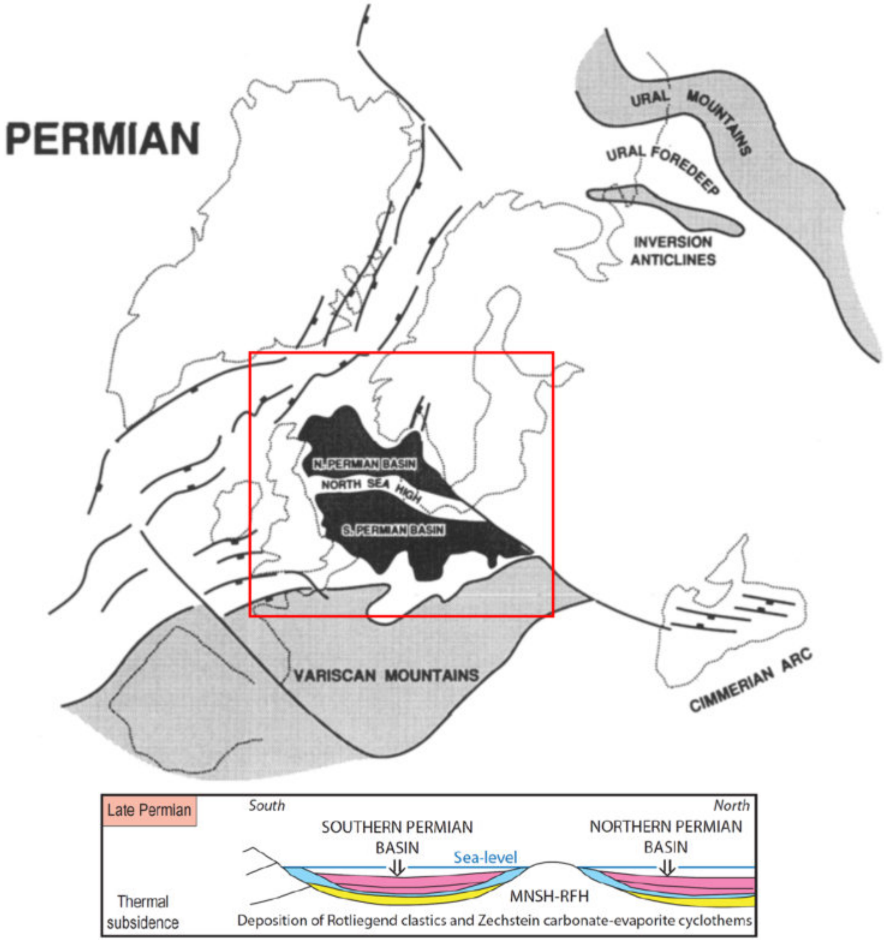

Figure 4.4: Simplified reconstruction of the Permo-Triassic relationship between the basins by Coward (1995) and Patruno et al. (2022), respectively. MNSH refers to the Mid North Sea High.

A thermal uplift during the Mid-Jurassic was followed by the second rifting event in the Late Jurassic period. Three separated basins were formed in the central and northern parts of the North Sea (see Figure 4.1) being the Central Graben, the Moray Firth Graben and the Viking Graben (Fjerseth et al. (1997)). The syn-rift deposition of the Kimmeridge Clay occurs, constituting the major source rock for the North Sea (Cooper et al. (1995)). Once the rifting activity decreased, a thermal subsidence led to the increase in the sea level and the deposition of a thick layer of carbonates (Chalk Group) across the whole basin during the Cretaceous. This subsidence extended to the Early Cenozoic, forming the actual intracratonic sedimentary basin that is the North Sea and the current positions of the continents.

4.2 Norway (Horda Platform)

The northeast structure from which samples arrived is in the Norwegian sector of the North Sea corresponding to the Horda Platform. The Horda Platform is located between the west coast of Norway near Bergen and to the east of the Viking Graben (see Figure 4.5).

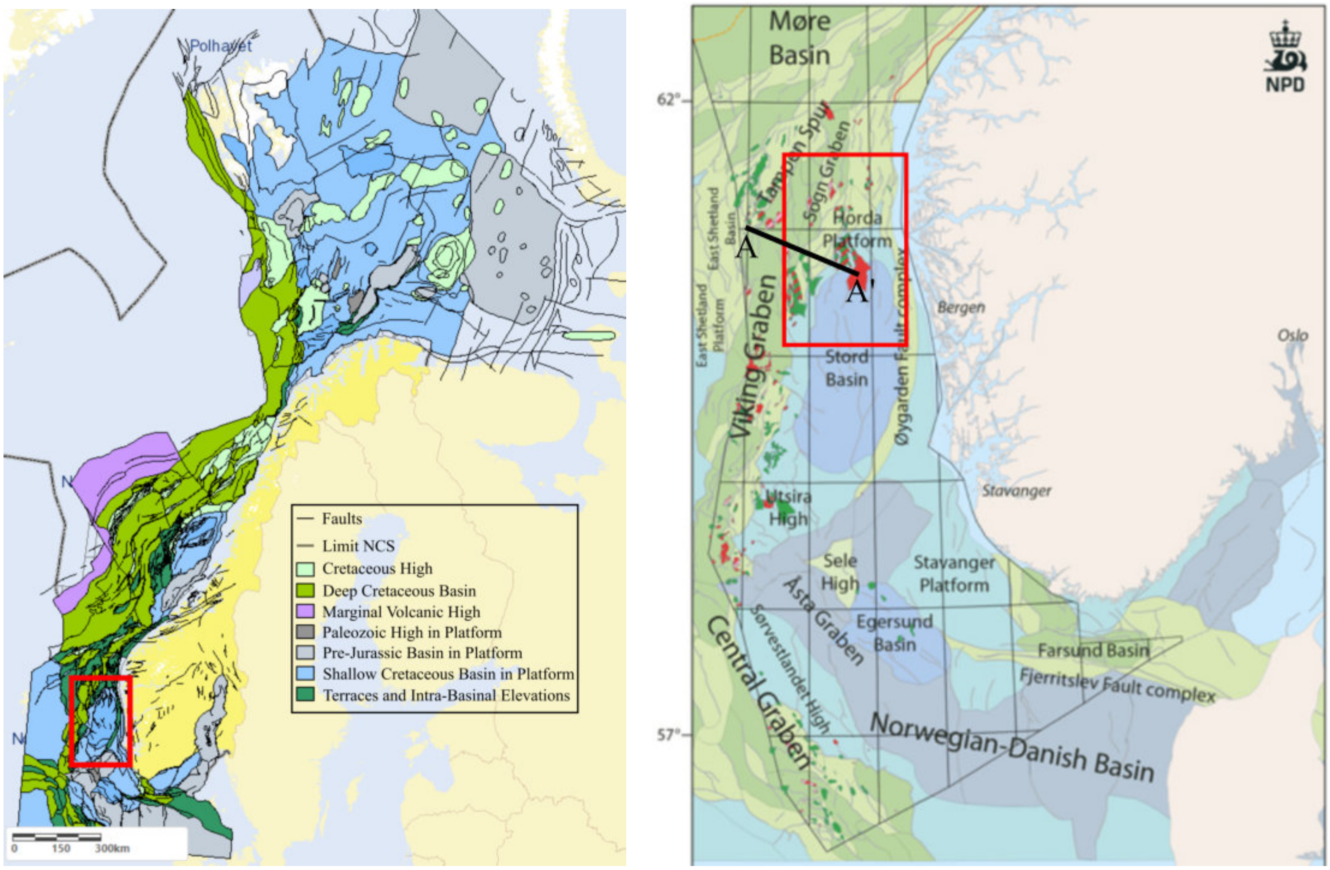

Figure 4.5: Location of the Horda Platform in the Norwegian sector of the North Sea (modified from the Norwegian Petroleum Directorate (NPD)).

The tectono-stratigraphical evolution of the Horda Platform started during the Permo-Triassic rifting. As the cross-section shows (Figure 4.6), there is a large rift system underneath a post-rift sediment cover. The Horda Platform comprises a large half-graben area where the developed faults have massive displacements. During the Middle Jurassic, a subsidence took place where syn-rift deposition of very heterogeneous and poorly sorted sands was framed in a marine to shore-face environmental setting (Stewart et al. (1995)). In the cross-section, the black layer corresponds to the Lower-Mid Jurassic deposits which thin toward the east.

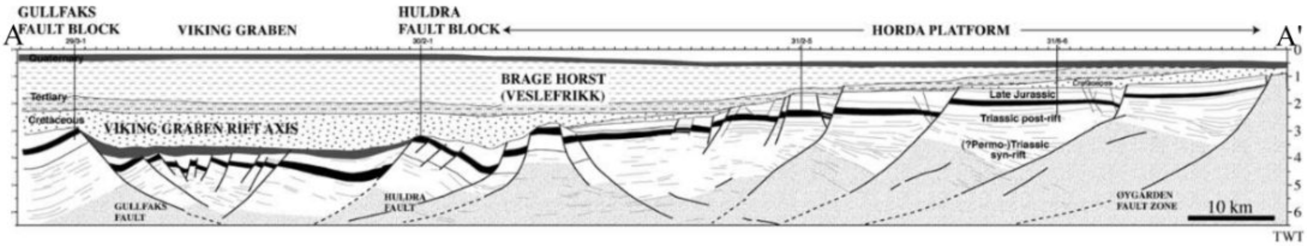

Figure 4.6: General cross-section including the Viking Graben and the Horda Platform (from Fossen et al. (2003)).

These deposits correspond to the target CO_2 storage site, Lower Jurassic Dunlin Group comprising the Johansen and Cook Fm. (Sundal et al. (2016)).

4.3 Denmark (Lisa Structure)

Following Norway, the interested area of study in the Danish sector is located to the east of the North Sea. For the SHARP project, the Lisa Structure corresponds to a potential storage location of CO_2. The targeted formation is called Gassum Fm. which is a primordial reservoir in the Danish Sector. In this specific location (where the red star lies), it amounts to over 180 m of thickness (see Figure 4.7). These sediments were deposited in the Late Triassic (Rhaetian period) as part of the Norwegian-Danish Basin (Olivarius et al. (2019)).

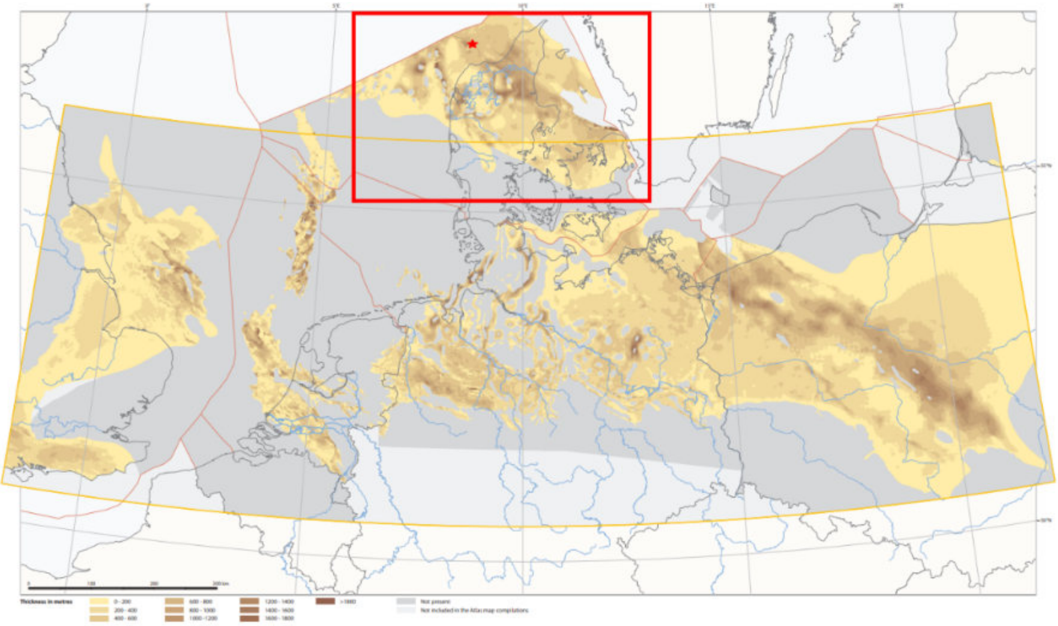

Figure 4.7: Thickness map and distribution of the Gassum Formation in Northern Europe (modified from the Southern Permian Basin Atlas in www.nlog.nl).

In Figure 4.8, the high density of faults covering Denmark can be observed. Near the Lisa Structure to the west, a major fault strikes NW-SE corresponding to the Fjerritslev Fault Zone following to the North Sea towards the Egernsund Basin (Schack Pedersen et al. (2010)) (better shown in Figure 4.5). This complex tectonic setting developed, in its majority, during the Permo-Triassic period.

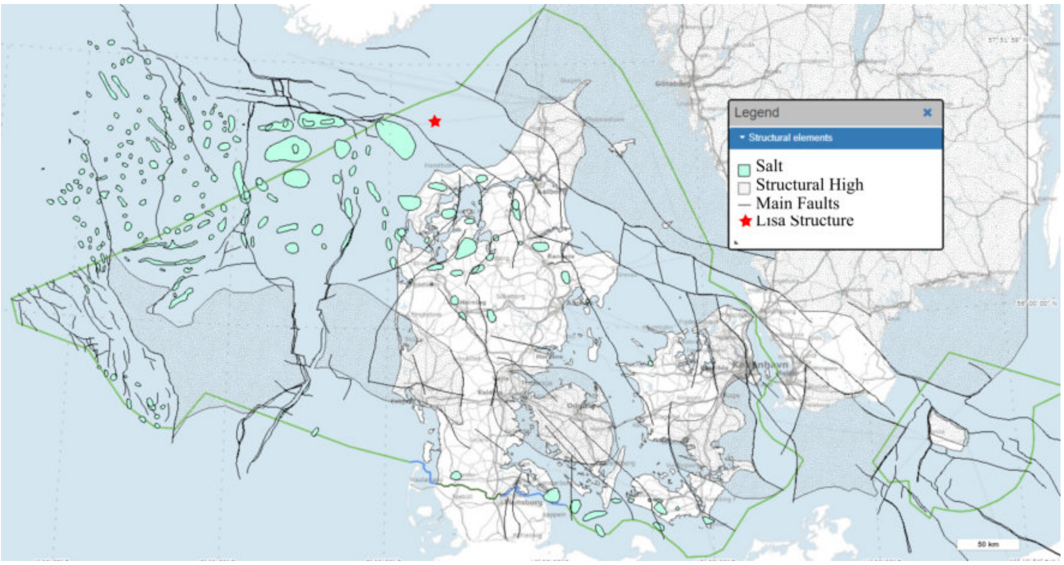

Figure 4.8: Location of the Lisa Structure within the Danish sector of the North Sea (modified from https://data.geus.dk).

4.4 Netherlands / Germany (Analog outcrop)

Part of the SHARP project involves the study of the samples obtained from the Aramis project whose field is located offshore nearby Texel island in the northwest of the Netherlands. The targeted reservoir to study comprises the Upper Rotliegend Group. These formations were deposited in the Southern Permian Basin brought by fluvial and aeolian environments. As Figure 4.9 shows, in the present, these deposits outcrop in the region of Rhineland-Palatinate (Number 2 in the map) in Germany and at about 2 km beneath the subsurface of the locations at the Netherlands (Number 1). Since the samples from location 1 were not available o time, the samples from the quarry were used as analog results.

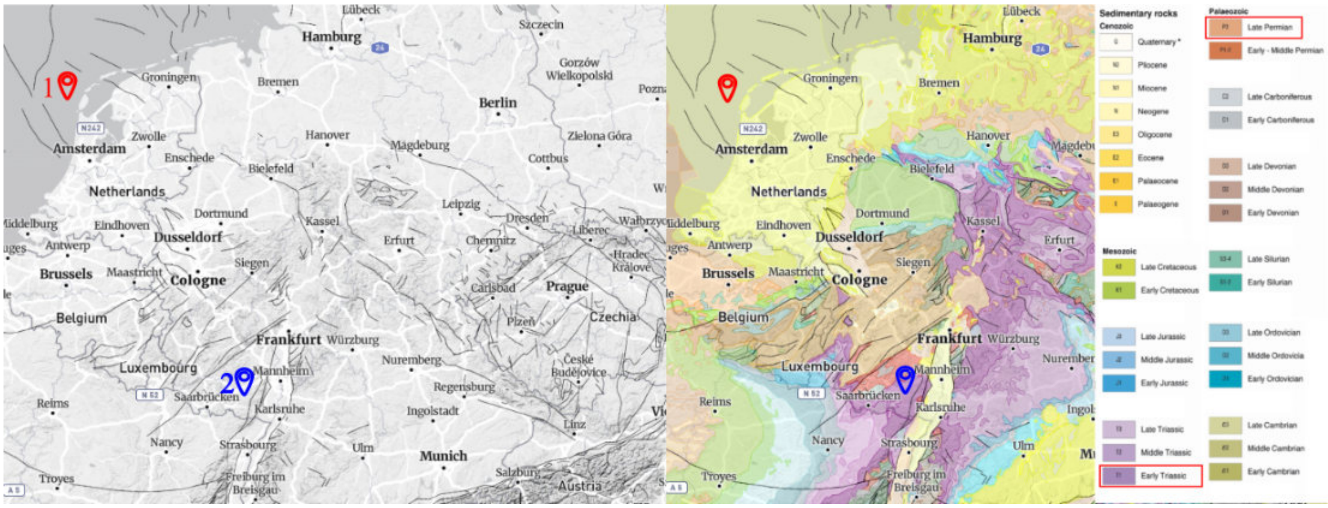

Figure 4.9: Structural and geological maps of the Netherlands and part of Germany. The numbers correspond to the locations of 1) Aramis project field, 2) Quarry (Upper Rotliegend Group outcrop) (modified from https://macrostrat.org).

Figure 4.10 was obtained from the Southern Permian Basin Atlas project which can be found in the NLOG webpage. This project comprises several chapters and this thickness map is from Chapter 7 - Rotliegend. This figure depicts the thickness distribution of the Upper Rotliegend Group on the subsurface of the Netherlands and northern Germany. Near Location no. 1 of Figure 4.9 the thickness can reach up to 400 m which makes the spot very attractive for storage purposes.

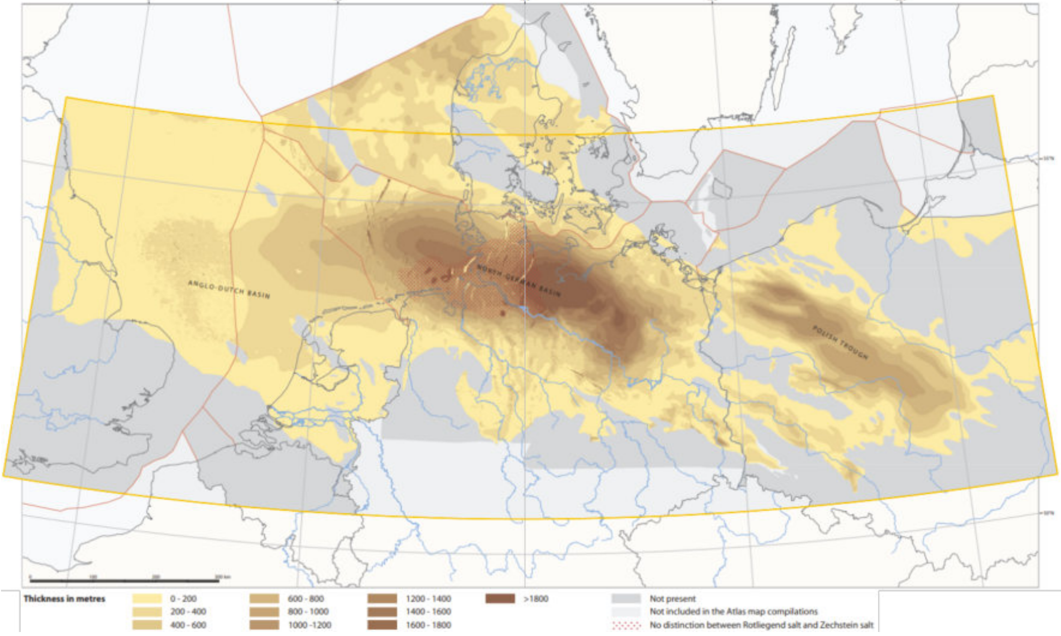

Figure 4.10: Thickness map of the Upper Rotliegend Group (Gast et al. (2010)).

5 Material & Methodology

Samples from the different reservoirs of the North Sea and the outcropping analog onshore in Germany have been received in the laboratory of Rock Mechanics at Delft University of Technology.
The main objective was to obtain from all these samples as much mechanical and acoustic behavioral information as possible. In order to achieve this, several preparations were carried out to the samples received; porosity measurements, micro CT imaging, shear testing with and without confining pressure (P_c), tensile testing, and acoustic measurements. In addition, some of the data were directly obtained from the interested parties which carried out their own experiments.
This section describes the steps to prepare the samples for the tests, the first measurements from this preparation, and the explanation of the laboratory experiments that sought to meet the aims of this thesis.

5.1 Sample preparation

Some of the samples received by the different parties were first taken into several steps of preparation before starting the laboratory experiments. This preparation refers to all of the steps prior to the final test.
Not all of the samples arrived with the desired dimensions; for example, a block of about 30 cm by 30 cm was received from the quarry in Germany. Therefore, the first step was to make plugs. To do this, a coring machine (see Figure G.30) with a diamond bit of 30 mm diameter was used to make cores from the block. Then, with a diamond saw machine (see Figure G.31), the length of the extracted plugs were adjusted. For the triaxial and uniaxial compression tests, the diameter of the samples varied from 25 to 30 mm in diameter and with a length of twice the respective diameter. After cutting each plug, they were dried for at least a day in an oven at 60°C.
Once dried, each plug was massed and the dimensions were properly measured with a precise digital caliper (tolerance of 0.1 mm). The next step was to measure the porosity, which was done with a Helium Ultrapycnometer (see Figure G.33). This device uses helium to fill the connected pores inside the sample. This test takes several runs to show accurate results about the volume and density of the sample. The volume obtained from this equipment and the measured mass and dimensions of the sample were used in a MATLAB script to determine the porosity.
Once these steps were completed, the selected samples for Uniaxial Compression Strength tests were ready.

For Triaxial Compression testing, the selected samples were saturated with tap water from the laboratory in order to bring the sample to the desired conditions to start the experiments. In order to fill as many connected pores as possible, the sample was placed in a vacuum to extract the air filling those pores. Once the samples were in this vacuum for 2 hours at -1 bar, the sample was slowly saturated from the bottom by water (see Figure G.34).
(Visuals of all the equipment in Appendix G)

5.2 Preliminary Data and Samples

For explanatory consistency, the description of the samples are done as with the geological setting, from the north to the south sectors of the North Sea.

5.2.1 Norway

The Norwegian Geotechnical Institute (NGI) provided data of their tested samples where the CO_2 storage site is located. These data came from the Well 31/5-7 situated between the Troll Field and the Brage Field as shown in Figure 5.1 which targets the Johansen and the Cook formations.

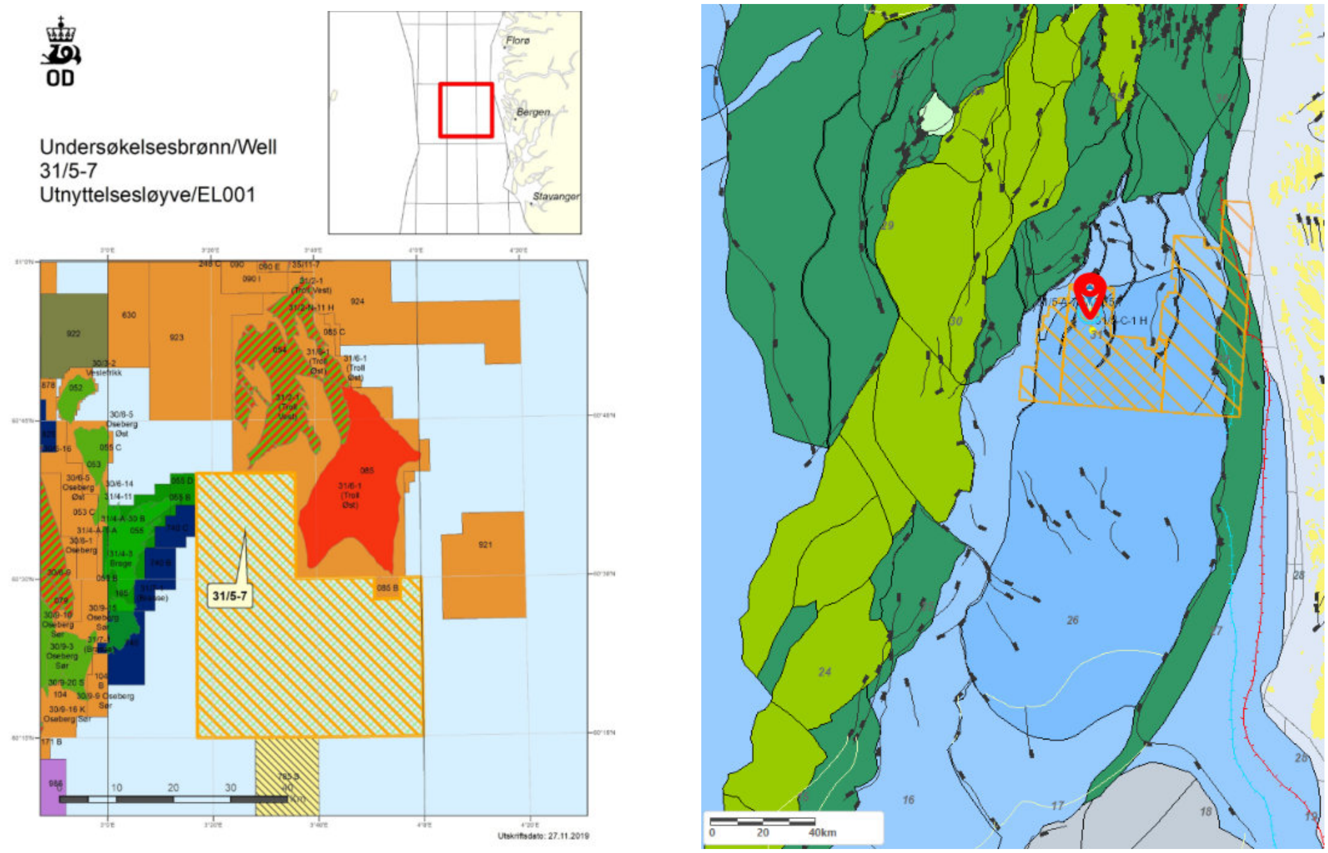

Figure 5.1: Offshore well in the Norwegian sector of the North Sea. Map on the left provided by NGI, map on the right modified from the NPD site.

From this well, three depth intervals were sampled and tested by NGI. The data obtained are provided in Table 5.1. The conducted tests on these samples were Consolidated Isotropic Drained (CID) Triaxial tests with low P_c.

Table 5.1: Information received by NGI about the samples related to the Horda structure. Lithology and depositional environment information obtained from Marjanac et al. (1997) and Sundal et al. (2016).

Sample name	**Well**	**Target Fm**	**Lithology**	**Depositional setting**	**Depth sample [m]**
T2461	31_5-7	Johansen	Fine-grained sandstone	Deltaic sand facies	2761.00-2761.25
T2463	31_5-7	Johansen	Fine-grained sandstone	Deltaic sand facies	2761.00-2761.25
T2464	31_5-7	Johansen	Fine-grained sandstone	Deltaic sand facies	2761.00-2761.25
T2466	31_5-7	Johansen	Fine-grained sandstone	Deltaic sand facies	2725.00-2725.25
T2467	31_5-7	Johansen	Fine-grained sandstone	Deltaic sand facies	2725.00-2725.25
T2469	31_5-7	Johansen	Fine-grained sandstone	Deltaic sand facies	2725.00-2725.25
T2470	31_5-7	Cook	Bioturbated sst. and shales	Tidal and fluvio-estuary	2680.25-2680.50
T2472	31_5-7	Cook	Bioturbated sst. and shales	Tidal and fluvio-estuary	2680.25-2680.50
T2476	31_5-7	Cook	Bioturbated sst. and shales	Tidal and fluvio-estuary	2680.25-2680.50

Table 5.2: Properties of the samples before the test obtained from NGI.

Sample name	Diameter [mm]	Length for test [mm]	Porosity [%]
T2461	24.39	52.21	31.6
T2463	24.43	52.11	31.9
T2464	24.37	52.06	31.7
T2466	24.56	52.27	23.7
T2467	24.52	52.27	24.0
T2469	25.03	52.33	23.8
T2470	24.86	52.42	22.7
T2472	24.94	52.36	23.4
T2476	24.86	52.32	23.7

Figure 5.2 shows samples T2472 and T2463 before testing. These samples look quite similar and homogeneous; however, sample T2472 contains some shale and comes from a bioturbated formation while sample T2463 is a cleaner sandstone. These differences in composition play an important role in their geomechanical behaviour since they can affect the cohesion of the sample and their 'weak' points to hold stress.

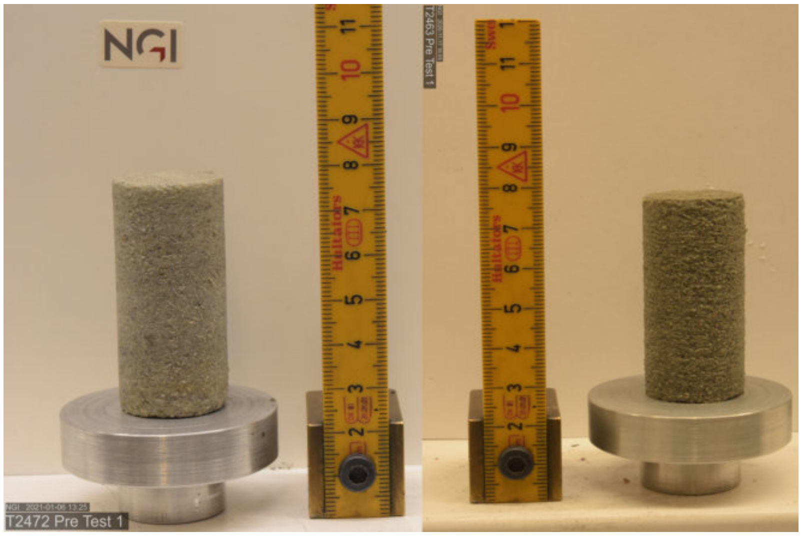

Figure 5.2: Norwegian samples T2472 (left) and T2463 (right).

5.2.2 Denmark

AS with the Norwegian samples, the following table (see Table 5.3) summarizes some of the most important parameters about all of the samples coming from different wells in Denmark prior to the experiments such as their lithology and environment of deposition.

Table 5.3: Information received by Geological Survey of Denmark and Greenland (GEUS) about the samples related to the Lisa structure.

Sample name	Well name	Lithology	Depositional setting	Depth sample [m]
1	Vedsted-1	Fine to medium sandstone	Foreshore	1776.67
2	Vedsted-1	Medium sandstone	Lower shoreface	1777.50
3	Flyvbjerg-1	Fine to medium sandstone	Shoreface	1321.00
4	Flyvbjerg-1	Fine to medium sandstone	Shoreface	1320.60
5	Flyvbjerg-1	Medium sandstone	Shoreface (contain mudlaminae)	1320.50
6	Flyvbjerg-1	Medium to coarse sandstone	Upper shoreface	1316.50
6	Flyvbjerg-1	Medium to coarse sandstone	Upper shoreface	1316.50
7	Gassum-1	Medium sandstone	Upper shoreface	1637.50
8	Gassum-1	Medium to coarse sandstone	Upper shoreface	1634.60
9	Gassum-1	Medium sandstone	Upper shoreface	1633.00
10	Gassum-1	Medium sandstone	Shoreface	1536.20
11	Gassum-1	Medium sandstone	Shoreface	1534.50
12	Stenlille-6	Medium sandstone	Fluvial	1582.70
13	Stenlille-6	Fine sandstone	Fluvial-estuarine	1574.70
109	Thisted-3	Medium sandstone, silty	Estuarine or possible floodplain	1181.32
117	Thisted-3	Fine-medium sandstone	Estuarine	1183.32
133	Thisted-3	Medium sandstone	Estuarine or possible floodplain	1187.58
137	Thisted-3	Mudstone	Estuarine or possible floodplain	1188.32
145	Thisted-3	Fine sandstone	Fluvial	1210.82
201	Thisted-3	Fine sandstone, silty	Estuarine	1227.28
221	Thisted-3	Fine to medium sandstone	Estuarine	1232.28

Table 5.4 shows the parameters of the samples that were tested in the laboratory. Some of the samples received by GEUS were not suitable for testing because of their condition or their dimensions. From sample 109 to 221, the length was too short to do either unconfined or confined compression experiments. Samples 2, 5, and 6 were not well preserved or too fragile to test (very loose grains).

Table 5.4: Parameters of the samples selected for testing.

Sample name	Diameter [mm]	Original length [mm]	Length for test [mm]	Mass [g]	Density [g/cm^3]	Porosity [%]
1	24.70	74.30	50.28	46.38	2.744	29.7
3	24.70	49.60	49.60	46.22	2.848	33.0
4	24.70	43.40	43.40	40.58	2.841	31.4
7	24.70	64.28	50.05	42.43	2.664	33.9
8	24.50	66.00	49.98	41.61	2.703	34.8
9	24.65	75.55	48.60	42.06	2.687	34.4
10	24.75	55.20	49.51	45.83	2.717	29.7
11	24.75	56.10	50.09	45.59	2.739	31.3
12	24.65	68.35	48.99	45.60	2.756	29.5
13	24.75	63.65	49.47	47.43	2.714	26.7

To locate the origin of these samples, Figure 5.3 shows the location of the wells relative to the position of the Lisa structure. By the use of the software Petrel and the information received from GEUS, a correlation was made in which it was possible to see the depth and thickness changes over the distance between the wells (see Figures in Appendix A). Several logging tools were used in order to improve the accuracy of the correlation, i.e. Gamma rays (GR), Density, Neutron Porosity among others. Low GR readings indicates lithologies with low content of radioactive sources (Nazeer et al. (2016)) such as clay minerals. Thus, the lower the GR the cleaner the sandstone is.

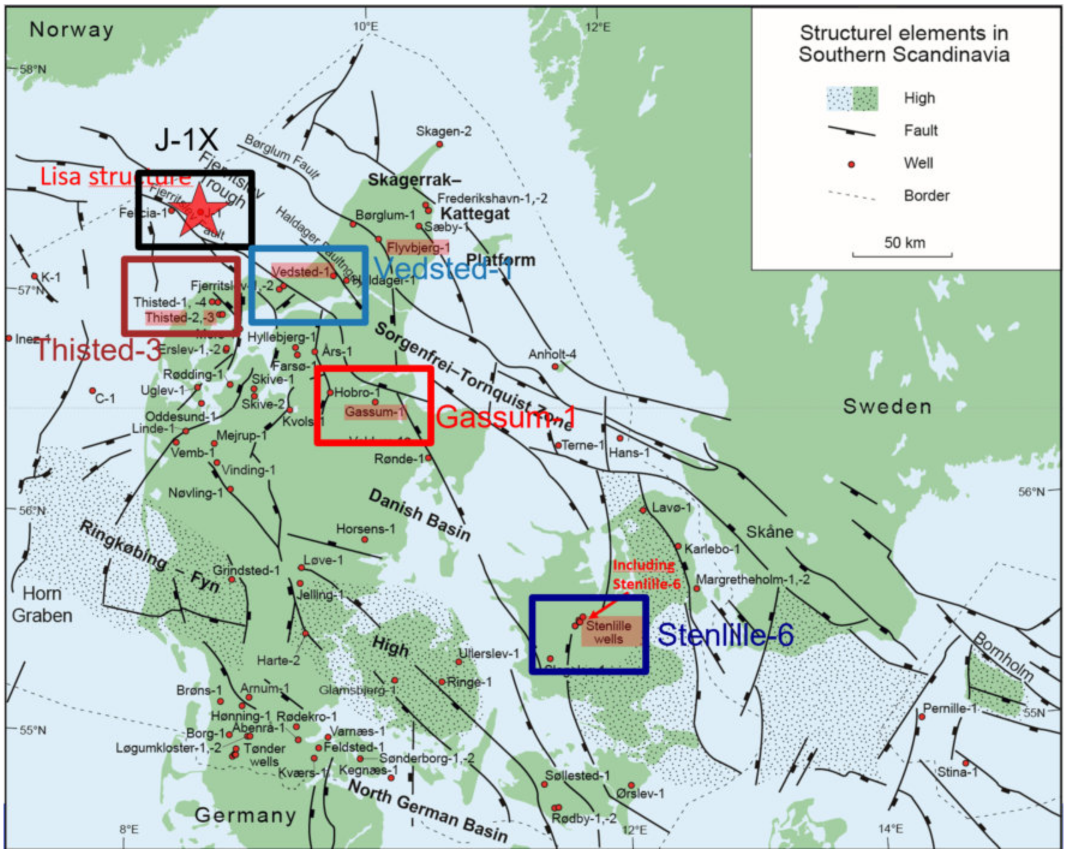

Figure 5.3: Offshore and onshore wells within Denmark where the samples were obtained from, and the location of the Lisa structure (modified from GEUS).

Figure 5.4 shows some of the Danish samples before testing (See Appendix G for more pictures of the rest of the Danish samples). These samples show heterogeneities within their lithology. The features on these samples, such as lamination or content in clay clumps, could affect the way the sample accommodates the compaction and deformation, as mentioned with the Norwegian samples, since the materials differ in composition.

Figure 5.4: Three of the samples received from GEUS: Sample 1 (left), Sample 3 (center) and Sample 13 (right).

5.2.3 Germany

The block of rock received from the quarry in Germany (Konrad Müller GmbH Natursteinwerk) originates from the Red Felser sandstone which is part of the Upper Rotliegend Group. As previously mentioned, this formation is the outcropping analog to the targeted formations in the Netherlands region due to its similar characteristics in age and properties. From the block, several samples were cored and cut to the desired dimensions. Table 5.5 displays the preliminary data from all the samples that were used for testing.

Table 5.5: Information about the samples cored from the blocks coming from Germany.

Sample name	Diameter [mm]	Length for test [mm]	Mass [g]	Density [g/cm^3]	Porosity [%]
PB2	29.63	71.84	106.43	2.663	19.6
PB3	29.68	69.95	103.05	2.664	20.1
PB4	29.55	70.11	102.97	2.655	19.5
PB5	29.65	70.28	104.38	2.663	21.1
PB6	29.68	69.20	102.50	2.653	19.5
PB7	29.68	14.67	21.43	2.641	16.4
PB8	29.60	12.17	17.84	2.703	20.4
PB9	29.68	14.05	20.50	2.642	20.2
PB10	29.68	14.40	20.52	2.624	19.4
PB15	29.75	69.85	103.34	2.629	19.2
PB16	29.75	69.85	103.41	2.629	19.1
PB18	29.78	69.85	103.48	2.637	19.5
PB19	29.78	69.85	103.40	2.626	19.3
PB20	29.76	69.85	103.73	2.633	18.9
PB21	29.75	69.89	103.78	2.628	18.9

Figure 5.5 shows an example of the Red Felser sandstone cored from the received block. The color of these samples indicates their continental origin since these sediments were deposited in fluvial environments and the oxidation of the iron minerals stained the sediments (He et al. 2022).

Figure 5.5: Example of one of the Red Felser samples from the German quarry.

5.2.4 Netherlands

From several onshore wells throughout the Netherlands, acoustic data were gathered and published at the Dutch Oil and Gas portal (Nederlandse Olie- en Gasportaal - NLOG), then reported by TNO (Hunfeld et al. 2021). These data comprise information from several formations including the Upper Rotliegend Group. Figure 5.6 shows the locations of these wells where the majority are gathered in the South West of the Netherlands which also corresponds to the West Netherlands Basin. This basin comprises a high density of oil and gas produced during the 1950s which are now targets for geothermal energy (Willems et al. 2020).

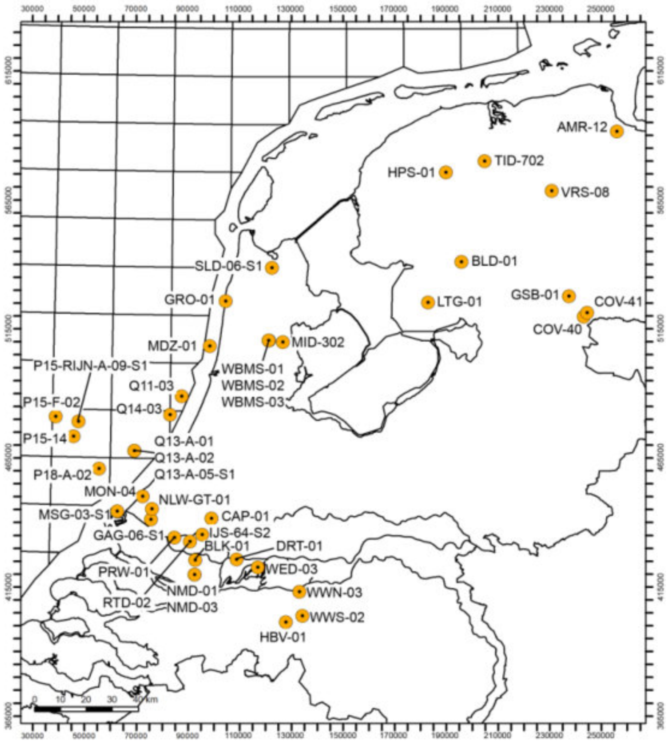

Figure 5.6: Location of wells in the Netherlands from which acoustic data were obtained from the public geomechanical data on nlog.nl.

5.3 Laboratory experiments

Once the samples were prepared, the tests were performed. In this section, the methodology of the different tests carried out with the samples is explained. The explanation of the test setups will be organized by increasing complexity of the test setup.
To analyze the data, several Python scripts were specifically written for this thesis.

5.3.1 Brazilian disc test

The Brazilian disc test (BD) was carried out to study the tensile strength of a rock which is an important factor to determine the Mode I or extensional fractures. However, this strength is an indirect result obtained from this type of test. Figure 5.7 shows the test setup used to carry out the BD test. The sample is compressed in the axial direction without any confinement.

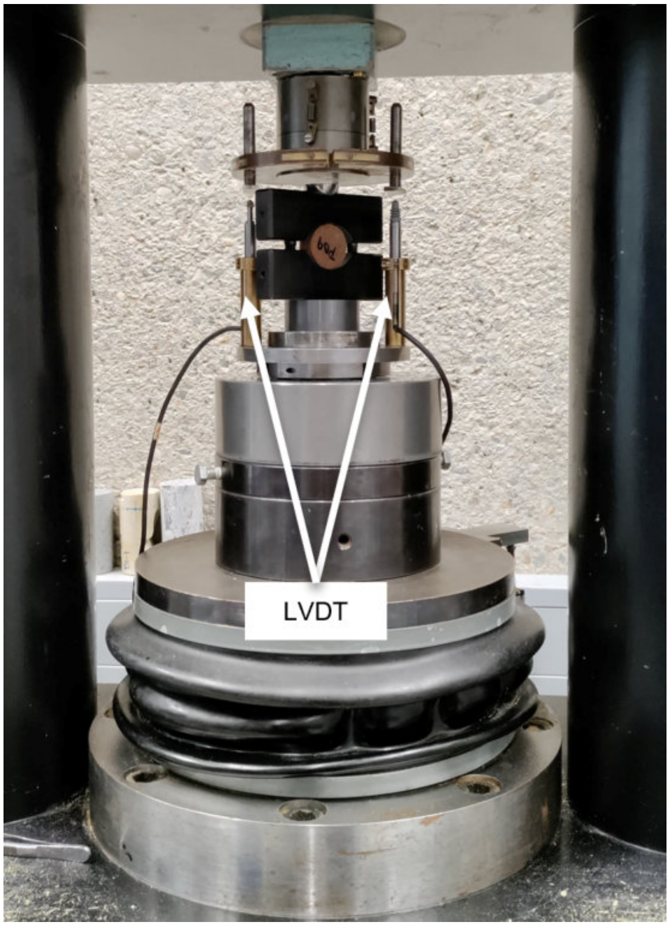

Figure 5.7: Experimental setup to test the tensile strength of a rock sample.

In order to calculate the tensile strength is necessary to have the maximum load, the diameter and the length (Equation 5.1 obtained from Brown (2015)).

$$\sigma_t = \frac{2 \cdot P}{\pi \cdot D \cdot t} = 0.636 \cdot \frac{P}{D \cdot t} \tag{5.1}$$

Where, σ_t is the tensile strength of the sample in MPa, P the recorded load in kN, D, the diameter of the sample and t the width of it in mm.

5.3.2 Unconfined Compressive Strength tests

The Unconfined Compressive Strength (UCS) test allows to measure the strength of the sample and its axial stiffness without a P_c in the horizontal ($\sigma_H = \sigma_h = 0$). The difference between the BD and UCS tests is the type

of fractures developed from the axial compression. For the UCS experiments, the length of the sample and the side from where the sample is compressed creates Mode III or shear fractures in the sample.
Figure 5.8 shows the setup used for this type of test. The sample is fixed on the top and bottom by metal plates which are the source of compression. The chain sensor around the samples measures the radial strain and the Linear Variable Differential Transformer (LVDT) sensors measure the axial strain.

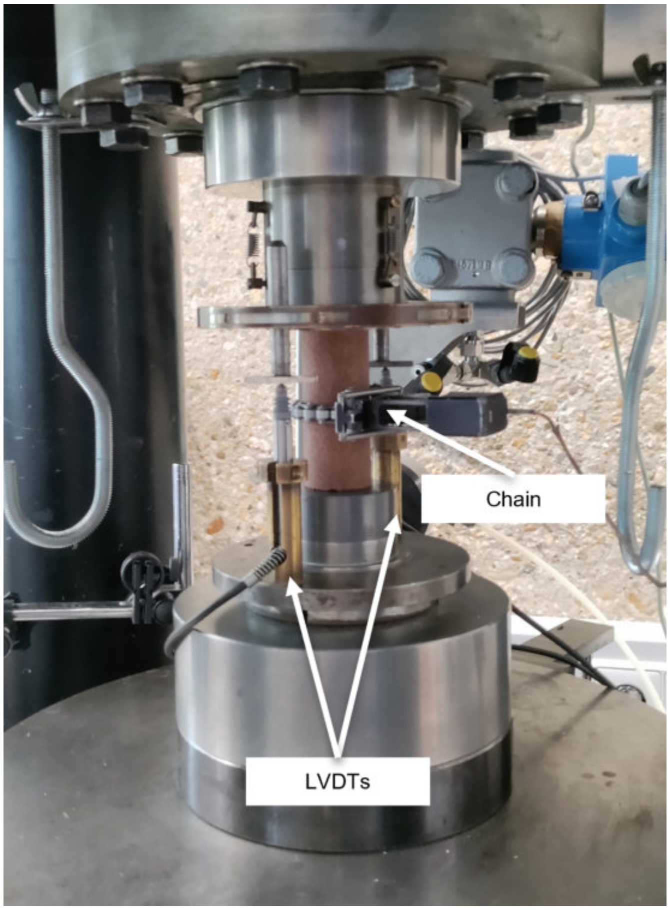

Figure 5.8: Experimental setup to test UCS in rock samples. Indicated are the LVDTs at opposite sides of the sample and the chain wrapped circumferentially around the sample.

From the data collected, a function was fitted via linear regression for each test in order to obtain the elastic modulus (or Young's modulus) which describes the stiffness of the sample. From the collected data, the yield point was also obtained, giving the transition from the elastic to the inelastic region of the stress-strain curve. These parameters will become important factors for predictions about the behavior of the reservoirs formed by these samples in order to avoid risks during injection activities.
In addition, the UCS test allows to measure the Poisson's ratio (PR) of the sample since the chain surrounding it measures the lateral deformation (ϵ_{trans}) and the LVDTs measure the vertical displacement (ϵ_{axial}). Inserting these measurements in Equation 5.2 calculates the static Poisson's ratio. This parameter is unit-less.

$$\nu_s = -\frac{d\varepsilon_{trans}}{d\varepsilon_{axial}} \tag{5.2}$$

5.3.3 Triaxial Compression tests

Triaxial Compression tests give information about the strength of a rock when the horizontal stresses are greater than 0 as well as its stiffness. As with the UCS test, the samples dimensions have a length double that the diameter. In these tests, the axial stress (σ_V) is always greater than the horizontal (radial) stresses (σ_H and σ_h) which in these experiments are equal ($\sigma_V > \sigma_H = \sigma_h$).

In addition to determining the strength and Yield Point, performing this test on a sample also allows to measure the stiffness of the sample through the stress and strain obtained by the force and the LVDTs, respectively. The LVDTs are placed, in this case, on the metallic plate as can be seen in Figure 5.9, contrary to what the UCS setup shows. Moreover, with this triaxial setup, the acoustic data can be measured through the active-source acoustic sensors placed inside the pistons called transducers (red and black squares in the schematic view).

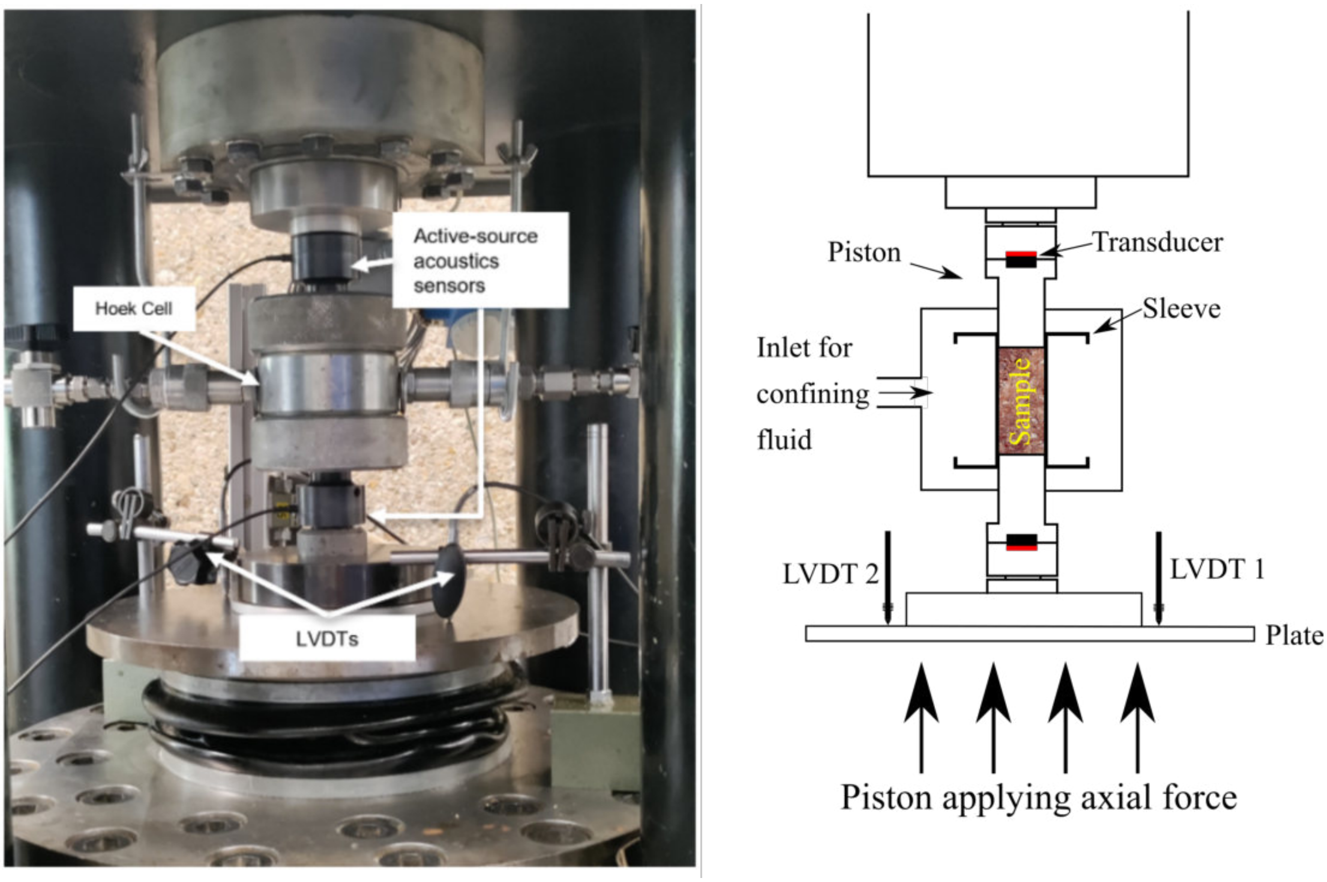

Figure 5.9: Experimental setup to test triaxial compression of rock samples. Indicated are the LVDTs at opposite sides of the plate to measure an averaged axial deformation, the hoek cell inside which the sample is located, and the pistons where the active-source acoustic sensors are located.

The preparation of the Hoek cell depended on the size of the sample at the beginning of the experiment. Some samples were approximately 30 mm in diameter and 70 mm in length while others were 25 mm and 50 mm, respectively. This change in dimensions required a different size of pistons and an extra covering between the oil protective sleeve and the sample to fill the gap. Once the sample was placed on the center of the sleeve, the pistons were inserted and a small amount of oil was pumped with the 'Isco Pomp' to increase the P_c inside ($\approx$0.5 MPa) and hold the pistons in place. Then the cell was positioned in the center of the bottom and top plates (important for equal distribution of the stress to the sample) and locked by applying some force by elevating the bottom plate. The triaxial experiments carried out comprised 5 cycles with a linear stress increase and decrease at the same rate. Each cycle was loaded with a different P_c from 10 to 50 MPa, with an increment of 10 MPa for each cycle. Between cycles, an unloading part was recorded until the axial stress was about 5 MPa higher than the P_c of the next cycle. For all of the samples, the plastic region was reached in every cycle which is an important piece of information because the sample would irreversibly deform during each cycle. In addition, for only the German samples, the last cycle was loaded until the sample reached failure. These tests were specifically performed to obtain the maximum information about the geomechanical behavior of the samples under the different confining pressures. Reaching the plastic deformation region allowed to study a possible real deformation that the rocks suffer during production or injection operations.

Machine strain correction

The strain measured in the triaxial tests is based on the LVDTs positioned on the plate which are also measuring the deformation of the metal parts of the machine that are under stress. Using an aluminium sample for which the elastic properties are known ($E_{al} = 70$ GPa), the same test was performed excluding the plastic zones of each cycle.
From the measured data, the strain of the aluminium was obtained by solving Equation 5.3, where E is the Young's modulus (MPa), σ the axial stress (MPa) and ε the strain. Then, the strain of the machine was calculated assuming Equation 5.4 holds.

$$\varepsilon_{aluminium} = \frac{\sigma}{E_{aluminium}} \tag{5.3}$$

$$\varepsilon_{total} = \varepsilon_{mach} + \varepsilon_{aluminium} \tag{5.4}$$

From this difference in strains, a linear regression was fitted to the strain of the machine for each cycle, yielding the Young's Modulus and applying it to Equation 5.5 to compute for the strain of each sample:

$$\varepsilon_{sample} = \varepsilon_{total} - \frac{\sigma}{E_{mach}} \tag{5.5}$$

It is important to mention that the results shown in Sections 6 and 7 are shown after implementing this correction.

5.3.4 Active-source acoustics

Active-source acoustics measurements refer to the propagation of a wave through a sample. These measurements were done while the triaxial experiment was running. To create this wave, a wave generator and amplifier are necessary to transmit the wave through a transducer (inside the top piston of the triaxial setup). The acoustic signal passes through the top piston, then the sample and through the bottom piston until it arrives to the receiver transducer (inside the bottom piston). The information collected by this sensor is then sent to the oscilloscope to visualize the wave. To this oscilloscope, a computer is connected recording the data. Each wave was sent every 10 seconds through the sample creating Acoustic traces. From Figure 5.9 we know where the transducers are located and Figure 5.10 shows the equipment used for the active acoustic measurements.

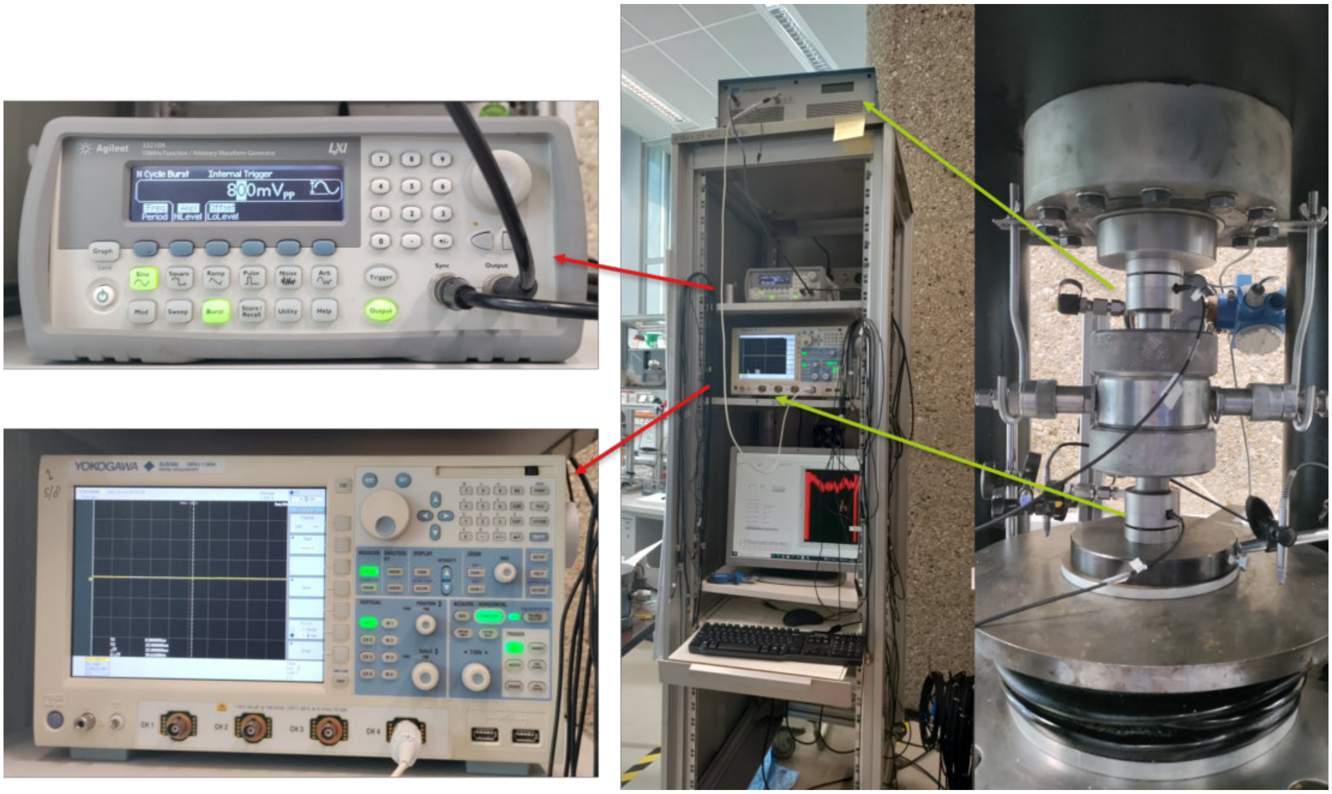

Figure 5.10: Right: the triaxial setup where the transducers are located. The top transducer is connected to the amplifier (top green arrow) which is directly connected to the wave generator (top red arrow), while the bottom transducer (bottom green arrow) is connected to the oscilloscope visualizing the wave (bottom red arrow). Left: the wave generator in the top where the wave parameters are set, and the oscilloscope in the bottom where the wave can be analyzed.

The parameters set for the wave are the same for all experiments (see Table 5.6)

Table 5.6: Parameters of the generated wave.

Wave generator	
Frequency	1 MHz
Amplitude	800 mV
Cycle set	N
Cycle	0
Burst time	5 µs
Oscilloscope	
Sampling	125 kW
ACQ (acquisition)	Average - 256
Time division	100 µs/div
Computer	
Timestep	10

It is important to mention that the transducers send a shear wave (or S wave) through the sample. This is done in order to obtain both P and S waves since there is always a compressive force when sending a wave through the sample. If the P wave transducers were used, only the P wave would be clear but the S wave would be very difficult to distinguish.

The reason to measure these acoustics waves is to improve the understanding of the dynamic behavior while conducting the tests. The grains that compose each sample are different in shape and size and the cement that unifies them fills the spaces in a unique way. These factors impact the transmission of the wave passing through the sample. If the internal structure of the sample is changed when being axially compressed, the wave changes its path and velocity translating into modifications on their dynamic behavior.

The dynamic elastic modulus (E_d) depends on the density of the sample (ρ) in kg/m^3 and the measured velocities (V_p and V_s in m/s) as shown in Equation 5.6 obtained from Mavko et al. (1998).

$$E_d = \frac{\rho V_{\mathrm{S}}^2 \left(3V_{\mathrm{P}}^2 - 4V_{\mathrm{S}}^2\right)}{V_{\mathrm{P}}^2 - V_{\mathrm{S}}^2} \tag{5.6}$$

The density of each sample was assumed constant for the whole experiment.
The P and S velocities were calculated with the use of RadEx Pro software. This software allowed to visualize all of the Acoustic Traces of each loading cycle next to each other as shown in Figure 5.11. This view shows the peaks and troughs of the recorded amplitude which were used to pick the arrival times of both waves. Some of the amplitudes lost resolution when importing the SEG-Y file to the software and the act of selection became complicated as shown in the first traces of the P arrival time.

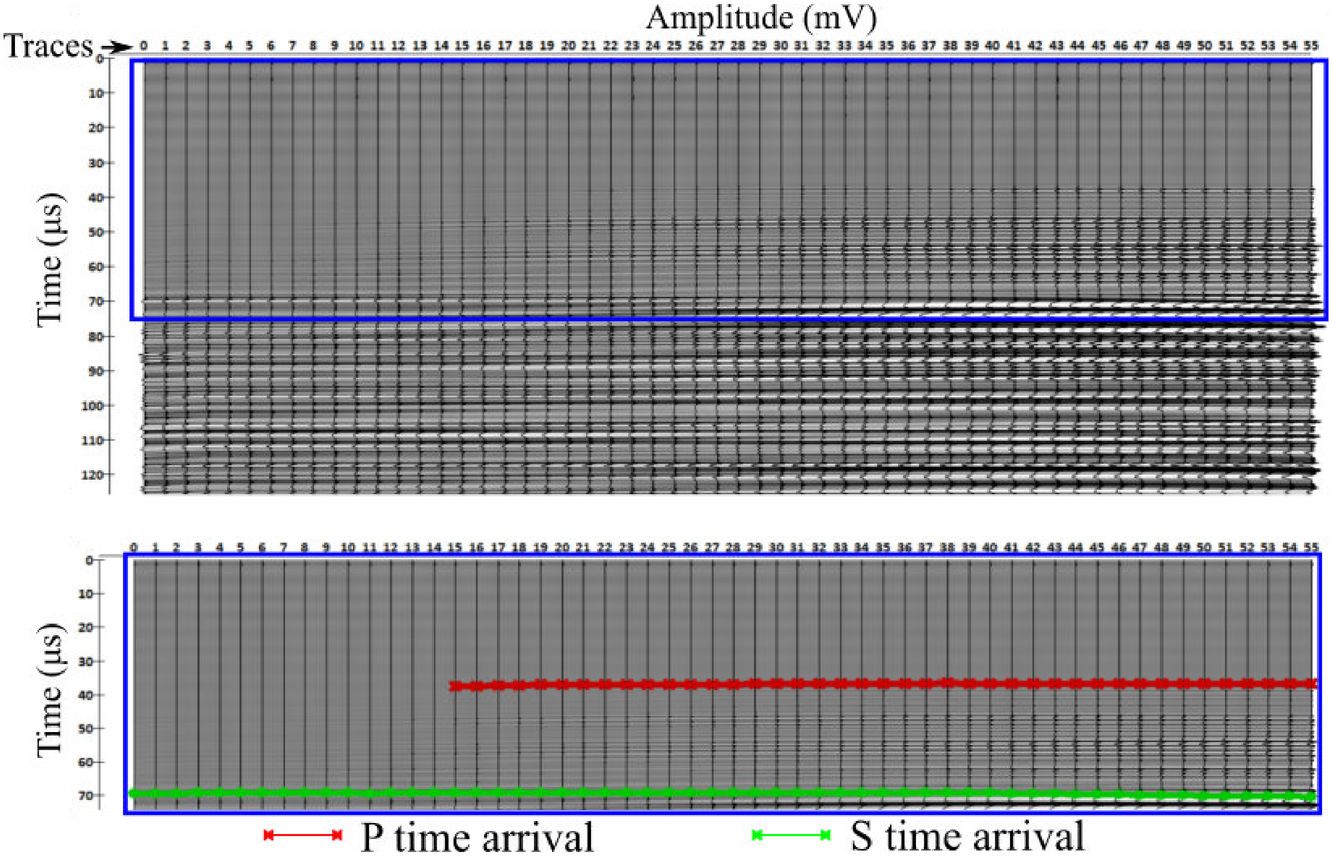

Figure 5.11: Example of a RadEx view of each trace amplitude recorded during a cycle versus time. Each trace is differentiated with an identification number or FFID (numbers in x-axis). This display of traces allows to pick the time arrival of the compressional and shear waves more easily, differentiating the change of amplitudes faster.

Complementing this display is the single trace view of a sample using a Python script (see Figure 5.12). With this display, it was easier to zoom in to the desired section (red rectangle) of the wave and precisely pick the arrival time of both waves, and then extrapolate it to the RadEx view.

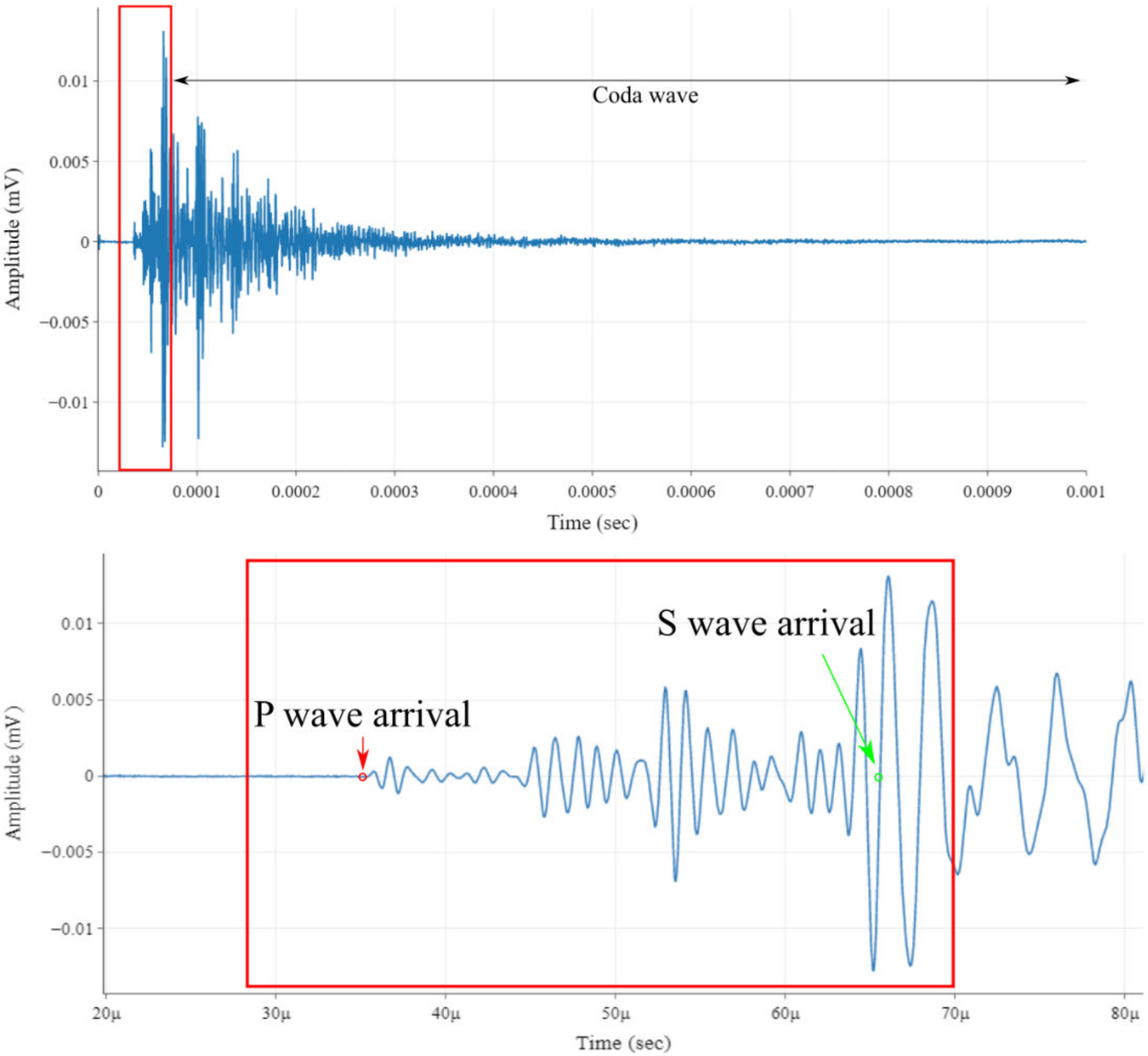

Figure 5.12: Example of a single trace where P and S arrival times are indicated. The S selection corresponds to the start of the largest amplitude since the transducers measure a shear wave.

As for the mechanical data, the acoustic data needs of a correction. As the transducers are inside the pistons and not in direct contact with the sample, the wave first travels from the top transducer through one piston, then the sample, and again through the second piston until it arrives to the bottom transducer. Therefore, the measurement received is not just from the sample and needs to be corrected. To do this, a measurement is taken only with the pistons without a sample in between. Figure 5.13 shows the different arrival times with and without the sample in between the pistons.

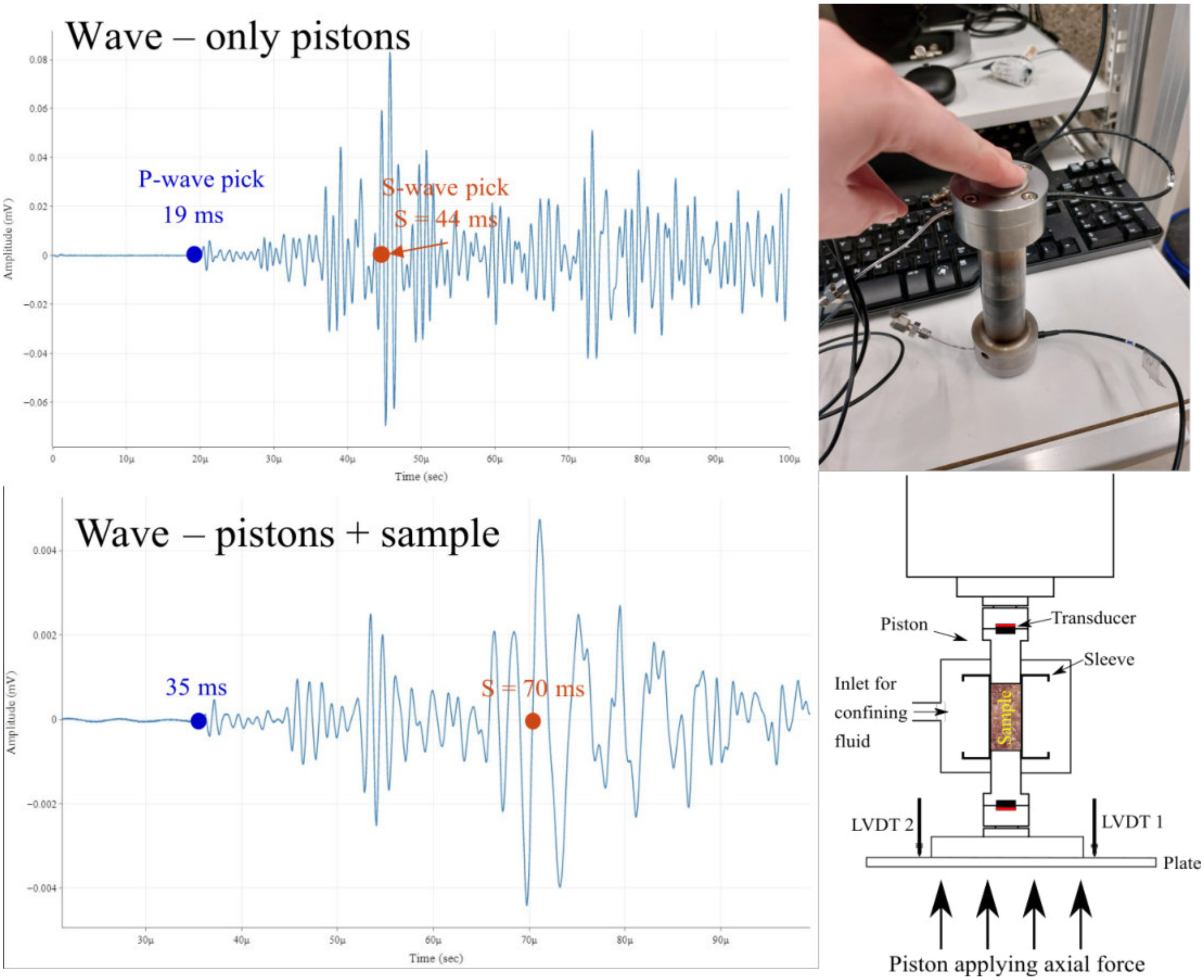

Figure 5.13: Example of an acoustic wave without sample in between the pistons (top image) and an acoustic wave with the sample (bottom image)

For Figure 5.13 different arrival times for the P and S waves are displayed. To correct these arrival times and obtain the corrected acoustic wave of the sample, the subtractions of the P and S waves mus be done.

Once the P and S arrival times were picked, the next step was to calculate the deformation of the sample using the strain measured during the mechanical tests, both the corrected and the total strain.
Through the velocities, it was also possible to calculate the Poisson's ratio (ν) using Equation 5.7 (Mavko et al. (1998)):

$$\nu_d = \frac{V_{\mathrm{P}}^2 - 2V_{\mathrm{S}}^2}{2\left(V_{\mathrm{P}}^2 - V_{\mathrm{S}}^2\right)} \tag{5.7}$$

5.4 Samples information for tests

To summarize, Table 5.7 shows the tests carried out to each sample received from the different countries.

Table 5.7: Test performed per sample. NA = Not Applicable

Sample name	Type of test	Confining Pressure (MPa)	Active-source acoustics measurements?	Micro CT image?
T2461	CID (by NGI)	5-10-15	Yes	No
T2463	CID (by NGI)	5-10-15	Yes	No
T2464	CID (by NGI)	5-10-15	Yes	No
T2466	CID (by NGI)	5-10-15	Yes	No
T2467	CID (by NGI)	5-10-15	Yes	No
T2469	CID (by NGI)	5-10-15	Yes	No
T2470	CID (by NGI)	5-10-15	Yes	No
T2472	CID (by NGI)	5-10-15	Yes	No
T2476	CID (by NGI)	5-10-15	Yes	No
1	Triaxial	10-20-30-40-50	Yes	Yes
2	-	-	-	-
3	-	-	-	Yes
4	-	-	-	-
5	-	-	-	-
6	-	-	-	-
6	-	-	-	-
7	-	-	-	-
8	Triaxial	10-20-30-40-50	Fail	Yes
9	Triaxial	10-20-30-40-50	Fail	No
10	Triaxial	10-20-30-40-50	Yes	No
11	Triaxial	10-20-30-40-50	Yes	No
12	Triaxial	10-20-30-40-50	Fail	Yes
13	Triaxial	10-20-30-40-50	Yes	Yes
109	-	-	-	-
117	-	-	-	Yes
133	-	-	-	-
137	-	-	-	Yes
145	-	-	-	-
201	-	-	-	Yes
221	-	-	-	Yes
PB2	UCS	NA	No	No
PB3	UCS	NA	No	No
PB4	Triaxial	10-20-30-40-50	Fail	No
PB5	Triaxial	10-20-30-40-50	Fail	No
PB6	Triaxial	10-20-30-40-50	Fail	No
PB7	BD	NA	No	No
PB8	BD	NA	No	No
PB9	BD	NA	No	No
PB10	BD	NA	No	No
PB15	UCS	NA	No	No
PB16	UCS	NA	No	No
PB18	UCS	NA	No	No
PB19	Triaxial	10-20-30-40-50	Yes	No
PB20	Triaxial	10-20-30-40-50	Yes	No
PB21	Triaxial	10-20-30-40-50	Yes	No

6 Results

This section displays the results obtained from both mechanical and acoustic data. The mechanical data were obtained from the UCS machines (both 50 kN and 500 kN). These data are considered as the static experimental data. On the other hand, the measured acoustic data were obtained from the previously described active-source acoustic equipment and are considered as the dynamic measurements.
All the results presented in this section include the corrections to the data explained in the methodology section. In addition, as it was observed by the sample pictures in Section 5 and Appendix G, the samples from different countries show many lithological dissimilarities. Some samples have a higher content in clay, the porosity ranges are also different per country, or even color-wise they differ. These heterogeneities make challenging a comparison between the different areas of study. To make this thesis visually easier, several plots are separated by country.

6.1 Mechanical data

6.1.1 Stress-strain cycles

A direct result obtained from the UCS machines are the Stress-Strain plots derived from the force applied to the sample and the LVDTs measuring the displacement of the plate.

While the tests were running, the Stress-Strain plots mainly helped to observe the behavior of the sample and to identify the deformation regimes (elastic or inelastic) of each sample in order to not have undesirable failure. Figure 6.1 shows a variety of plots: A, B, and C correspond to the combination of all of the Triaxial tests carried out on the samples, from which it is possible to observe the variability on the behavior of the samples per country; and D, E, and F show the tests done on one sample from each region to differentiate the cycles.

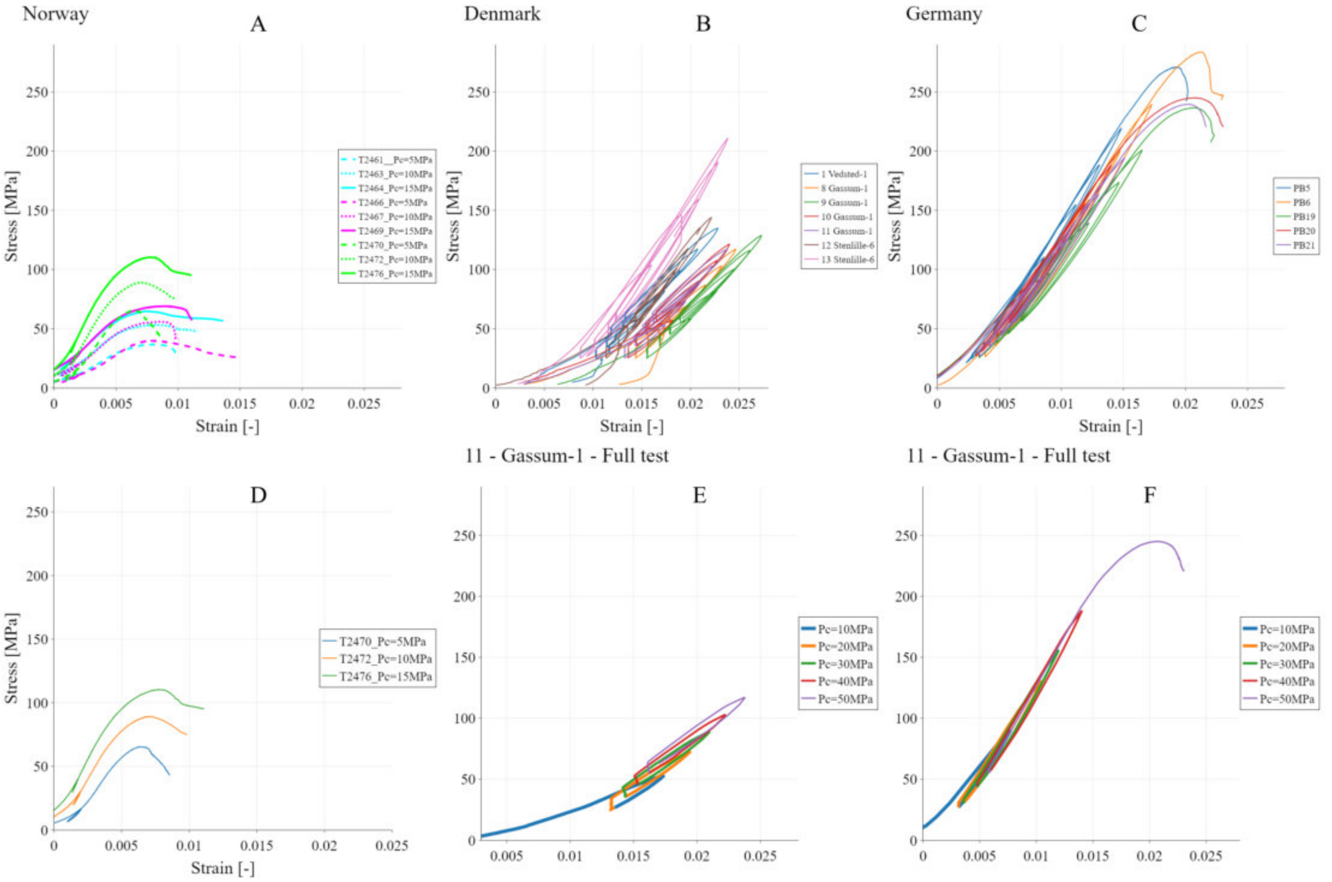

Figure 6.1: Stress-strain plots. A, B, and C plots show the behavioral variability of the samples per region. D, E, and F show an example of one sample in order to differentiate the cycles.

For the Norwegian samples, three different P_c were applied to the samples, from 5 to 15 MPa and reaching failure at each P_c. From plot A, the P_c shows a clear effect in the stress range reached by each sample. T2470, T2472, and T2476 show more stiffness than the rest of the samples (fuchsia and cyan curves). This different behavior can also be related to the provenance of the samples, since T2470, T2472, and T2476 come from the Cook Fm and the rest from the Johansen Fm. Plot D shows three different curves corresponding to three different samples for which the only difference resides in the P_c used in each sample. The blue curve corresponds to $P_c = 5$ MPa and the green curve to $P_c = 15$ MPa.

For the Danish and German samples, five cycles were performed during the triaxial tests (Figures E and F in 6.1). Each cycle corresponds to a different P_c, starting from 10 MPa on the first cycle (blue line) and finishing with a P_c of 50 MPa for the last cycle (purple line). In plots B and C, the behavioral variability of the sandstones can be observed for the Danish and German samples, respectively. In plot B, the Danish samples show a higher variability on their constitutive behavior. This difference of stiffness is strongly correlated to their disparity in depositional environments which played a big role in their porosity, cohesion and lithology (heterogeneities). On the other hand, the variability within the German samples is not very high because all the samples cored from the block are almost identical in their properties.

The six plots display the same ranges in their axes; here it is possible to observe that the deformation and the compression hold by the different samples were very different. The strain that the Danish and German samples reached at the end of the experiments was very similar however the stress reached in comparison indicates that the physical properties of the samples were very different (porosity, cohesion or cementation, homogeneity, or grain size). These properties are characterized by their depositional and burial history.

Finally, since the Norwegian samples were confined with low P_c, the best comparison could be done for the P_c of 10 MPa (orange line in plot D, Figure 6.1). This curve shows less deformation than the Danish sample in the first cycle (blue line in plot E with an strain of 0.017) and similar strain to the first cycle of the German sample (blue line in plot F with an strain of 0.008). The maximum stress reached by the Norwegian sample ($\rho = 80$ MPa) is also higher quantitatively than the Danish one ($\rho = 50$ MPa). This points out again to the differences between the samples from the different regions in terms of porosity and lithology.
In Appendix B, the rest of the stress-strain plots are displayed.

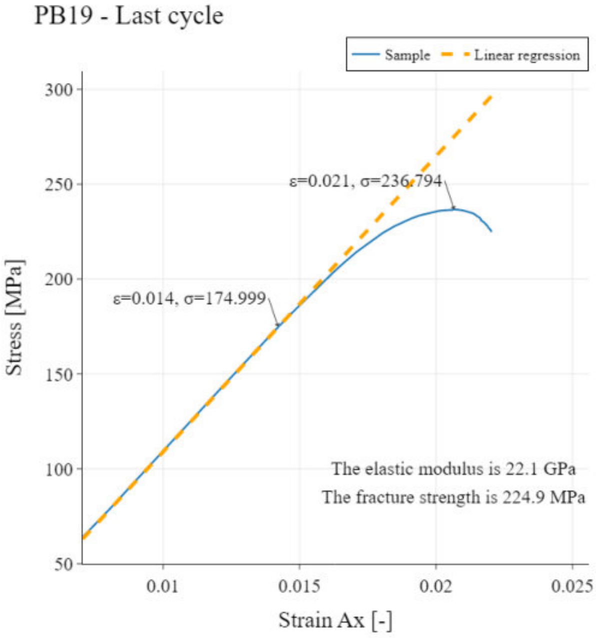

Figure 6.2: Example of the information obtained from a stress-strain plot for the German sample PB19. This is the cycle corresponding to the P_c = 50 MPa where the sample reached failure.

Furthermore, Figure 6.2 shows an example of all the information that can be obtained from a stress cycle. This plot corresponds to the last cycle where failure was reached in sample PB19 ($P_c = 50$ MPa). Since the aim of the thesis was to fully characterize each location based on the available samples, each cycle allowed the extraction of its constitutive behavior, the yield strength, the maximum load and the maximum deformation.
In addition, from each cycle, the slope of the linear region was fitted by a linear regression giving the stiffness of the sample per cycle. Then, based on the inflexion point obtained by looking at the deviation from the linear fit, the Yield Point was also extracted.

6.1.2 Static Young's modulus versus Confining Pressure

Figure 6.3 shows all of the Static Young's modulus (SYM) versus P_c from the samples tested at TU Delft and NGI.

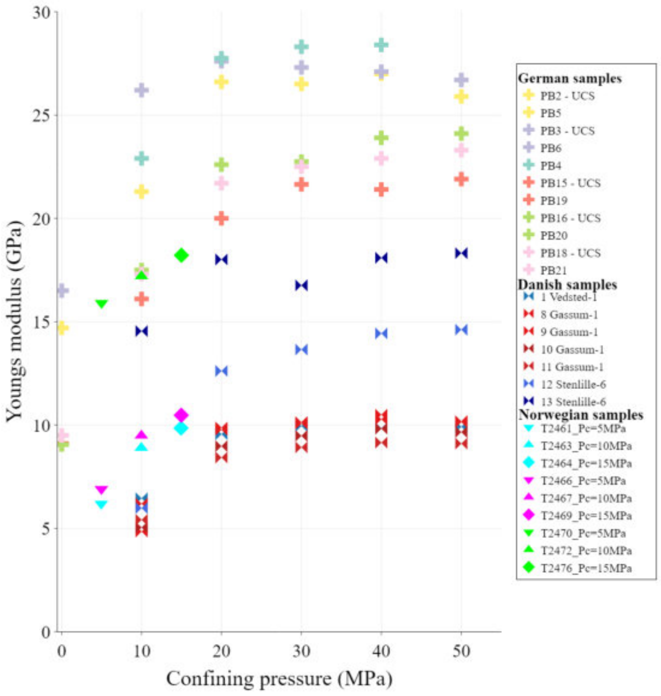

Figure 6.3: Young's modulus versus Confining Pressure for all data received and measured.

In order to have a clearer view of each set of data from the samples, Figure 6.4 shows the Young's modulus versus P_c per country. The ranges of the axes are identical for ease of comparison.

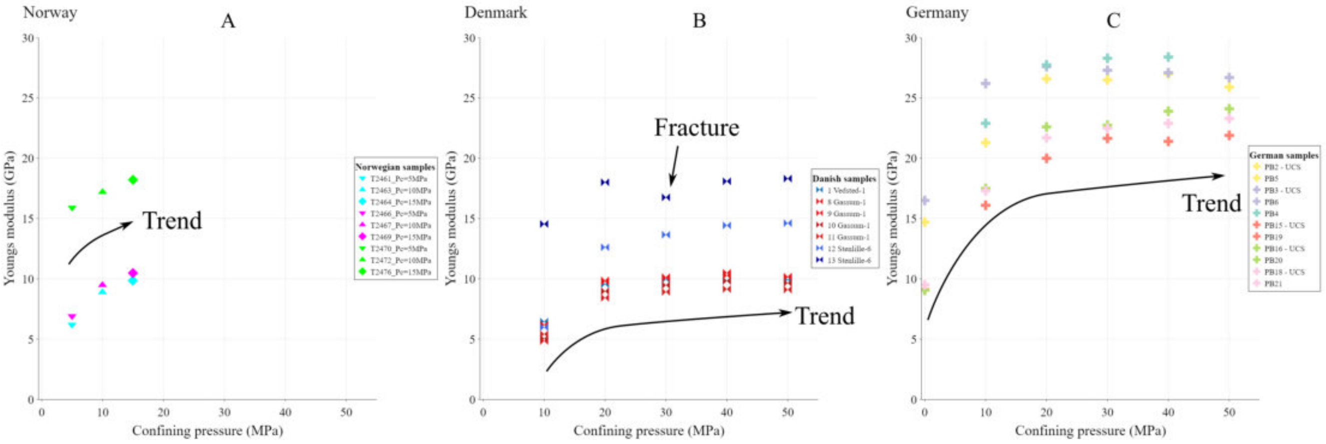

Figure 6.4: Young's modulus versus Confining Pressure, separated by country based on the different properties of the samples.

For all of the tested samples presented in Figure 6.4, the static elastic modulus tends to increase with increasing P_c, which could be explained by the internal rearrangement of the grains via closing voids. This is further addressed in Section 7.

For the Norwegian samples, the laboratory experiments done by NGI used lower but increasing P_c for each sample only reaching up to 15 MPa. However, the changes in the elastic modulus of the sample are clearly dependent on the P_c.

For the Danish and German samples tested at TU Delft, the P_c range reached 50 MPa, giving an understanding of how the samples behave under higher stresses. The Danish samples were only triaxially tested while for the German samples, UCS was also included ($P_c = 0$ MPa in plot C from Figure 6.4). The samples tested for UCS are plotted with the same colors of the triaxially tested samples based on the similarities of their porosity.

The main trend (see Figure 6.4) tends to significally increase for lower P_c, and from the P_c of 30 MPa onwards, it starts to plateau which could indicate that the samples are reaching a stability in their internal structure (SYM is becoming independent of the P_c).

In Plot B (Figure 6.4), the Danish sample 13 from well Stenlille-6 shows a decrease in the SYM at a P_c of 30 MPa. During the second cycle of this test, a small fracture developed compromising the rest of the experiment. Nevertheless, the test was continued to check the behavior of the sample after failure was reached. After failure was reached, the SYM began to increase again without any indication of the fracture propagating in the Stress-Strain curves (see Figure B.3).

6.1.3 Depth versus Static Young's modulus

Figure 6.5 displays the depth from where the samples were obtained versus the computed SYM. In this figure, for the German and Danish samples, the representative result corresponds to a P_c of 10 MPa since the Norwegian samples were tested at low P_c.

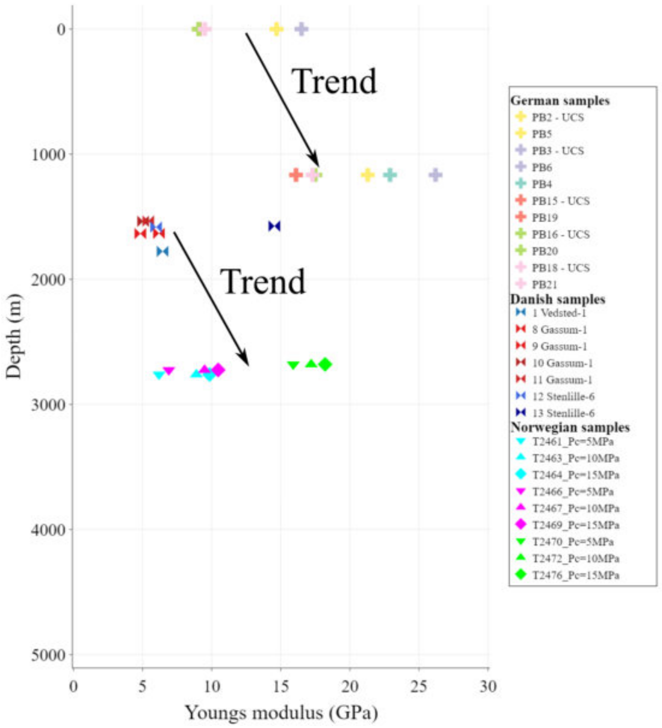

Figure 6.5: Depth versus static Young's modulus. This plot includes the samples tested at TU Delft and NGI.

The German samples were extracted from a quarry, meaning that their depth was 0 m. This depth applies to the samples tested for UCS. However, in Figure 6.5, the samples tested under triaxial confinement show a depth of 1170 m. Using the method of Douma et al. (2019) to predict fractures containment in the subsurface based on outcrops, and assuming that σ_3=1/3σ_v at the moment of failure, the depth can be extrapolated. Comparing this

estimated depth to the measured depth of the Danish samples, and considering the stiffness difference between these samples, the calculated depth for the German samples suits the increasing trend. However, taking into account the heterogeneity of the samples, their different burial history, the test setup differences and the human error partaken on the experiments, this trend could give inaccurate predictions.
Appendix C displays the depth versus Young's modulus plots for the different P_c estimated with the method from Douma et al. (2019) for the German samples.

6.1.4 Yield point versus Confining Pressure

From the Stress-Strain curves, an inflection point called the yield point is determined. The yield point is a material property that refers to the point at which a material starts to deform inelastically under stress (Abdewi 2017). Figure 6.6 shows the change of the yield points of the tested samples with the different P_c.

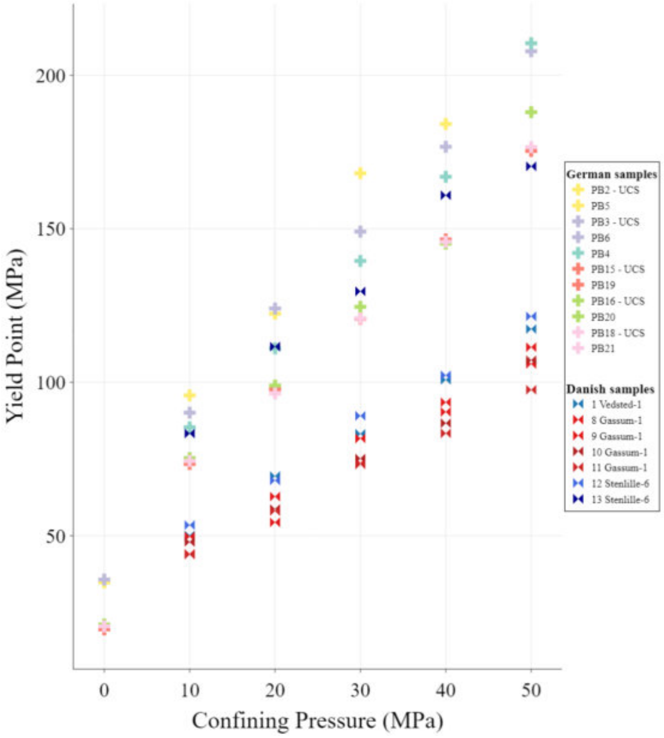

Figure 6.6: Yield point versus Confining Pressure.

The linear trend of the yield point indicates that the internal change of the samples seems to be happening at a later stage in each cycle with increasing P_c since all the deformation occurs in a smaller stress range (Li et al. 2023).
Figure 6.7 shows the Yield Point versus P_c per region, in order to see the effect on porosity, cohesion and lithology characterizing the different samples coming from each formations. These plots show how the trend is consistently linear increasing with the increasing P_c. The slope of the German samples is higher since these samples reached higher stresses during the tests.

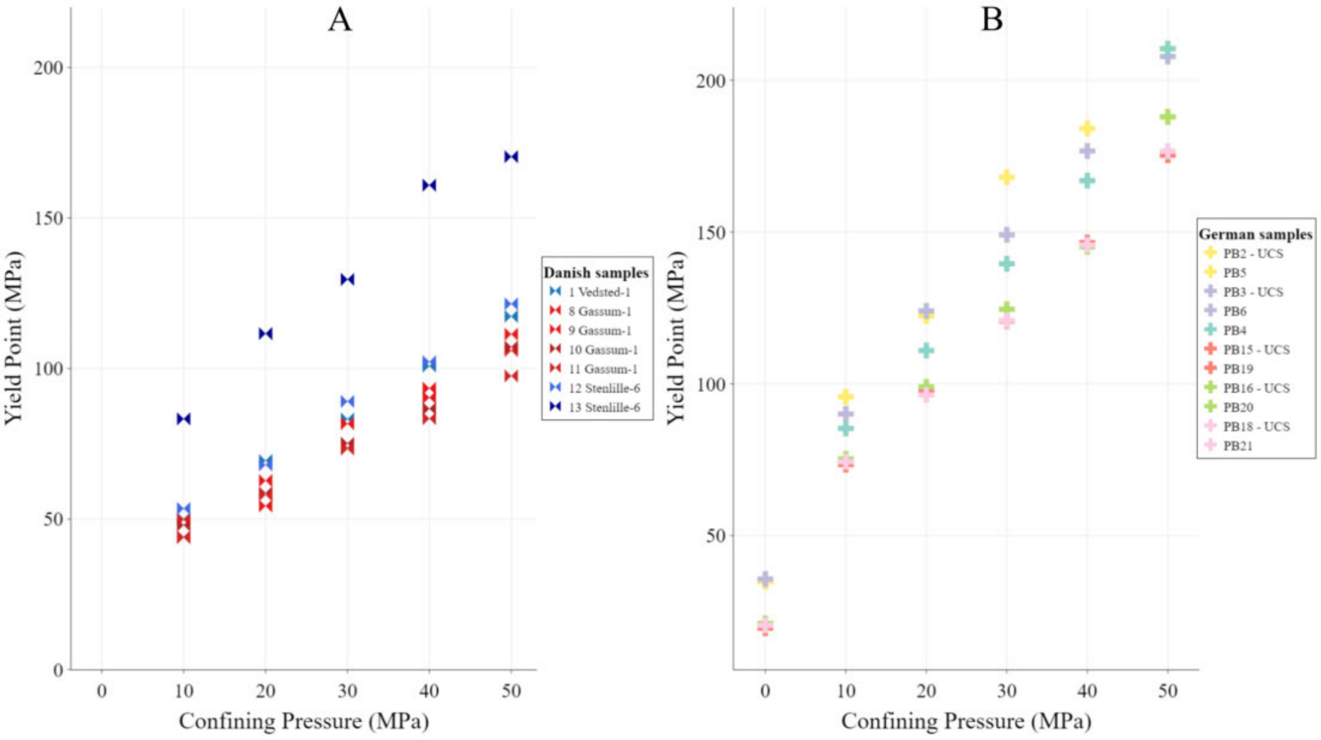

Figure 6.7: Separated Yield Point versus P_c per country.

We can also observed that the slope of the Danish samples 13 doesn't stay linear but it's slope decreases on the last three cycles where P_c was 30, 40 and 50 MPa. This could be a direct effect on the fracture developed on the second cycle of the triaxial test.

6.1.5 Failure & Yield envelopes

From the maximum stresses before failure and the Yield Points obtained through the experiments, the Mohr-Coulomb failure and yield envelopes were computed. The Mohr-Coulomb plot is a linear equation that describes the relationship between the shear strength of a soil or rock and the normal stress acting on it (Labuz et al. 2012). In other words, it defines the maximum shear stress that a soil or rock can withstand before it fails under a given normal stress. The cohesion of these samples was not an input parameter but a byproduct of the correlation made between the different circles.

Figure 6.8 distinguishes both the failure and yield envelopes for the different samples depending on the type of results obtained from the tests.

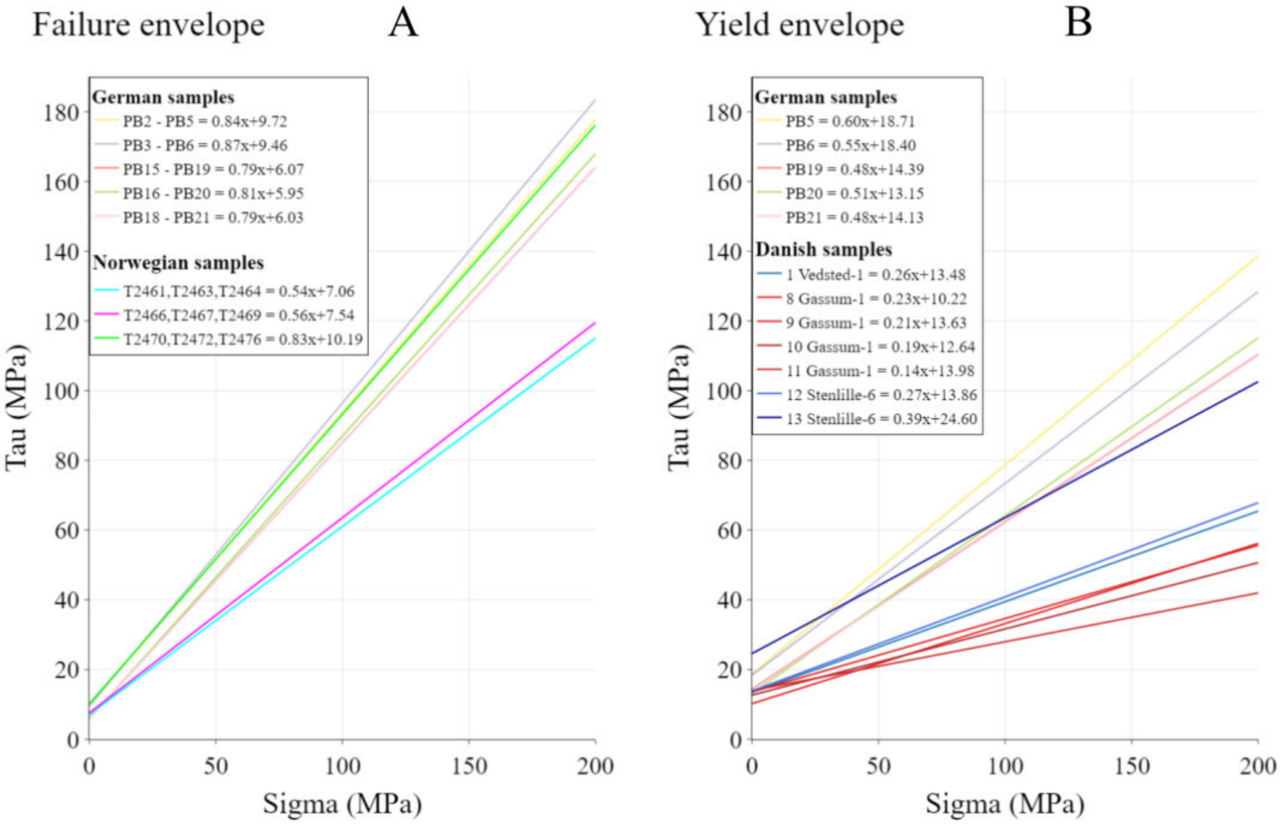

Figure 6.8: Mohr-Coulomb failure envelope (left-hand plot) and yield envelope (right-hand plot).

The axes have the same ranges so the comparison between envelopes is convenient. These envelopes were calculated as the mean of the failure or yield points, and P_c. Figure 6.9 shows an example of the obtained circles and envelope based on the data of the stress-strain plots. For the failure envelope of the German samples, the UCS and the last cycle ($P_c = 50$ MPa) defined the slope.

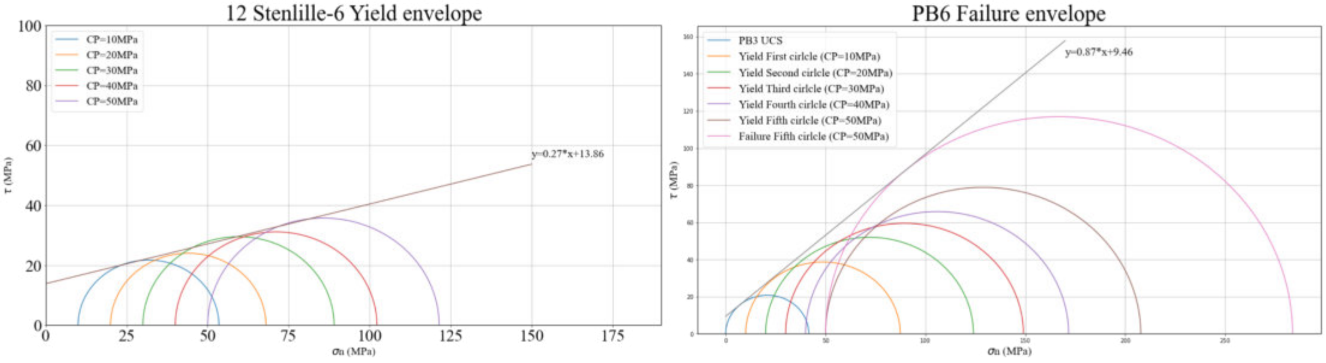

Figure 6.9: Example of Mohr-Coulomb circles for failure and yield envelopes calculated for the Danish sample 12 (left-hand plot) and German sample PB6 (right-hand plot). Note: the range of the y-axis is not the same.

Appendix D displays the rest of the Mohr-Coulomb plots for the German and Danish samples.

6.1.6 Cohesion versus static Young's modulus

From the Mohr-Coulomb circles, the Yield and Failure envelopes were obtained, and from these envelopes the cohesion of the samples can be derived by the intersection of the envelopes with the y-axis. The cohesion is used to measure the shear strength of a rock (Rafiei Renani et al. 2018).

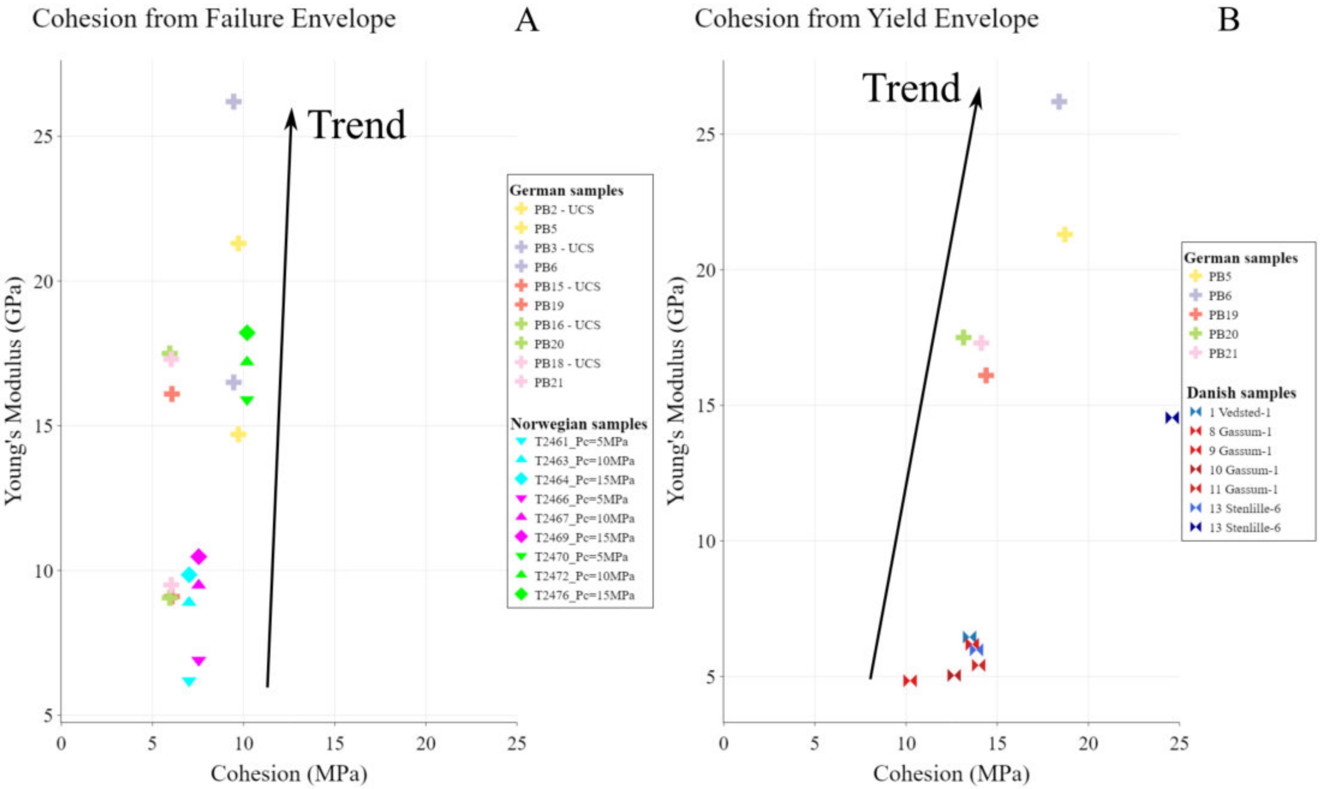

Figure 6.10: Static Young's modulus versus Cohesion. Plot A corresponds to the cohesion derived from the Failure enveloped while plot B correponds to the cohesion derived from the Yield envelope. For the triaxially tested samples, the result shown is for a P_c = 10 MPa.

Figure 6.10 shows the SYM obtained from the stress-strain plots versus the cohesion derived from the Failure (plot A) and Yield (plot B) envelopes. The trend shows an increase of both derived types of cohesion with increasing SYM.

6.1.7 Cohesion versus porosity

The cohesion is also related to the porosity of the samples. The porosity of the samples was measured by the helium pycnometer located at the Rock Mechanics laboratory. Figure 6.11 shows cohesion versus porosity for the cohesion derived from the Failure envelope (plot A) and the Yield envelope (plot B). The trends in this figure show a decrease of cohesion with increasing porosity.

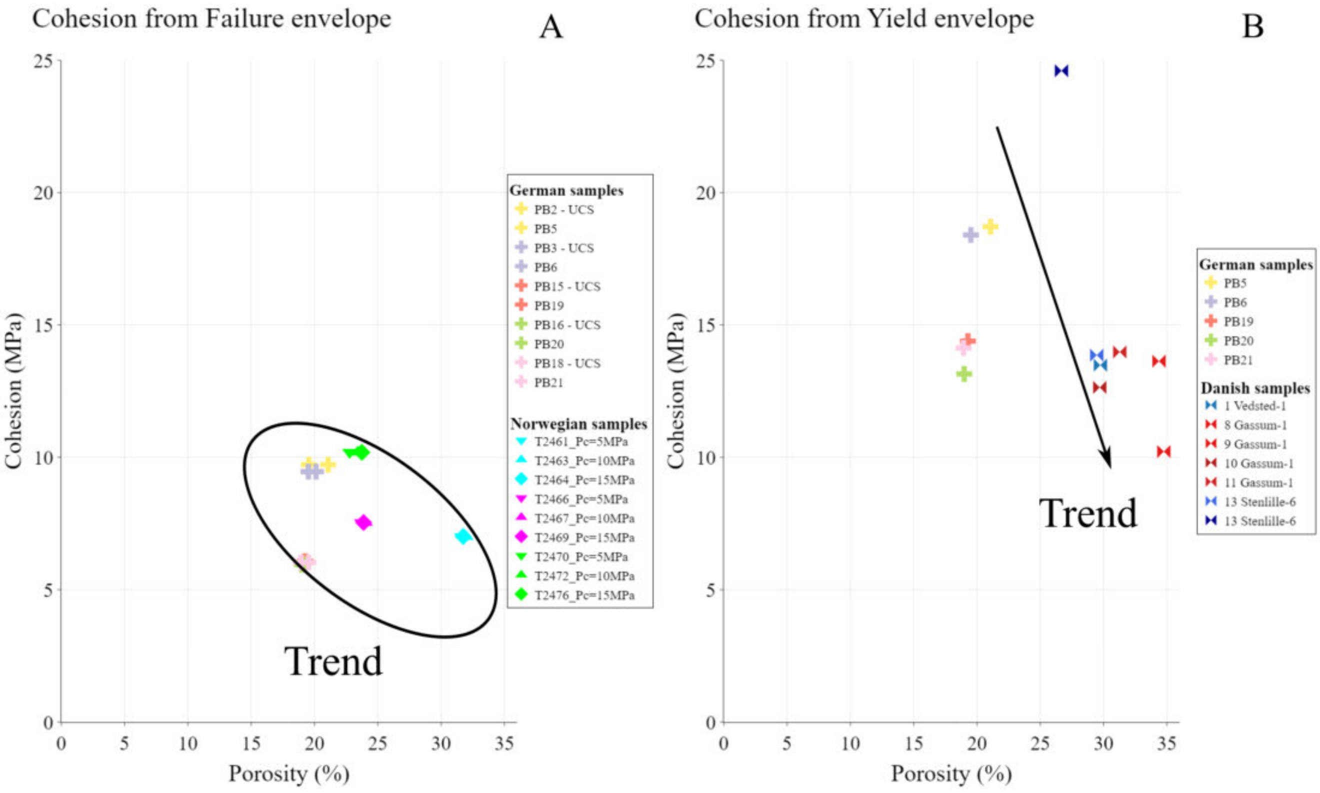

Figure 6.11: Cohesion versus Porosity.Plot A corresponds to the cohesion derived from the Failure enveloped while plot B correponds to the cohesion derived from the Yield envelope. For the triaxially tested samples, the result shown is for a P_c = 10 MPa.

From Figure 6.10, the SYM increases with increasing cohesion, while from Figure 6.11 the trend in decreasing. This gives and insight about an indirect correlation of the effect of the porosity on the SYM; the higher the porosity, the lower the SYM becomes.

6.1.8 Static Young's modulus versus Porosity & Depth versus Porosity

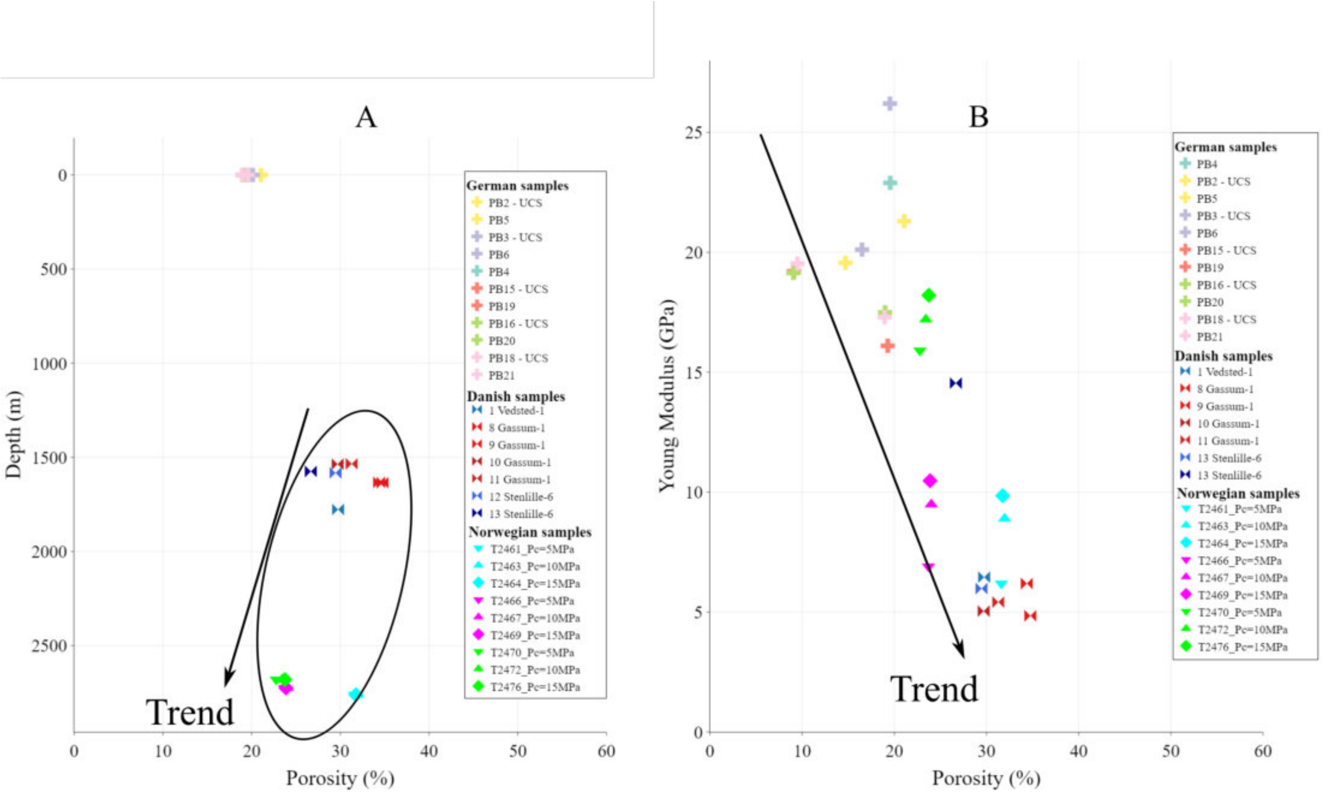

Figure 6.12: Change of porosity with depth (plot A) and with the static elastic modulus (plot B). The trends show a decrease of porosity with depth and with increasing static elastic modulus.

In order to understand the correlation between the porosity and the SYM, Figure 6.12 illustrates the variation of porosity with depth and with the static elastic modulus.

The porosity decreases with increasing depth (plot A) and, as predicted from the cohesion plots (Figure 6.11), the Static Young's modulus increases with decreasing porosity (plot B). As observed in subsection 6.1.2, during the triaxial tests, the SYM increased with higher P_c. This could also be correlated to the increase of the elastic modulus in the subsurface due to an increase in the overburden and P_c. So, the relationship between depth and SYM is positively increasing due to a modification of the internal properties of the sample related to the changes of pressure.

In plot A, the German samples are not following the trend. The properties of this samples based on their geological history, differ significantly from the Danish and Norwegian samples. The German samples show very low porosity and high cohesion even though they are outcropping. Therefore, in Section 7.3 the German samples will be compared to the analog reservoir in the coast of the Netherlands.

6.2 Acoustic measurements

Refer to Table 5.7 , to check the listed samples with active-source acoustic data measured.

The acoustic data measured during the tests were recorded as binary data. In order to use it, a middle step was necessary to convert the data to ASCII or SEG-Y which could be read by the RadEx Pro Software. This step was done through a python script which converted the binary data to SEG-Y to import it directly into RadEx Pro.

As with the mechanical data, the Acoustic measurements are dependent on some parameters of the sample. For the Acoustic data, the porosity and the fluids filling these voids influence greatly the paths of the waves passing through the samples.

6.2.1 P and S waves velocity

From the picked time arrivals in RadEx Pro as shown in Figure 5.11, and the calculated deformation through the triaxial tests based on the strain, the velocities of the P and S waves were obtained.
Figure 6.13 shows an example of the P and S waves velocities versus the Acoustic traces for each cycle of the triaxial test done to the Danish sample 1 (plot A) and German sample PB20 (plot B). As mentioned in Section 5.3.4, these Acoustic traces were recorded every 10 seconds passing through the samples. The mechanical data was then adapted to fit the recorded Acoustic traces.

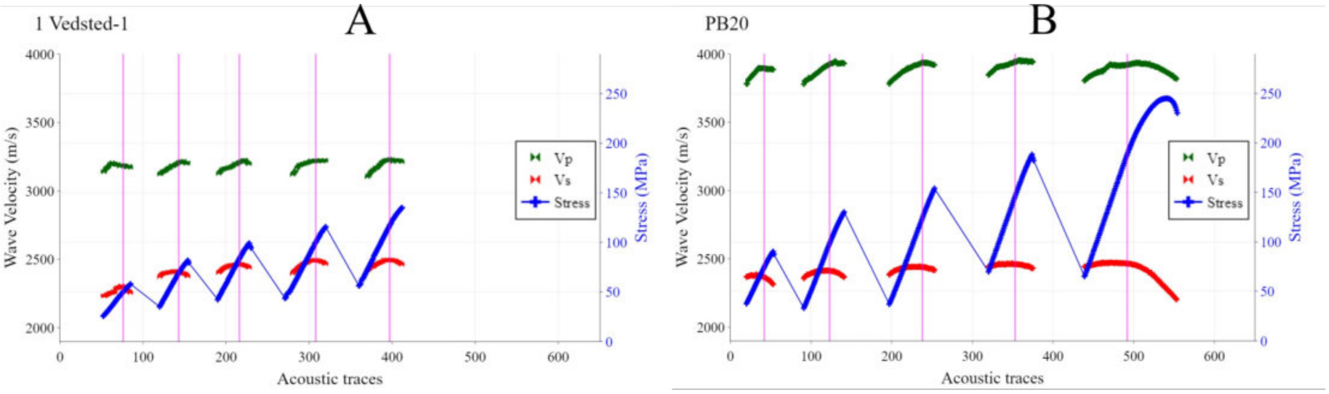

Figure 6.13: Wave velocity and axial stress versus the Acoustic traces measured every 10 seconds during the triaxial experiments. Magenta vertical lines represent the Yield Point of each cycle.

In Figure 6.13, the stress cycles (blue data points) from the triaxial tests show the constitutive behavior of the samples under different P_c versus the Acoustic traces. The magenta vertical lines depict the Yield Point reached in each triaxial cycle. The P and S waves velocities from the recorded traces in each individual cycle correspond to the green and red data points, respectively. Both waves velocities showed a small increase at the beginning of each cycles. After the Yield Point was surpassed, the waves velocities decrease or plateau. For the German sample example, when failure is reached at the end of the last cycle, the velocities decrease significantly.
It is important to consider that the picking times of the P and S waves contain uncertainties related to the low resolution of the image, thus the velocities are not perfectly smooth in their transitions. These errors also affect other results calculated using the velocities such as the Dynamic Young's modulus (DYM) and the Dynamic Poisson's ratio (DPR) (Siggins (1993)).
Appendix E displays all of the plots depicting the Mechanical data and P and S waves velocities versus Acoustic traces.
In order to do a more visual comparison of only the velocities with the presented data, Figure 6.14 shows the change of the P and S waves velocities (V_p and V_s, respectively) against the P_c. The mean of the velocities per cycle was used for these plots in order to have a clear understanding of their change with varying P_c.

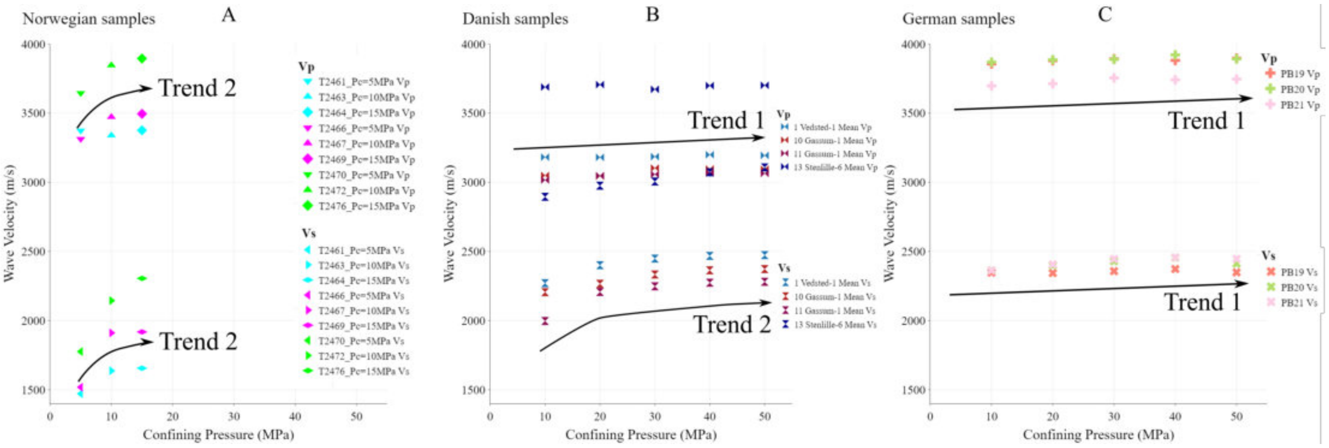

Figure 6.14: Mean wave velocities versus Confining Pressure.

For Plot C, depicting the German samples, the general trend (Trend 1) for P and S waves is linear and independent of P_c on all the samples, with the V_p ranging between 3500 and 4000 m/s and the V_s from 2200 to 2500 m/s for all P_c. Assuming the porosity in the German samples is not varying significantly with P_c, the paths taken by the compressional and shear waves are relatively constant.

For the Norwegian samples in plot A, the V_p ranges between 3300 and 4000 m/s (similar to the German samples) and the V_s between 1500 and 2500 m/s. The trend shows a positive dependency of the P_c which allows us to assume that the porosity of the sample is being affected by the mechanical compression and therefore the waves pats are also being modified which directly changes their velocities.

In plot B, the majority of Danish samples show a V_p of 3000 to 3500 m/s and a V_s of 2200 to 2500 m/s (similar to the German samples). These samples show a general trend (Trend 2) where the V_s is dependent of P_c when it's lower than 30 MPa. As with the Norwegian samples, this could be an indication of their lower cohesion and the restructuring of the grains with compression. Moreover, with higher P_c, this internal changes are less significant and therefore the velocities become independent of the compression. In addition, Danish sample 13 shows higher V_p (about 3700 m/s) and V_s (2900 to 3100 m/s) than the rest of the Danish samples.

Asef et al. (2013) obtained similar trends of wave velocity versus confining pressure through laboratory experiments carried out in limestones. An initial exponential increase of the velocity at lower P_c than 15 MPa and a following linear trend.

6.2.2 Wave velocity versus Porosity

As mention for Figure 6.14 the assumption about the effect of the porosity on the velocity of the acoustic waves was made (Sayers et al. 2002). Figure 6.15 shows two trending circles made around the V_p and V_s data clouds depicting a decreasing trend on the velocities as the porosity of the samples increases.

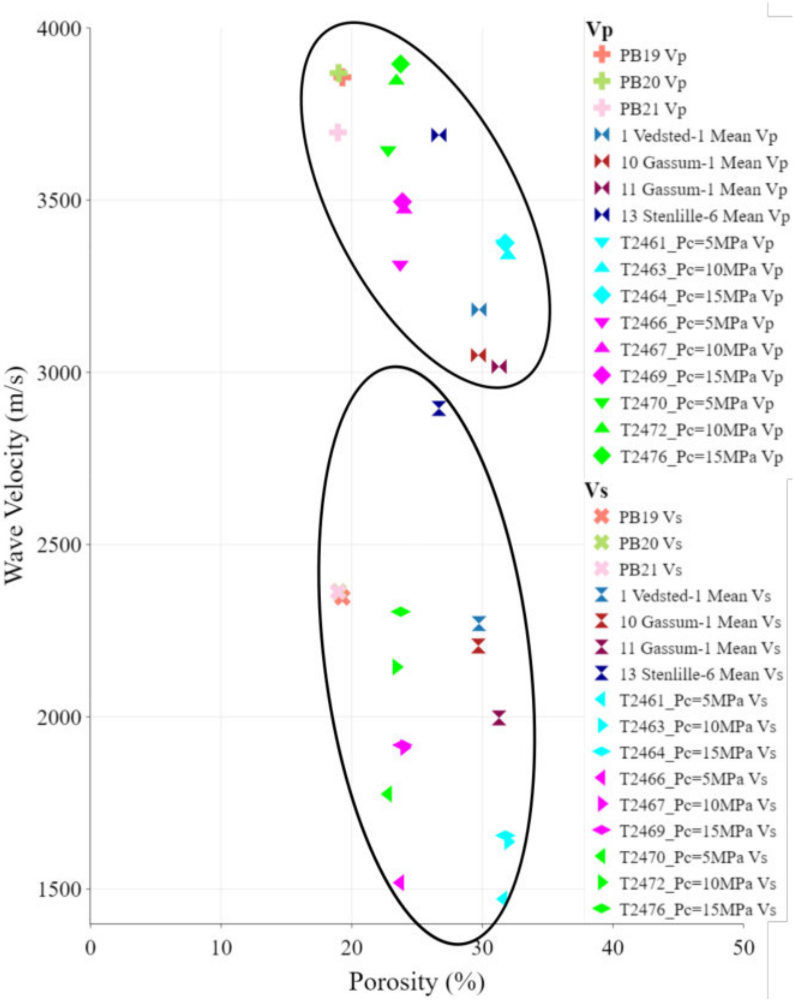

Figure 6.15: V_p and V_s versus Porosity. The range on the x-axis was increased to display a more clear trend of the data.

The stress and geological history of these samples are very different and significant for the results on the V_p and V_s. Based on this fact, the trends were not directly visible and therefore an ellipse shape was chosen to show a trend instead of an arrow.

6.3 Dynamic versus Static Young's modulus

Based on the wave velocities, the DYM was obtained by applying Equation 5.6 in Section 7.3. Figure 6.16 shows the SYM and DYM obtained from the mechanical tests and acoustic measurements for the Danish samples (plot A) and the German samples (plot B). These comparisons allow to understand the behavior of the samples as a function of P_c using two different techniques to collect data.
For the Norwegian samples, their density was not provided which didn't allow the calculation of the DYM.

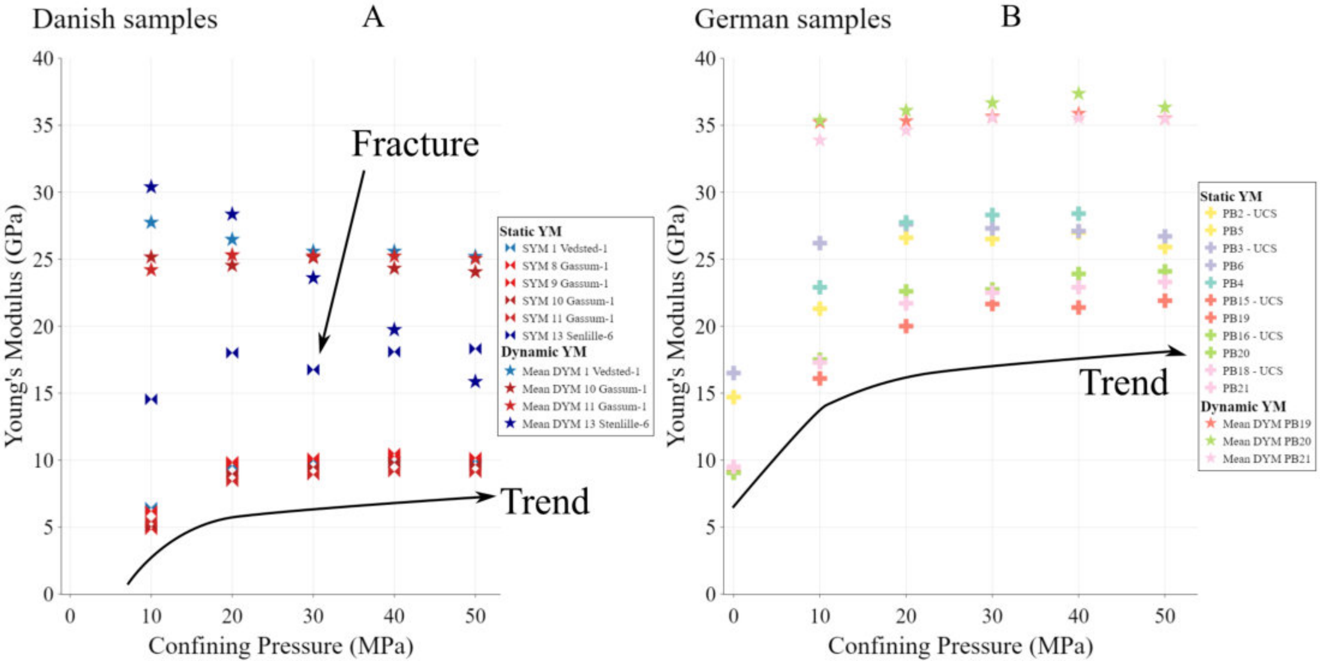

Figure 6.16: Comparison between Static and Dynamic Young's modulus for the Danish (Plot A) and German (Plot B). DYM = Dynamic Young's modulus and SYM = Static Young's modulus.

In plot A, the Danish samples showed a positive dependency of the P_c when lower than 30 MPa for the SYM. This trend is also followed by the DYM for samples 10 and 11 from the Gassum-1 well. However, sample 1 from the Vedsted-1 well and 13 from the Stenlille-6 well, show a decreasing trend of DYM with P_c. For sample 1, this decrease is more pronounced at P_c lower than 30 MPa, and for higher P_c the DYM becomes independent of P_c. On the other hand, for sample 13, the negative trend is constant which indicates a change on the internal structures of the samples. Since sample 13 developed a fracture during the second cycle of the test, this decreasing trend is very possibly related to the micro propagation of this fracture and the movement of the water filling the pores through it.
AS for the German samples (plot B), the trend showed a positive dependency of the DYM with P_c until a P_c of 30 MPa. At higher P_c, the slope of this trend decreases which indicates that the dependency of the DYM on the P_c is also decreasing.
The difference in the magnitude between the static and the dynamic results are expected since the data was obtained with different methods. In addition, this can also be related to the uncertainties gathered through the experiments and the heterogeneity on each of the samples.

6.4 Dynamic and Static Poisson's ratio

Figure 6.17 shows the Static and Dynamic Poisson's ratio based on the UCS data and active-source acoustics measurements recorded at TU Delft and the data collected by NGI. The Dynamic Poisson's ratio (DPR) was obtained through Equation 5.7 as described in Section 5.3.4 while the Static Poisson's Ratio (SPR) was calculated through Equation 5.2 (refer to Section 5.3.2).

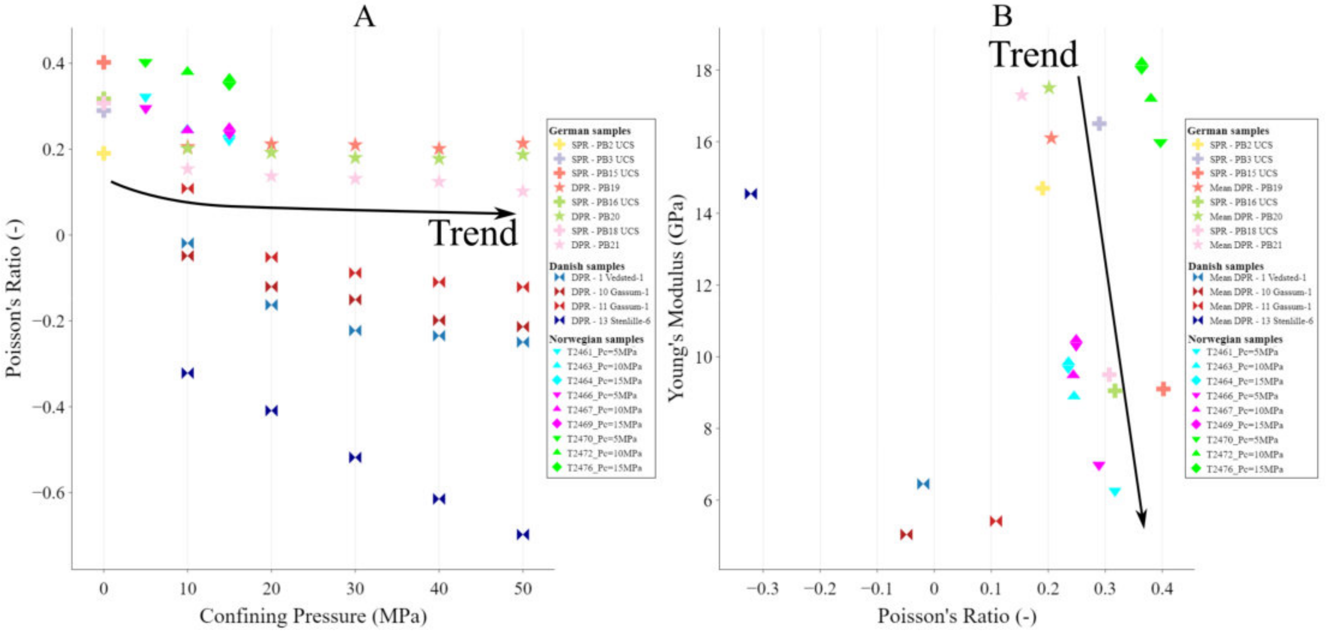

Figure 6.17: Poisson's ratio versus P_c (Plot A) and Young's modulus versus Poisson's ratio (PlotB). Young's modulus of triaxial tests depicted for P_c = 10 MPa. Trends indicate a decrease of Poisson's ratio with increasing P_c and increasing Young's modulus.

As shown in Figure 6.17, using the same equation for all the acoustic data to calculate the DPR, the obtained results gave some quite contrasting results. The SPR and DPR of the data obtained from the UCS tests, acoustic measurements and the data from NGI falls within a similar range of 0.2 to 0.4. In addition, in plot A, the trend follows a significant negative dependency with P_c lower than 20 MPa, while at higher P_c the trend is independent of it.

On the other hand, the results of the Danish samples acquired by the same method give negative values. Especially, Sample 13 shows a big range of PR and a steeper decreasing slope than the rest of the Danish samples.

The Young's modulus versus Poisson's ratio (plot B) also shows a wide variety of results from which, at first, it is difficult to discern a trend. However, if the focus is only on the German and Norwegian samples, it is possible to extract a decreasing trend of the Young's modulus with increasing Poisson's ratio. This trend is also studied by Zhang et al. 2005 in which the decreasing stiffness is related to the content of water saturating the sample which increases the Poisson's ratio.

6.5 Micro CT imaging

During this thesis, nine samples from the Danish sector were scanned in the Micro CT scanner at TU Delft (refer to table 5.7). The resolution obtained from this imaging reached the 0.032 mm per voxel, being able to process the porosity of the samples. The results of this imaging can be observed in Figures 6.18, 6.19 and 6.20 by using the VGStudio MAX software. This software allowed to change the appearance of the volume displayed to be able to observe the internal structure of the sample and its heterogeneities.

The first top images of these three figures show a picture of the sample (under the name of the sample) and a preview of how the sample looks from the Micro CT scan. This image on the right also shows the target area of interest (light blue line) on the displayed samples. Based on the dimensions of the samples, this region of interest covered more or less volume. For instance, samples with smaller lengths like Samples 201 and 221, have the majority of their volume covered by this area, while longer samples (i.e., Sample 3) have an area of interest covering the places with higher heterogeneities.

From the second bottom images, the connected empty spaces (effective porosity) is displayed under different tolerances set on the software. The tolerance number does not give a lot of information by its own if it is not compared with higher or lower values of tolerance, thus, two different values are given to see the effect. The tolerance range was assumed to be affected by the properties of the sample. More cohesive samples to the touch needed higher values of tolerance in comparison to less cohesive samples. This can also be related to the porosity since it has an negative dependency effect on the cohesion.

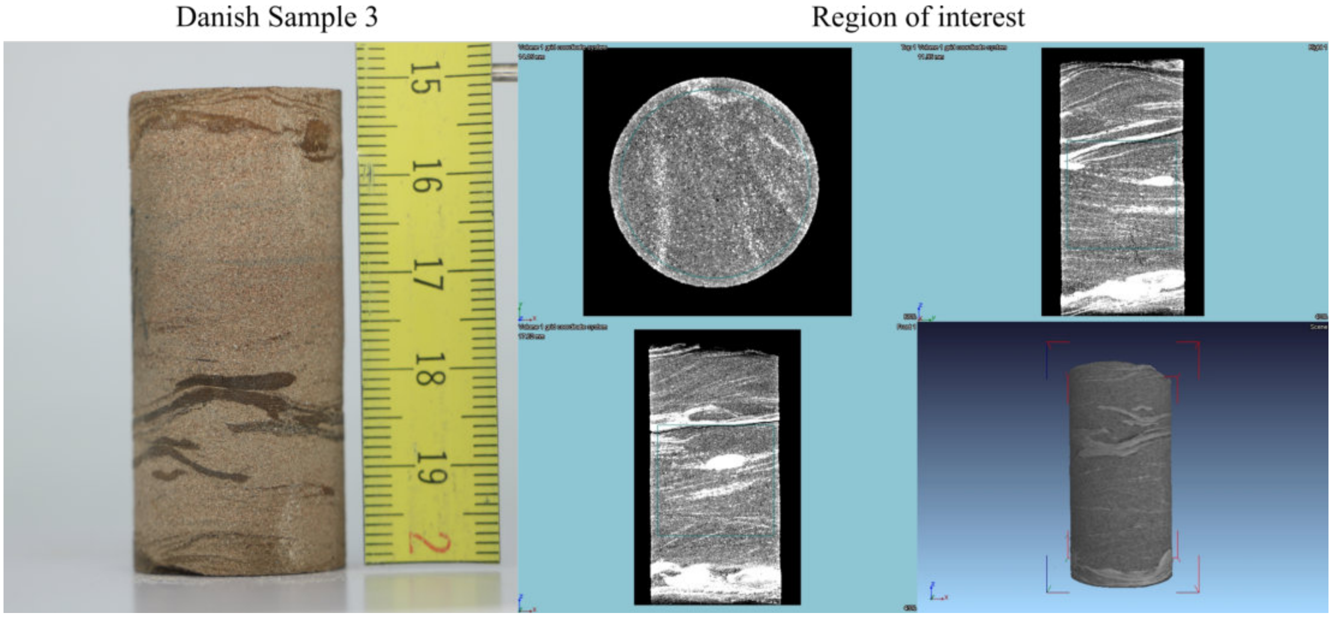
Danish Sample 3

Region of interest

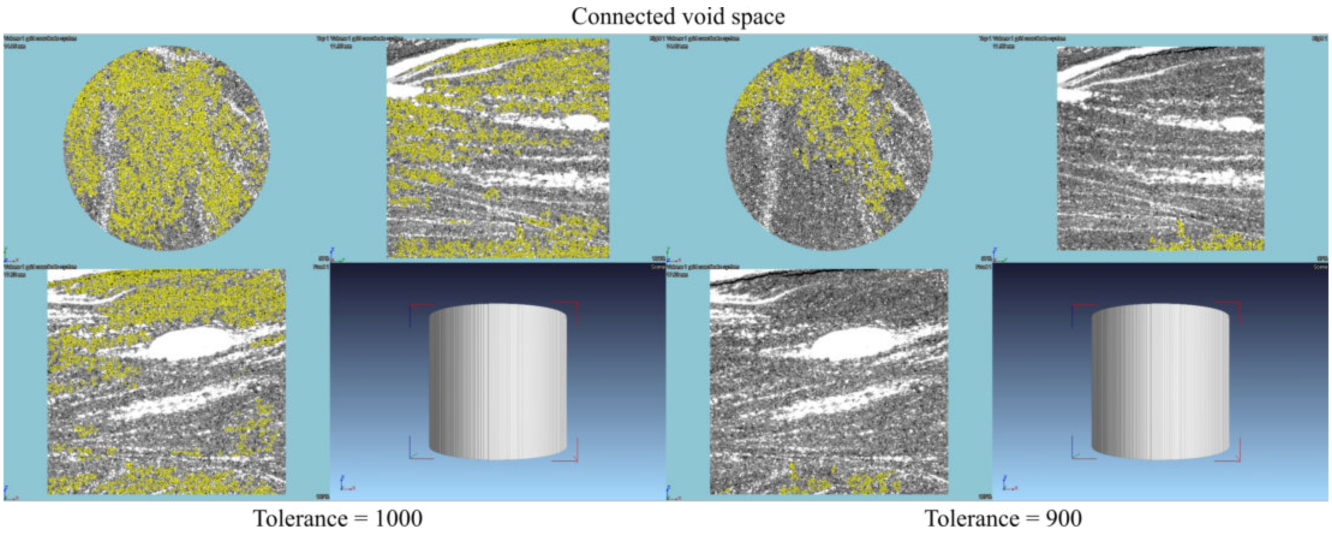
Connected void space

Tolerance = 1000

Tolerance = 900

Figure 6.18: Micro CT imaging of Sample 3. The top image shows the picture of the sample together with a preview of the image. The bottom picture shows the connectivity of the pores when the tolerance set on the software of is 1000 and 900.

From Figure 6.18 the lithological heterogeneity of Sample 3 is very clear where the claystone (dark brown) is being surrounded by fine sandstone (light reddish-brown). From the Micro CT scan, this heterogeneity is also visible in the internal part of the samples. The structures within the sample form some short of cross bedding where the clay (white) doesn't have a specific thickness throughout the sample. This sample has a calculated porosity of 33% (from Helium Pycnometer measurements) and with a tolerance of 1000, it is visible that the connected porosity (yellow color) follows the sandstone beds vertically and horizontally. When this tolerance is lowered to 900, the connectivity decreases significantly, which could be an indication of clay distribution within the voids.

Danish Sample 201

Region of interest

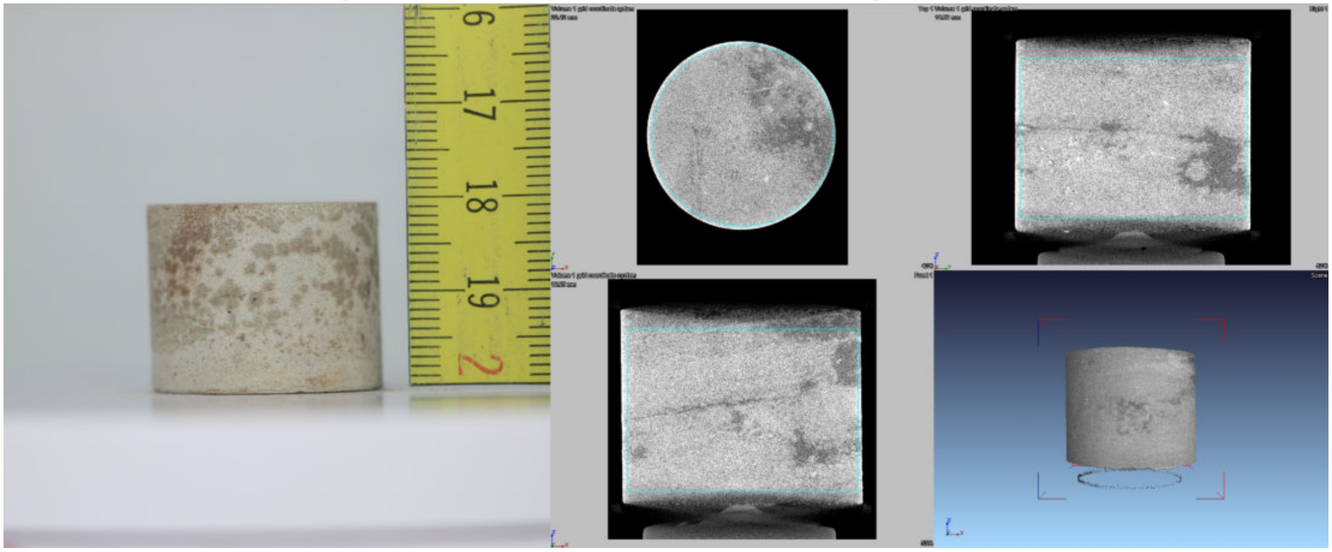

Connected void space

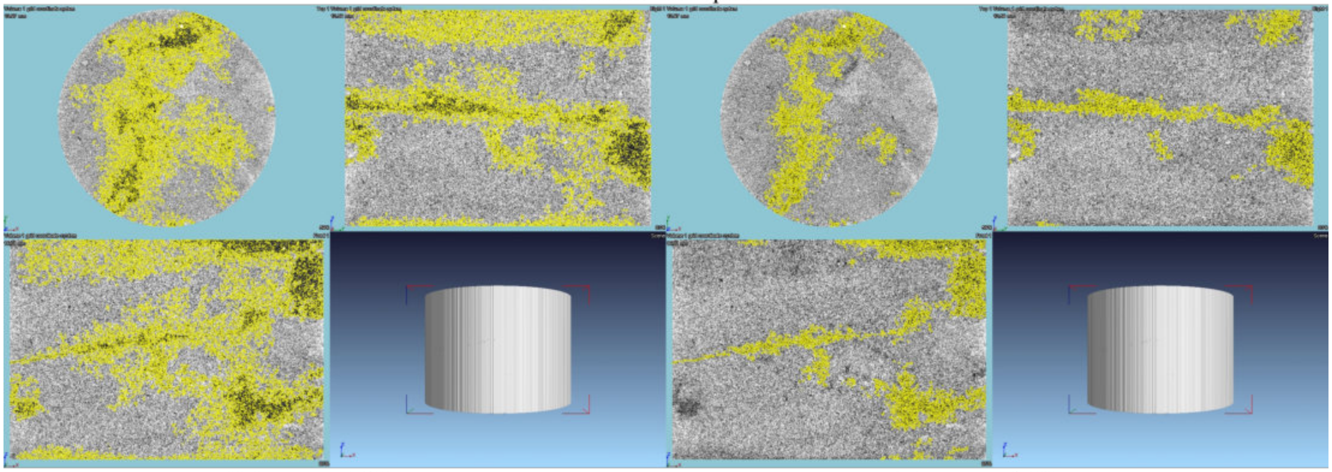

Tolerance = 1500

Tolerance = 1000

Figure 6.19: Micro CT imaging of Sample 201. The top image shows the picture of the sample together with a preview of the image. The bottom picture shows the connectivity of the pores when the tolerance set on the software of is 1500 and 1000.

Figure 6.19 shows Samples 201. This samples is comprised by fine-grained sandstone and silt. It is unclear if the darker brown spots are only in the surface of the sample or if they correspond to the silty material since their distribution is not clear in the Micro CT image. This sample was quite cohesive to the touch and the calculated porosity was of 14.5%, which was reflected in the high values of the tolerance needed to increase the connectivity of the pores, as we can see in the bottom image. The yellow areas corresponding to the connected void space (dark colors in the Micro CT image) have a limited vertical connectivity. In order to see a change on this connectivity, the tolerance was decreased to 1000. For this tolerance, the vertical and horizontal connectivity decrease significantly.

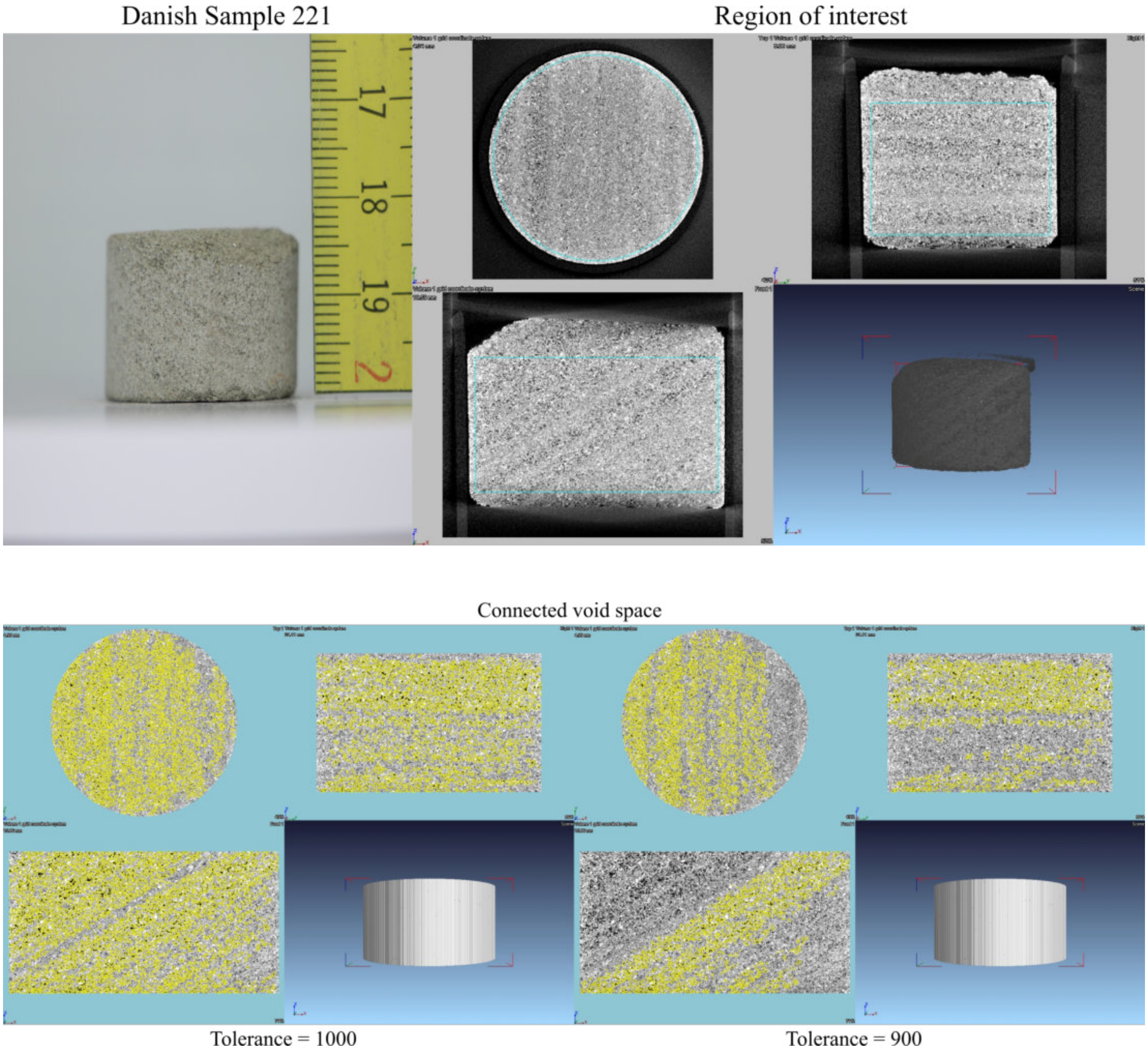

Figure 6.20: Micro CT imaging of Sample 221. The top image shows the picture of the sample together with a preview of the image. The bottom picture shows the connectivity of the pores when the tolerance set on the software of is 1000 and 900.

Finally, a more homogeneous sample is presented in Figure 6.20. Sample 221 is composed by a fine- to medium-grained sandstone from which bedding is visible with bare eye and more clearly in the Micro CT image. The high porosity (34%) and the cohesion of this sample being 'weak' to the touch, translated into a lower value of the tolerance needed to observe a change on the connected porosity. This connected porosity follows the bedding of the samples vertically and horizontally, as shown in the bottom image of Figure 6.20.

Appendix F displays the Micro CT images of Danish samples 1, 8, 12, 13, 117, and 137.

7 Discussion

The results obtained from the laboratory experiments were compared to literature data found for different reservoirs of the North Sea. Only geomechanical data obtained from reservoirs comprised of sandstones as the main lithology were taken into account for a better comparison with the geomechanical data measured in the laboratory.
The literature data were obtained from the Nederlandse Aardolie Maatschappij (NAM), Nederlandse Olie- en Gasportaal(NLOG), TNO, and various articles/reports: (Haug et al. (2018), B. Orlic et al. (2013), B. Orlic (2013), Bogdan Orlic (2016), Schutte (2019), Shell (2014), Shell (2016), and Staples et al. (2007)).
For the plots shown in Section 6, the literature data are added to study if the trends are maintained or if drastic changes are introduced.

7.1 Introduction of literature data

In this section of the discussion, a small description of each data point will be introduced to compare them with the testes samples from this thesis.
Starting from Haug et al. (2018), the target location described in this article was the Pompeckj block situated in North Germany. The reservoir from where data was extracted is formed by sandstones from the Upper Rotliegend Group at a depth of 4800 m. Their caprock consists on shales, carbonates and evaporites comprising the Zechstein Group. The geomechanical data from this paper could be potentially correlated to the German samples from this thesis.

Two of the three papers authored by Dr. Orlic (B. Orlic et al. (2013) and Bogdan Orlic (2016)), also target the Upper Rotliegend Group but in two different places of the Netherlands. First in B. Orlic et al. (2013) the depleted gas field under study was not specified, while in Bogdan Orlic (2016) the area of study was located in Zuid-Friesland. Both reservoirs are at about 2 km depth with an average porosity of 20-25%, and their caprock is the Zechstein Group. As with the article from Dr. Haug, the data from these papers could be compared directly to the German samples tested in this thesis.
The third paper by B. Orlic (2013), includes the geomechanical properties of five different fields in different models of the subsurface surrounding those fields. Three of the fields are located onshore and two offshore. The obtained geomechanical data corresponds to all the formations conforming the subsurface of those fields, but for this thesis, only the main sandstone formations were taken into account. Since no confined pressure data was provided, the comparison is restricted to plots regarding depth, porosity, and Poisson's ratio.

Schutte (2019) focused her MSc Thesis on the Cranberry field situated offshore in the Dutch Sector of the North Sea. The target formation is also part of the Upper Rotliegend Group and the depth of the reservoir is at 2.5 km with an average porosity of 10%. The caprock also corresponds to the Zechstein Group.
From Shell, two studies where carried out and described in the project reports Shell (2014) and Shell (2016). The first report corresponds to the Peterhead CCS Project which studies several samples from the Captain Fm. at the Goldeyene reservoir located in the northern part of the UK sector. Its caprock corresponds to the Rødby Fm. This depleted gas reservoir is located at 2.5 k deep with an average porosity of 25%. These sandstones were deposited from the effect of suspension after the collapse very dense turbidity currents (Allen et al. 2020).
On the second Shell report, the Endurance Structure on the UK sector is studied and the target formation is the Bunter Fm. Its depth is of 1300 m and the porosity is of 29%. This formation was deposited in aeolian and fluvial environments and shows interbedded playa margin silts and clays (Shell 2016).
Finally, from Staples et al. (2007) the target reservoir is located in the Shearwater Field in the U.K. Central North Sea, and corresponds to the Fulmar Fm. for which the caprock is Hod Chalk Fm. These sandstones were deposited in a shallow marine environment (Johnson et al. 1986).
In general, many cited papers/articles/reports studied the geomechanical behavior of different reservoirs in the North Sea, however, no data was provided that could be included in this thesis.

7.2 Static Young's modulus versus Confining Pressure

The data found in the literature are scattered points as shown in Figure 7.1. The different data points represent sandstones from the main formations studied in this thesis and from other target reservoirs from the SHARP project. The points cannot show a trend since they are singular measurements; however, their magnitudes fall in the range of trends of the tested data by TU Delft and NGI. The majority of confining pressures found in literature were lower than 20 MPa and some higher.

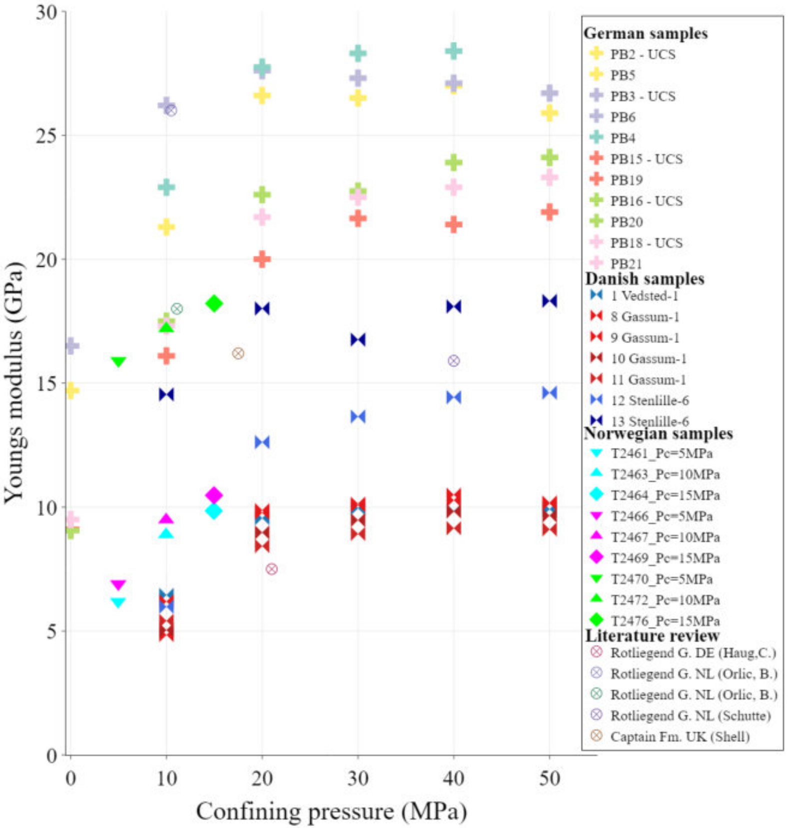

Figure 7.1: Young's modulus versus Confining Pressure for all data received, measured and found in literature (Haug et al. 2018; B. Orlic et al. 2013; Bogdan Orlic 2016; Schutte 2019; Shell 2014).

More geomechanical data would increase the quality of these trends and would help to create more precise predictions about the subsurface for activities involving injection of CO_2 to avoid the risks mentioned in the introduction (Section 3).

7.3 Depth versus Static Young's modulus

Figure 7.2 shows the data obtained from the laboratory experiments carried out at TU Delft and NGI and from the literature review. This figure includes a wide range of chronological time periods and discrete depositional environments for the different formations. It is important to understand that the mechanical behavior of the samples is directly linked to the burial history and the tectonic deformations shaping the samples (Douma et al. 2019) from the moment of their deposition of the sediment until the appearance they have in the present. Nevertheless, a general increase of the elastic modulus with depth can be inferred.

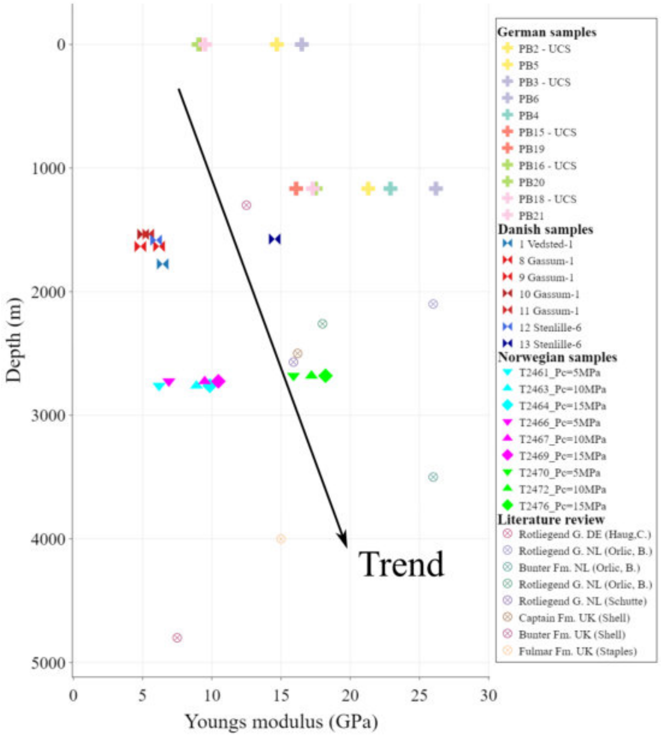

Figure 7.2: Depth versus static Young's modulus. This plot includes the samples tested at TU Delft and NGI as well as the data found in literature from reservoirs in the North Sea (Haug et al. 2018; B. Orlic et al. 2013; B. Orlic 2013; Bogdan Orlic 2016; Schutte 2019; Shell 2014; Shell 2016; Staples et al. 2007).

7.4 Static Young's modulus versus Porosity & Depth versus Porosity

Figure 7.3 includes the porosity from the literature as well as the measurements from the samples obtained from the NLOG (Aramis project). The plot to the left shows an overall decreasing trend of the porosity with depth. For the Young's modulus, the literature supports the trend followed by the laboratory tests being the decrease of Young's modulus with increasing porosity. This trend was also studied by Ramm (1992) for sandstones in different reservoirs from the coast of Norway which were deposited during the Jurassic. The mechanical compaction that these sediments experienced during their burial period led to a relocation and fracturing of the grains, decreasing the original void space. The overburden increased the pressure and depending on the geological context, the temperature, which induced chemical compaction, filling the pores with cement and with plastically deformed grains.

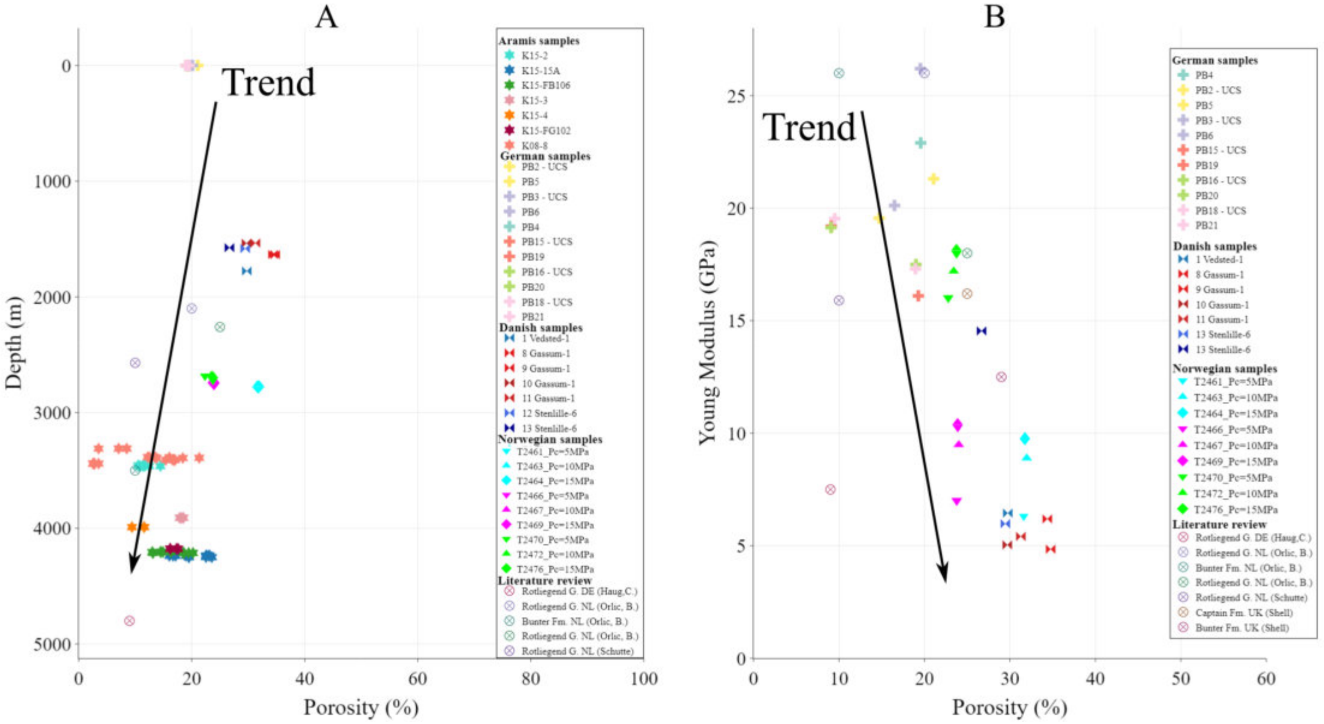

Figure 7.3: Porosity and elastic modulus change with depth. Data included from NAM and literature (Haug et al. 2018; B. Orlic et al. 2013; B. Orlic 2013; Bogdan Orlic 2016; Schutte 2019; Shell 2014; Shell 2016; Staples et al. 2007).

7.5 Dynamic versus Static Young's modulus

Acoustic data gathered from the wells located over the Netherlands (see Figure 5.6) by TNO include the dynamic Young's modulus of different formations as shown in Figure 7.4. From these formations, only the sandstone data are used in comparison to the tested data (right figure).

Figure 7.5 shows the static and dynamic modulus of elasticity versus depth obtained from TNO, the literature, NGI, and TU Delft. The main trend suggests an increase of the Young's modulus with increasing depth (note: depth increases downwards in the figure). This increase is related to the increasing confinement that the rocks are experiencing which is correlated to Figure 7.1.

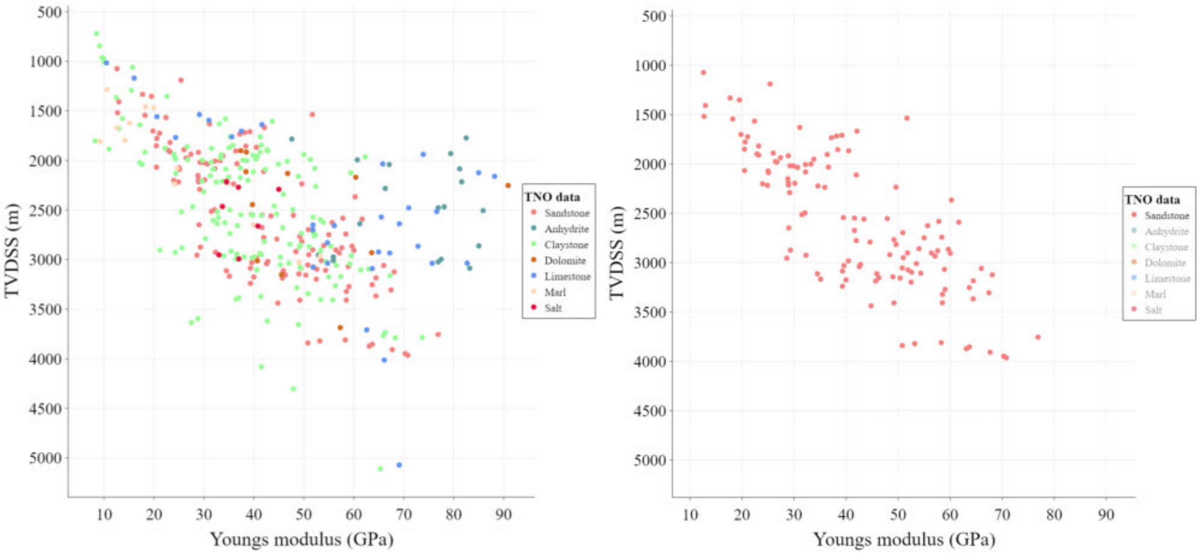

Figure 7.4: Left: Dynamic Young's modulus from different lithologies and formations. Right: filtered data showing only the elastic modulus from the sandstone formations.

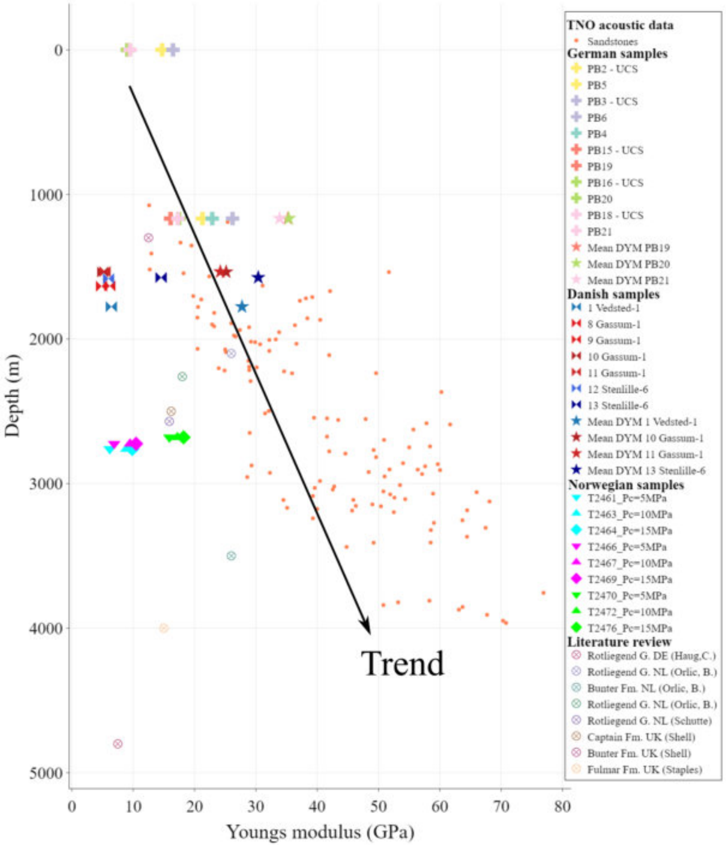

Figure 7.5: Static (SYM) and dynamic (DYM) Young's modulus versus Depth. The SYM of the Danish and German samples depicted have a P_c = 10 MPa.

7.6 Dynamic and Static Poisson's ratio

Figure 7.6 shows the data from the results section compared to the data found in the literature about the Poisson's ratio. The data from the literature review falls into the same ranges of those in the German and Norwegian SPR and DPR.

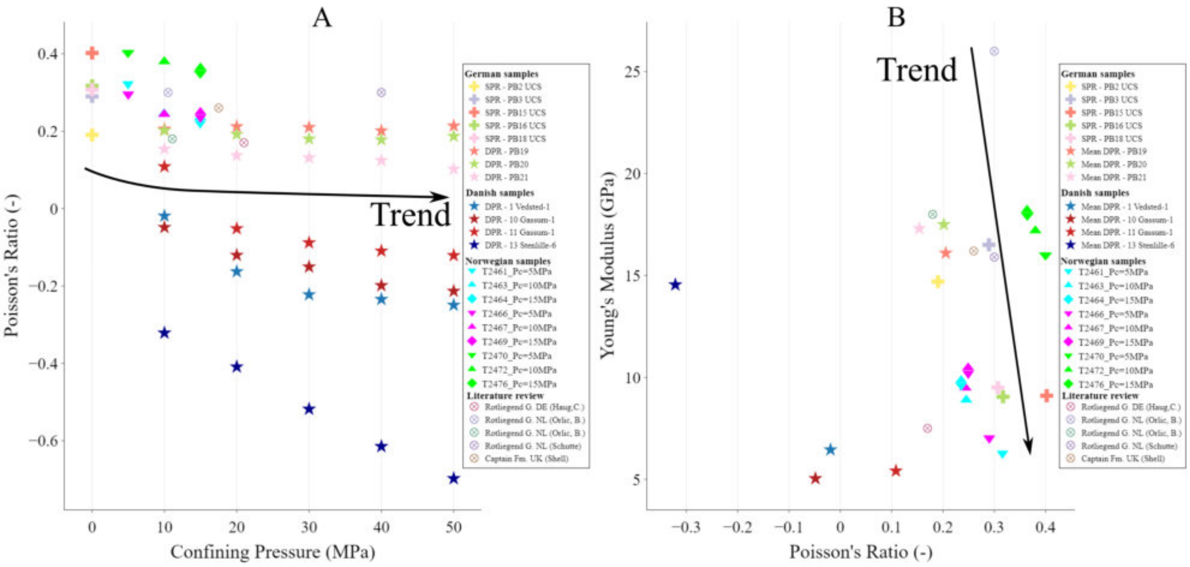

Figure 7.6: Poisson's ratio versus confining pressure (Plot A) and Young's modulus versus Poisson's ratio (Plot B). Includes data from the tested samples at TU Delft Laboratory, at NGI and from literature review (Haug et al. 2018; B. Orlic et al. 2013; Bogdan Orlic 2016; Schutte 2019; Shell 2014).

The use of compressional and shear waves velocities to calculate the DPR brought a characteristic problem which it is visible in Figures 6.17 and 7.6 where the DPR magnitudes of the Danish samples are negative even though that the same method as for the German samples was use to calculate it. Since this calculation is based on the wave velocities, the negative values are also related to the velocities. The average V_p/V_s ratio for wet sandstones ranges between 1.55 to 1.85 (Han et al. 1986). Taking into account that the waves measured from the tests done to the Danish samples were not very clear; the time arrivals of the waves were manually picked; and the small V_p/V_s ratio, any inaccurate picking could have caused the calculated negative values of DPR for the Danish samples.

7.7 Fulfillment of research question

The research question aimed to maximize the geomechanical information extracted from the collected samples within the constraints of time and equipment availability. To address this question, a combination of laboratory experiments and extensive literature review was conducted. These processes provided valuable insights into the property modifications of the samples when subjected to various testing methods. Sections 6 and 7 focused on examining the elasticity variations using the mechanical techniques of unconfined compression tests and triaxial compression tests, as well as active-source acoustic methods using ultrasonic waves. These investigations yielded diverse findings regarding the geomechanical behavior of the samples under different confining pressures. By comparing our results with literature findings from sandstone reservoirs across the North Sea region, common trends were identified. These consistent trends suggest that the obtained results can be incorporated into a subsurface model to make predictions about the geomechanical behavior of the studied reservoirs in Norway, Denmark, and Germany/Netherlands. Moreover, reservoirs with similar geological history as the ones tested in this thesis in different parts of the world, could benefit from these results if predictions about their geomechanical behavior are to be done.

One notable example where these geomechanical knowledge can potentially help the reduction of induced seismicity is in USA or Canada. Seismic events were triggered due to the injection of wastewater into the subsurface. By incorporating direct studies on the geomechanical properties of the reservoirs, more accurate predictions can be made regarding the available pore volume for fluid injection. This knowledge is crucial to prevent overpressure of the reservoir, thus minimizing the risk of induced seismic events. By improving our understanding of the reservoir's geomechanical behavior, we can enhance the safety and effectiveness of CCS projects, ultimately benefiting both the environment and human lives (Verdon et al. 2016).

8 Conclusions and Recommendations

In this study, the geomechanical properties of 27 samples coming from different reservoirs and outcrops of the northern regions of Europe were obtained via the following laboratory experiments:

- Brazilian test.
- Unconfined Compressive Strength.
- Triaxial compression.
- Active-source acoustics.

The main objective was to determine the geomechanical properties to better understand the limitations of different formations and to reduce the risks linked to subsurface activities of CO_2 injection for storage purposes.

8.1 Conclusions

The main conclusions taken out of the test results and gathered data are as follows:

- From the results, it can be observed that the stiffness of the sandstones increases with rising confining pressure. This change increases significantly at lower confining pressures while at higher confinement, the elasticity seems to plateau, or the increasing rate decreases.
- Upon non-critical fracture of a sample, the elasticity decreases (e.g. third P_c of sample 13 after a small fissure occurred in the second cycle).
- The static and dynamic elastic modulus follow similar trends while their magnitude differs due to the different methods used.
- The static and dynamic Young's modulus show an increasing trend with depth.
- The porosity clearly affects the elasticity of the rock: the Young's modulus increases with decreasing porosity. The porosity shows an expected decrease with depth. With depth, the confining pressure and overburden increase, and the elastic modulus tends to increase with higher confining pressures.
- The heterogeneities within the samples impact the elastic modulus of the samples. A clear indication of this effect can be seen in Figures 6.1, 6.4, and 7.3 where the differences in the Young's modulus are directly correlated to the contrast between the sandstones forming the samples. Samples composed by cleaner sandstones and a higher cohesion showed a high elastic modulus (German samples) while the more heterogeneous samples showed lower elasticity. Thus, understanding the heterogeneity and its influence on mechanical behavior is important for accurate modeling and predicting the behavior of rock masses subjected to stress (Iakusheva et al. 2022).
- The yield strength of the sample increases linearly with the increasing confining pressure.
- The P and S wave velocities show a change of trend when surpassing the yield point, generally plateauing or decreasing. This could be a useful insight for potential predictions through sonic logging of the rock deformation while injecting CO_2.
- Static and Dynamic Young's modulus are quantitatively different due to the different methods used to obtained the data. This is shown in an increased magnitude of the dynamic elastic modulus compared to the static.
- The Poisson's ratio decreases with increasing confining pressure due to the compaction that the sample experienced after each stress cycle. This also indicates that the samples become stiffer at higher confining pressures.
- The methodology followed since receiving the samples until testing is essential in order to collect a more comparable data. In this case, the sample dimensions set a main discrepancy. The samples obtained from GEUS were too small for the hoek cell and certain alternatives were taken. A rubber sleeve between sample and the sleeve holding the confining fluid was placed. This could have modified the registration of some data such as the active-acoustic measurements. Nevertheless, the data obtained from these samples was similar to the Norwegian data which have alike dimensions.

8.2 Recommendations for future work

The laboratory experiments carried out at TU Delft were planned to obtain as much geomechanical information as possible from the sample for the given time and equipment. Based on the acquired experience, some recommendations could improve similar future studies:

- To obtain the best comparable data, ensuring all the samples have the same dimensions to prepare the test setups accordingly is an important insight taken from this thesis.
- To expand this knowledge, testing the samples as with the methods used in this thesis (saturated and dry) while injecting CO_2 could make an impact on the geomechanical behavior of the sample.
- The experiments reached the inelastic domain of the sample and, therefore, there was irreversible deformation done to the sample. This deformation was carried to the following cycles which could also be detrimental for the results. Following these experiments with fully elastic testing could give further insight about the change of the stiffness with increasing confining pressure.
- Adding more data to these plots will decrease uncertainties toward prediction-making.
- The data obtained from these experiments could be added to models of the subsurface targeting the areas of study.
- Acquiring the permeability of the samples also increase the knowledge about their properties and the flow followed by the fluid to inject.

9 Bibliography

Abdewi, Elfetori F. (2017). "Mechanical Properties of Reinforcing Steel Rods Produced by Zliten Steel Factory". In: *Reference Module in Materials Science and Materials Engineering*. Elsevier. DOI: `10.1016/b978-0-12-803581-8.10362-5`.

Allen, Michael J., Daniel R. Faulkner, Richard H. Worden, Elliot Rice-Birchall, Nikolaos Katirtsidis, and James E.P. Utley (Mar. 2020). "Geomechanical and petrographic assessment of a CO2 storage site: Application to the Acorn CO2 Storage Site, offshore United Kingdom". In: *International Journal of Greenhouse Gas Control* 94. ISSN: 17505836. DOI: `10.1016/j.ijggc.2019.102923`.

Asef, Mohammad Reza and Ali Reza Najibi (2013). "The effect of confining pressure on elastic wave velocities and dynamic to static Young's modulus ratio". In: *Geophysics* 78.3, pp. D135–D142. ISSN: 19422156. DOI: `10.1190/GEO2012-0279.1`.

Brown, E.T. (2015). "The ISRM Suggested Methods for Rock Characterization, Testing and Monitoring: 2007-2014". In: *Pergamon Press 1981, pages 119 to 121*. DOI: `10.1007/978-3-319-07713-0`.

Cocks, L R M and T H Torsvik (2006). *European geography in a global context from the Vendian to the end of the Palaeozoic*. Tech. rep.

Cooper, B S, P E Barnard, and N Telnaes (1995). *The Kimmeridge Clay Formation of The North Sea*. Tech. rep.

Coward, M P (1995). *Permian and Triassic Rifting in Northwest Europe*. Tech. rep., pp. 7–39. URL: `https://www.lyellcollection.org`.

De Jager, Jan (2007). *Petroleum geology Petroleum system analysis View project Trap and Seal assessment View project*. Tech. rep. URL: `https://www.researchgate.net/publication/312604683`.

Douma, Lisanne A.N.R., Jaap A. Regelink, Giovanni Bertotti, Quinten D. Boersma, and Auke Barnhoorn (Oct. 2019). "The mechanical contrast between layers controls fracture containment in layered rocks". In: *Journal of Structural Geology* 127. ISSN: 01918141. DOI: `10.1016/j.jsg.2019.06.015`.

Fjerseth, R B, B.-E Knudsen, T Liljedahl, P S Midboe, and B Soderstrom (1997). *Oblique rifting and sequential faulting in the Jurassic development of the northern North Sea*. Tech. rep. 10, pp. 1285–1302.

Fossen, Haakon, Jonny Hesthammer, Tord Erlend Skeie Johansen, and Trond Olav Sygnabere (2003). "Structural geology of the Huldra Field, northern North Sea-a major tilted fault block at the eastern edge of the Horda Platform". In: *Marine and Petroleum Geology* 20.10, pp. 1105–1118. ISSN: 02648172. DOI: `10.1016/j.marpetgeo.2003.07.003`.

Gast, Reinhard, Michiel Dusar, Christoph Breitkreuz, Reinhard Gaupp, Jörg W. Schneider, Lars Stemmerik, Mark Geluk, Marion Geißler, Hubert Kiersnowski, Ken Glennie, Sander Kabel, and Neil Jones (2010). *Rotliegend dune-sandstones in the Sventesius*. Tech. rep.

Geluk, Mark (Marinus Cornelis) (2005). *Stratigraphy and tectonics of Permo-Triassic basins in the Netherlands and surrounding areas*. s.n.] ISBN: 9039339112.

Han, De-Hua, A Nur, and Dale Morqan (1986). *Effects of porosity and clay content on wave velocities in sandstones*. Tech. rep. 11. URL: `http://library.seg.org/`.

Hannah Ritchie, Max Roser, and Pablo Rosado (2022). *Energy*. URL: `https://ourworldindata.org/energy`.

Haug, C., J.-A. Nüchter, and A. Henk (Dec. 2018). "Assessment of geological factors potentially affecting production-induced seismicity in North German gas fields". In: *Geomechanics for Energy and the Environment* 16, pp. 15–31. ISSN: 23523808. DOI: `10.1016/j.gete.2018.04.002`. URL: `https://linkinghub.elsevier.com/retrieve/pii/S2352380818300030`.

He, Wang, Zhijun Yang, Hengheng Du, Jintao Hu, Ke Zhang, Weisheng Hou, and Hongwei Li (Aug. 2022). *Micro-Mechanisms and Implications of Continental Red Beds*. DOI: `10.3390/min12080934`.

Hunfeld, L B, J P T Foeken, and B M M Van Kempen (2021). *Geomechanical parameters derived from compressional and shear sonic logs for main geothermal targets in The Netherlands*. Tech. rep. URL: `www.nlog.nl,`.

Iakusheva, Regina, Israa Abu-Mahfouz, Muhammad Usman, Thomas Finkbeiner, and Volker Vahrenkamp (2022). "Understanding the Mechanical Properties Heterogeneity of Immature Source Rocks." In: *International Geomechanics Symposium: The Role of Geomechanics in Energy Efficiency and Energy Sustabiliity*.

Johnson, Howard D, Thomas A Mackayt, and David J Stewart (1986). *Ltd Marine and Petroleum Geology*. Tech. rep.

Kombrink, Henk and Stefano Patruno (2022). "The integration of public domain lithostratigraphic data into a series of cross-border North Sea well-penetration maps". In: *Geological Society Special Publication*. Vol. 494. 1. Geological Society of London, pp. 85–116. DOI: `10.1144/SP494-2020-25`.

Labuz, Joseph F. and Arno Zang (Nov. 2012). "Mohr-Coulomb failure criterion". In: *Rock Mechanics and Rock Engineering* 45.6, pp. 975–979. ISSN: 07232632. DOI: `10.1007/s00603-012-0281-7`.

Le Treut, Hervé, Richard Somerville, Ulrich Cubasch, M Allen, Le Treut, R Somerville, U Cubasch, Y Ding, C Mauritzen, A Mokssit, T Peterson, M Prather, M Marquis, KB Averyt, and M Tignor (2007). *Historical Overview of Climate Change Science Coordinating Lead Authors: Lead Authors: Contributing Authors: This chapter should be cited as.* Tech. rep.

Li, Qiuping, Jie Liu, Shouqing Lu, Zaiquan Wang, Hao Wang, Yimeng Wu, Yupu Wang, Di Ying, and Mingjie Li (Jan. 2023). "Influence of Confining Pressure on Nonlinear Failure Characteristics of Coal Subjected to Triaxial Compression". In: *International Journal of Environmental Research and Public Health* 20.1. ISSN: 16604601. DOI: `10.3390/ijerph20010105`.

Marjanac, Tihomir and Ronald J Steel (1997). *Dunlin group sequence stratigraphy in the northern North Sea: a model for Cook Sandstone Deposition South China Sea View project River deltas prograding in tidal seaways and straits: towards a conceptual depositional model View project.* Tech. rep. URL: `https://www.researchgate.net/publication/241974165`.

Martin-Roberts, Emma, Vivian Scott, Stephanie Flude, Gareth Johnson, R. Stuart Haszeldine, and Stuart Gilfillan (Nov. 2021). *Carbon capture and storage at the end of a lost decade.* DOI: `10.1016/j.oneear.2021.10.002`.

Mavko, Gary, Tapan Mukerji, and Jack Dvorkin (1998). *The rock physics handbook: tools for seismic analysis in porous media.* Cambridge University Press. ISBN: 0521620686.

Nazeer, Adeel, Shabeer Ahmed Abbasi, and Sarfraz Hussain Solangi (Nov. 2016). "Sedimentary facies interpretation of Gamma Ray (GR) log as basic well logs in Central and Lower Indus Basin of Pakistan". In: *Geodesy and Geodynamics* 7.6, pp. 432–443. ISSN: 16749847. DOI: `10.1016/j.geog.2016.06.006`.

Olivarius, Mette, Anja Sundal, Rikke Weibel, Ulrik Gregersen, Irfan Baig, Tonny B. Thomsen, Lars Kristensen, Helge Hellevang, and Lars Henrik Nielsen (Dec. 2019). "Provenance and Sediment Maturity as Controls on CO2 Mineral Sequestration Potential of the Gassum Formation in the Skagerrak". In: *Frontiers in Earth Science* 7. ISSN: 22966463. DOI: `10.3389/feart.2019.00312`.

Oraee-Mirzamani, Behdeen, Tim Cockerill, and Zen Makuch (2013). "Risk assessment and management associated with CCS". In: *Energy Procedia.* Vol. 37. Elsevier Ltd, pp. 4757–4764. DOI: `10.1016/j.egypro.2013.06.385`.

Orlic, B. (2013). "Site-specific geomechanical modeling for predicting stress changes around depleted gas reservoirs considered for CO2 storage in the Netherlands". In: URL: `http://onepetro.org/ARMAUSRMS/proceedings-pdf/ARMA13/All-ARMA13/ARMA-2013-446/1526831/arma-2013-446.pdf/1`.

Orlic, B., B.B.T. Wassing, and C.R. Geel (2013). "Field-scale geomechanical modeling for prediction of fault stability during underground gas storage operations in a depleted gas field in the Netherlands". In: URL: `http://onepetro.org/ARMAUSRMS/proceedings-pdf/ARMA13/All-ARMA13/ARMA-2013-300/1526580/arma-2013-300.pdf/1`.

Orlic, Bogdan (Dec. 2016). "Geomechanical effects of CO 2 storage in depleted gas reservoirs in the Netherlands: Inferences from feasibility studies and comparison with aquifer storage". In: *Journal of Rock Mechanics and Geotechnical Engineering* 8.6, pp. 846–859. ISSN: 16747755. DOI: `10.1016/j.jrmge.2016.07.003`. URL: `https://linkinghub.elsevier.com/retrieve/pii/S167477551630141X`.

Patruno, Stefano, Henk Kombrink, and Stuart G. Archer (2022). "Cross-border stratigraphy of the Northern, Central and Southern North Sea: a comparative tectono-stratigraphic megasequence synthesis". In: *Geological Society Special Publication.* Vol. 494. 1. Geological Society of London, pp. 13–83. DOI: `10.1144/SP494-2020-228`.

Pol -, E, A Di Masso, A Castrechini, M R Bonet, and T Vidal (2006). "Psychological parameters to understand and manage the NIMBY effect Parametres psychosociaux pour la comprehension et la gestion de I' effet NIMBY". In: DOI: `10.1016/j`. URL: `http:!`.

Pörtner, H.-O., D.C. Roberts, M. Tignor, E.S. Poloczanska, K. Mintenbeck, A. Alegría, M. Craig, S. Langsdorf, S. Löschke, V. Möller, A. Okem, and B. Rama (2022). *Climate Change 2022: Impacts, Adaptation, and Vulnerability.* Tech. rep. IPCC.

Rafiei Renani, Hossein and C. Derek Martin (June 2018). "Cohesion degradation and friction mobilization in brittle failure of rocks". In: *International Journal of Rock Mechanics and Mining Sciences* 106, pp. 1–13. ISSN: 13651609. DOI: `10.1016/j.ijrmms.2018.04.003`.

Ramm, Mogens (1992). *Porosity-depth trends in reservoir sandstones: theoretical models related to Jurassic sandstones offshore Norway.* Tech. rep.

Sayers, Colin M and De-Hua Han (2002). *The effect of pore fluid on the stress-dependent elastic wave velocities in sandstones.* Tech. rep. URL: `http://library.seg.org/`.

Schack Pedersen, Stig A and Peter Gravesen (2010). *Low-and intermediate level radioactive waste from Risø, Denmark. Location studies for potential disposal areas. Report no. 3 Geological setting and tectonic framework in Denmark GEOLOGICAL SURVEY OF DENMARK AND GREENLAND MINISTRY OF CLIMATE AND ENERGY.* Tech. rep.

Schutte, Lidewij (2019). “Geomechanical and Geochemical impact of CO 2 injection at the North Sea Cranberry Opportunity”. PhD thesis. Utrecht University.

Shell (2016). *K40: Subsurface Geoscience and Production Chemistry Reports.* Tech. rep. URL: `https://assets.publishing.service.gov.uk/government/uploads/system/uploads/attachment_data/file/531045/K40_Subsurface_Geoscience_and_Production_Chemistry.pdf`.

– (2014). *Peterhead CCS Project Document.* Tech. rep. URL: `https://assets.publishing.service.gov.uk/government/uploads/system/uploads/attachment_data/file/531054/Peterhead_11.115_-_Geomechanics_Report.pdf`.

Siggins, A. F. (1993). “Dynamic elastic tests for rock engineering”. In: *Comprehensive rock engineering. Vol. 3*, pp. 601–618. DOI: `10.1016/b978-0-08-042066-0.50030-6`.

Skurtveit, Elin and Lars Grande (2022). *SHARP Storage.*

Staples, Rob, Joel Ita, Rhian Burrell, and Rebecca Nash (2007). “Monitoring pressure depletion and improving geomechanical models of the shearwater field using 4D seismic”. In: *Leading Edge (Tulsa, OK)* 26.5, pp. 636–642. ISSN: 1070485X. DOI: `10.1190/1.2737120`.

STEMM-CCS (2016). *CCS reservoirs and CO 2 pathways.* Tech. rep. URL: `www.stemm-ccs.eu`.

Stewart, D J, M Schwander, and L Bolle (1995). *Jurassic depositional systems of the Horda Platform, Norwegian North Sea: practical consequences of applying sequence stratigraphic models.* Tech. rep.

Sundal, Anja, Johan Petter Nystuen, Kari Lise Rørvik, Henning Dypvik, and Per Aagaard (Nov. 2016). “The Lower Jurassic Johansen Formation, northern North Sea – Depositional model and reservoir characterization for CO2 storage”. In: *Marine and Petroleum Geology* 77, pp. 1376–1401. ISSN: 02648172. DOI: `10.1016/j.marpetgeo.2016.01.021`.

UNFCCC (2015). *Paris Agreement.* URL: `https://unfccc.int/process-and-meetings/the-paris-agreement/the-paris-agreement`.

Verdon, James P. and Anna L. Stork (Dec. 2016). “Carbon capture and storage, geomechanics and induced seismic activity”. In: *Journal of Rock Mechanics and Geotechnical Engineering* 8.6, pp. 928–935. ISSN: 16747755. DOI: `10.1016/j.jrmge.2016.06.004`.

Willems, Cees J.L., Andrea Vondrak, Harmen F. Mijnlieff, Marinus E. Donselaar, and Bart M.M. Van Kempen (2020). “Geology of the Upper Jurassic to Lower Cretaceous geothermal aquifers in the West Netherlands Basin - An overview”. In: *Geologie en Mijnbouw/Netherlands Journal of Geosciences* 99. ISSN: 15739708. DOI: `10.1017/njg.2020.1`.

Zhang, John J, Laurence Bentley, and Laurence R Bentley (2005). *Factors determining Poisson's ratio Seismic attributes analysis View project Factors determining Poisson's ratio.* Tech. rep., p. 1. URL: `https://www.researchgate.net/publication/265451756`.

10 List of figures and tables

List of Figures

List of Tables

Appendices

A Cross sections from Petrel data of GEUS

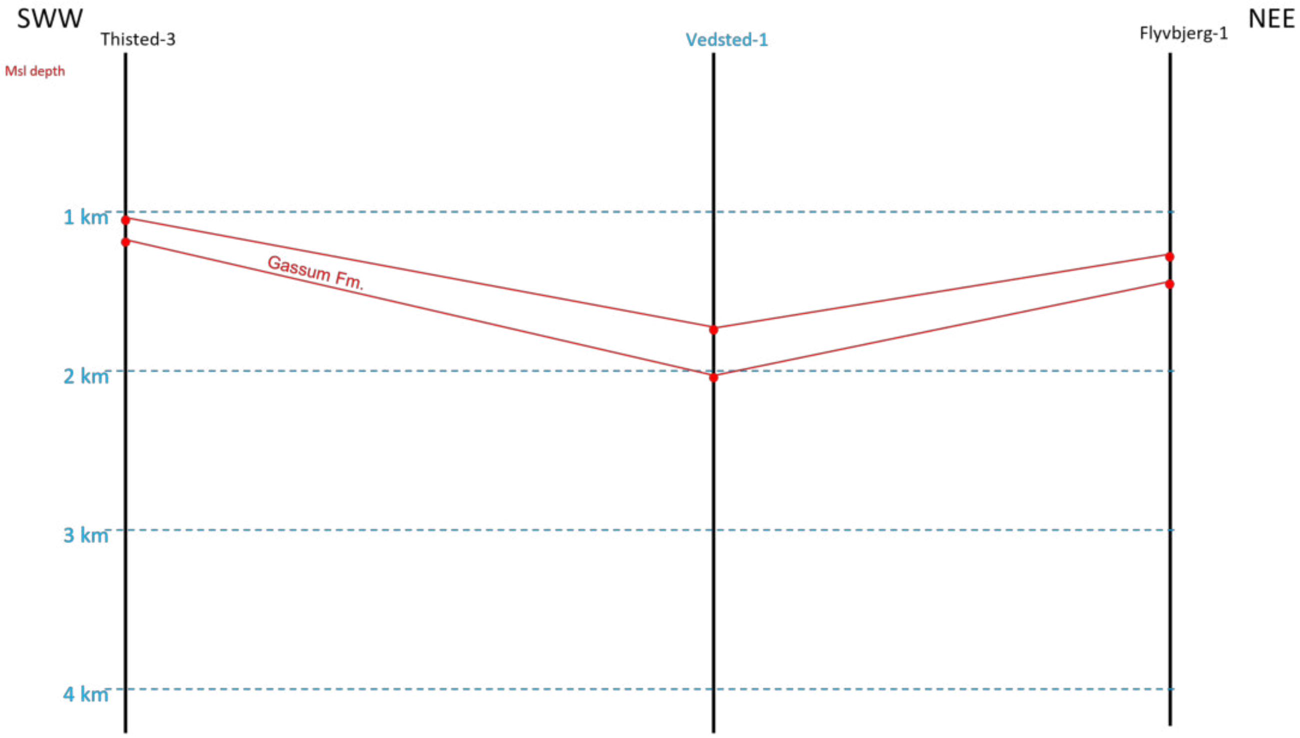

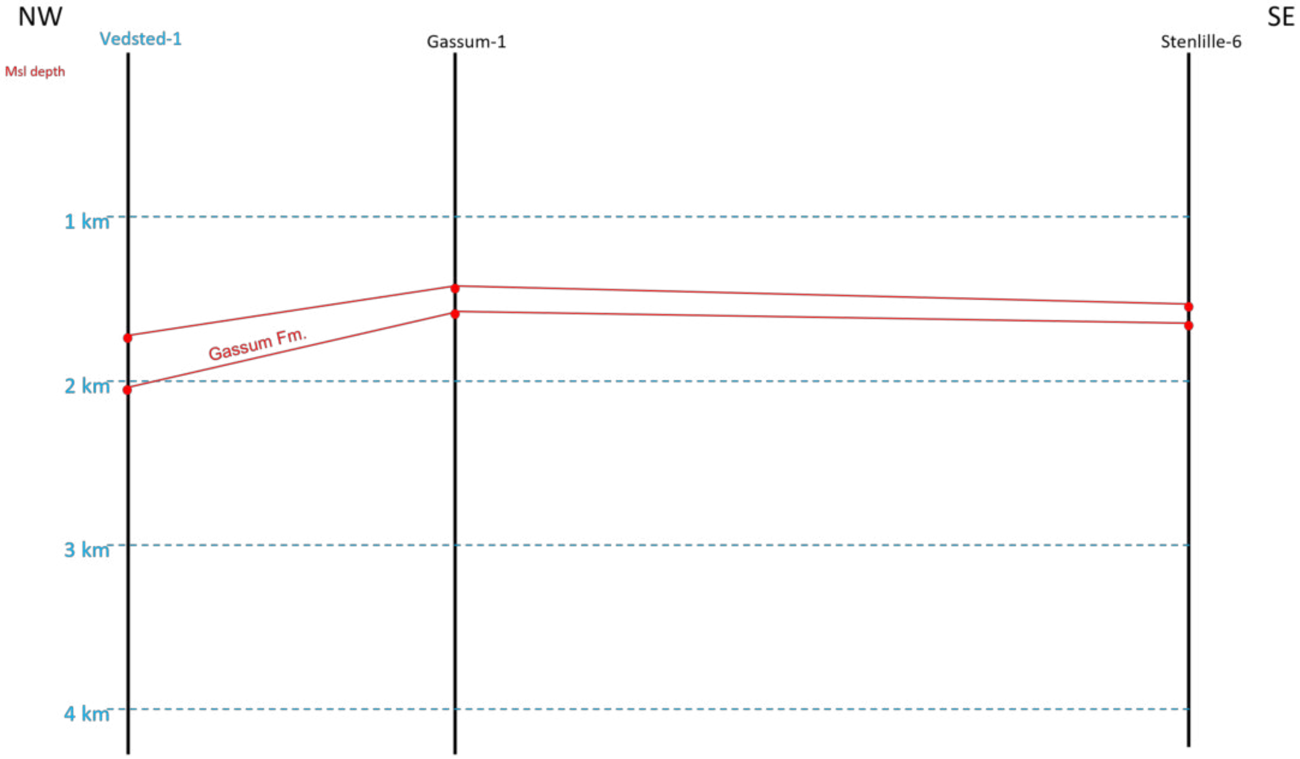

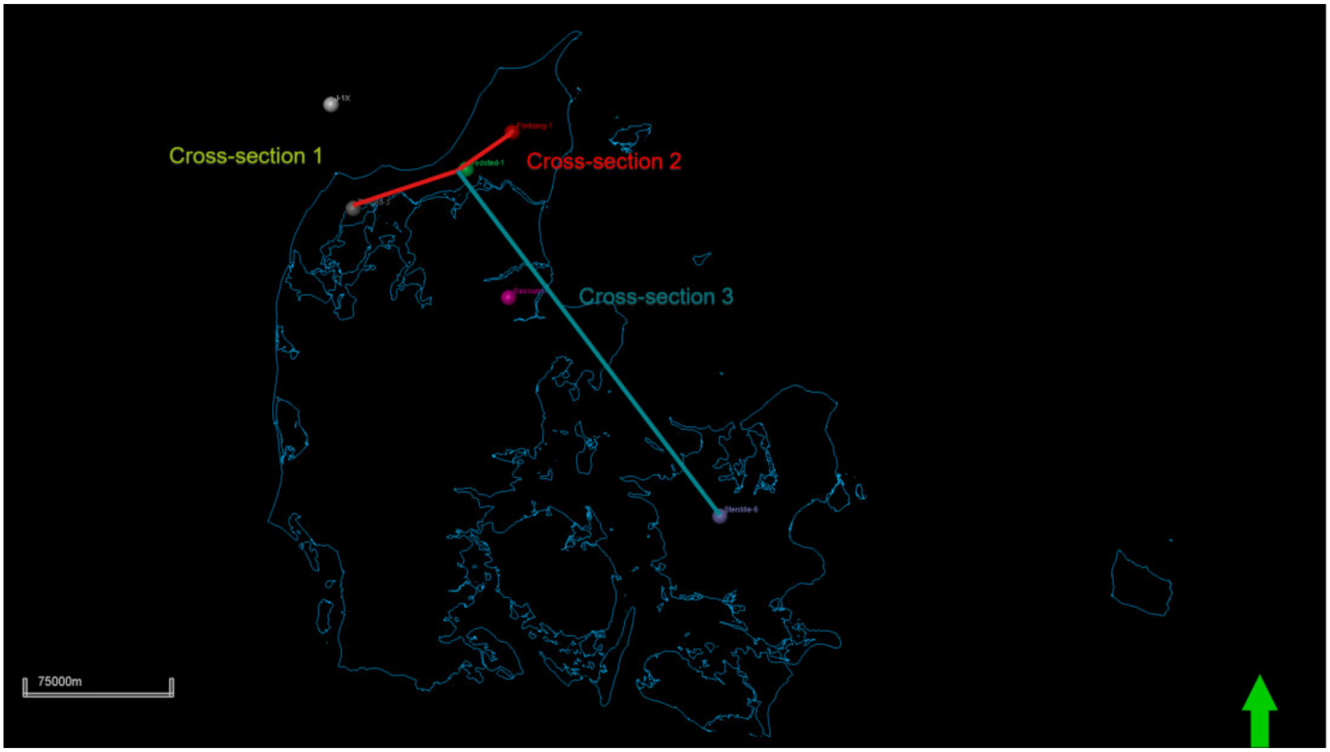
J-1X
Cross-section 1
Flyvbjerg-1
Vedsted-1
Cross-section 2
Cross-section 3
Stenlille-6
75000m

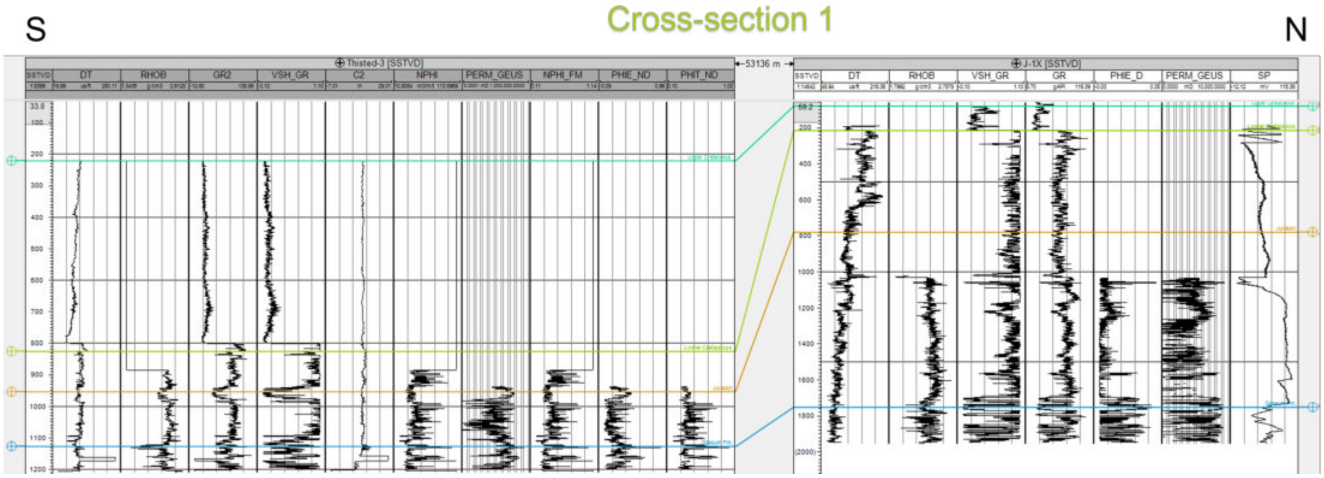
S
Cross-section 1
N
Thisted-3 [SSTVD]
53136 m
J-1X [SSTVD]
SSTVD
DT
RHOB
GR2
VSH_GR
C2
NPHI
PERM_GEUS
NPHI_FM
PHIE_ND
PHIT_ND
GR
PHIE_D
SP

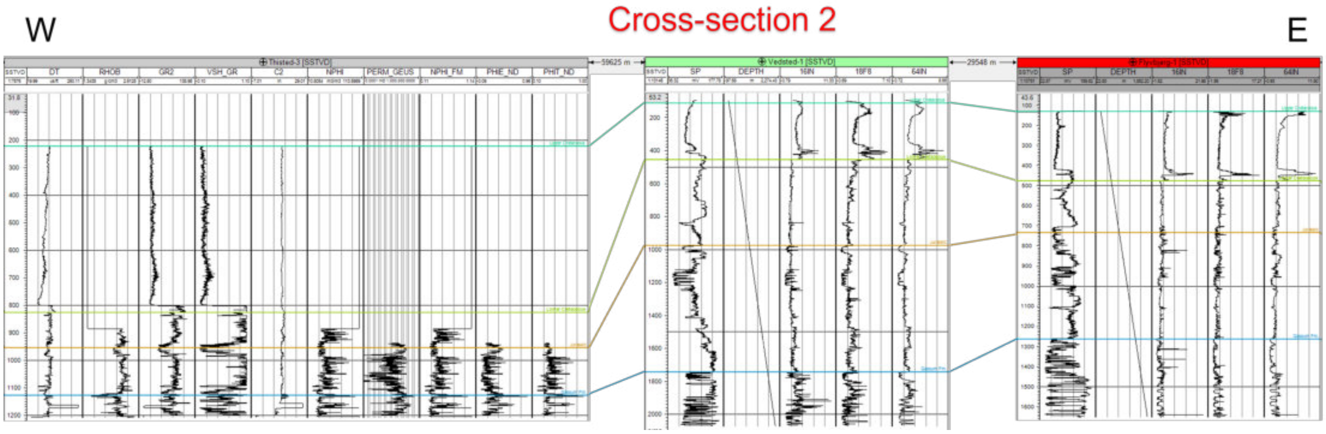
W
Cross-section 2
E
Thisted-3 [SSTVD]
59625 m
Vedsted-1 [SSTVD]
29548 m
Flyvbjerg-1 [SSTVD]
SSTVD
DT
RHOB
GR2
VSH_GR
C2
NPHI
PERM_GEUS
NPHI_FM
PHIE_ND
PHIT_ND
SP
DEPTH
16IN
18F8
64IN

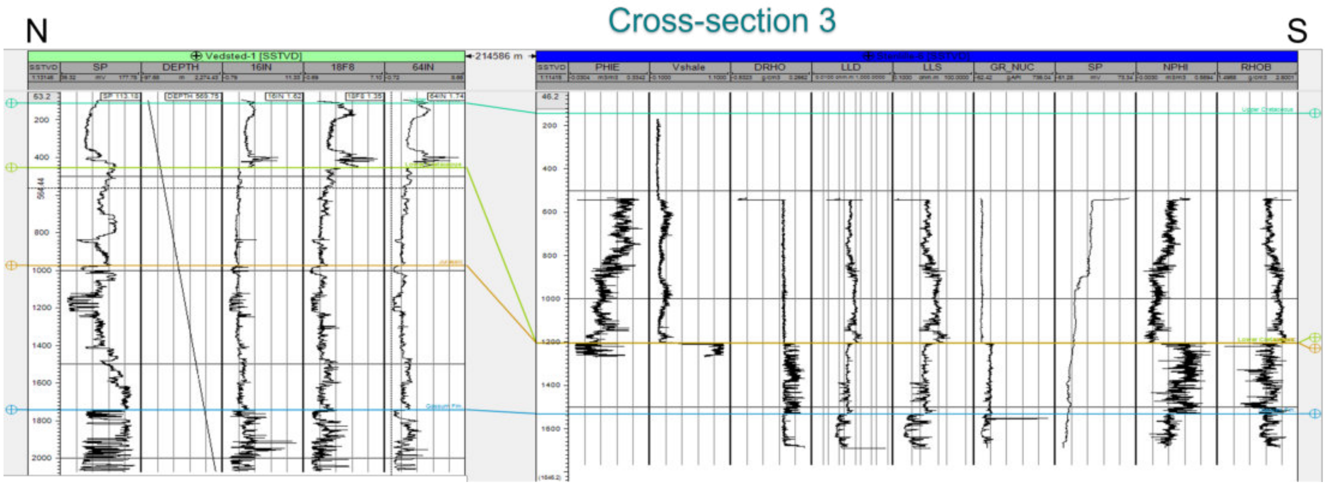
Cross-section 3
N
S
Vedsted-1 [SSTVD]
214586 m
SSTVD
SP
DEPTH
16IN
18F8
64IN
63.2
200
400
800
1000
1200
1400
1600
1800
2000
Lower Cretaceous
Jurassic
Gassum Fm.
Stenlille-6 [SSTVD]
PHIE
Vshale
DRHO
LLD
LLS
GR_NUC
SP
NPHI
RHOB
46.2
Upper Cretaceous
Lower Cretaceous

B Stress vs Strain plots

B.1 Brazilian disc test

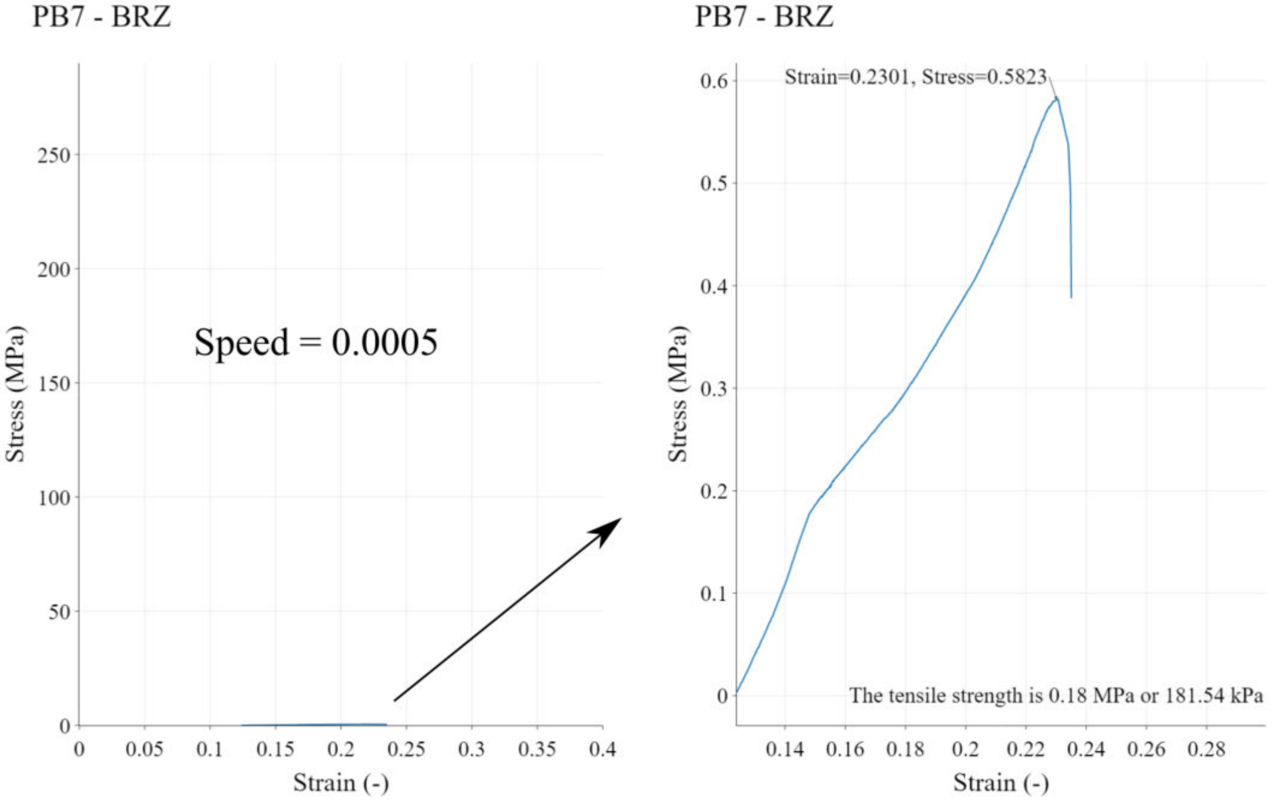

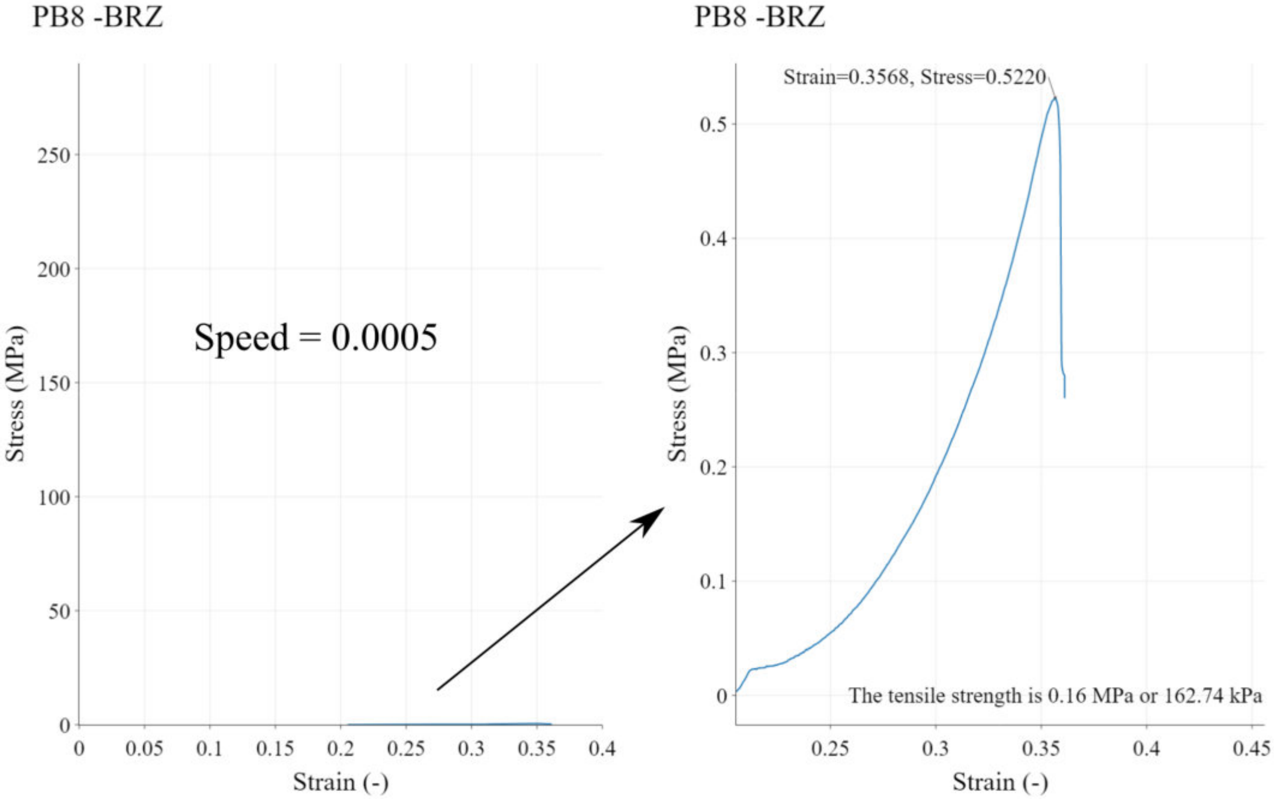

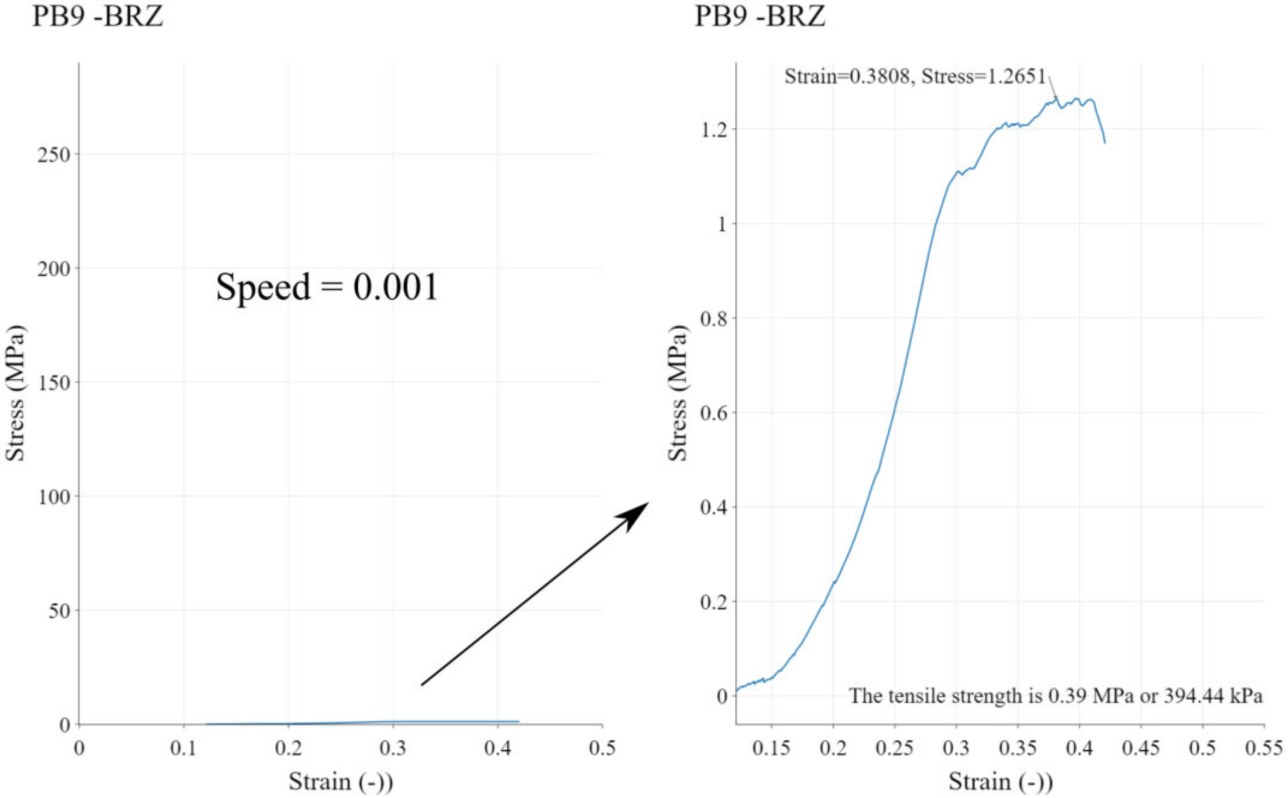
PB9 -BRZ

PB9 -BRZ

Speed = 0.001

Strain=0.3808, Stress=1.2651

The tensile strength is 0.39 MPa or 394.44 kPa

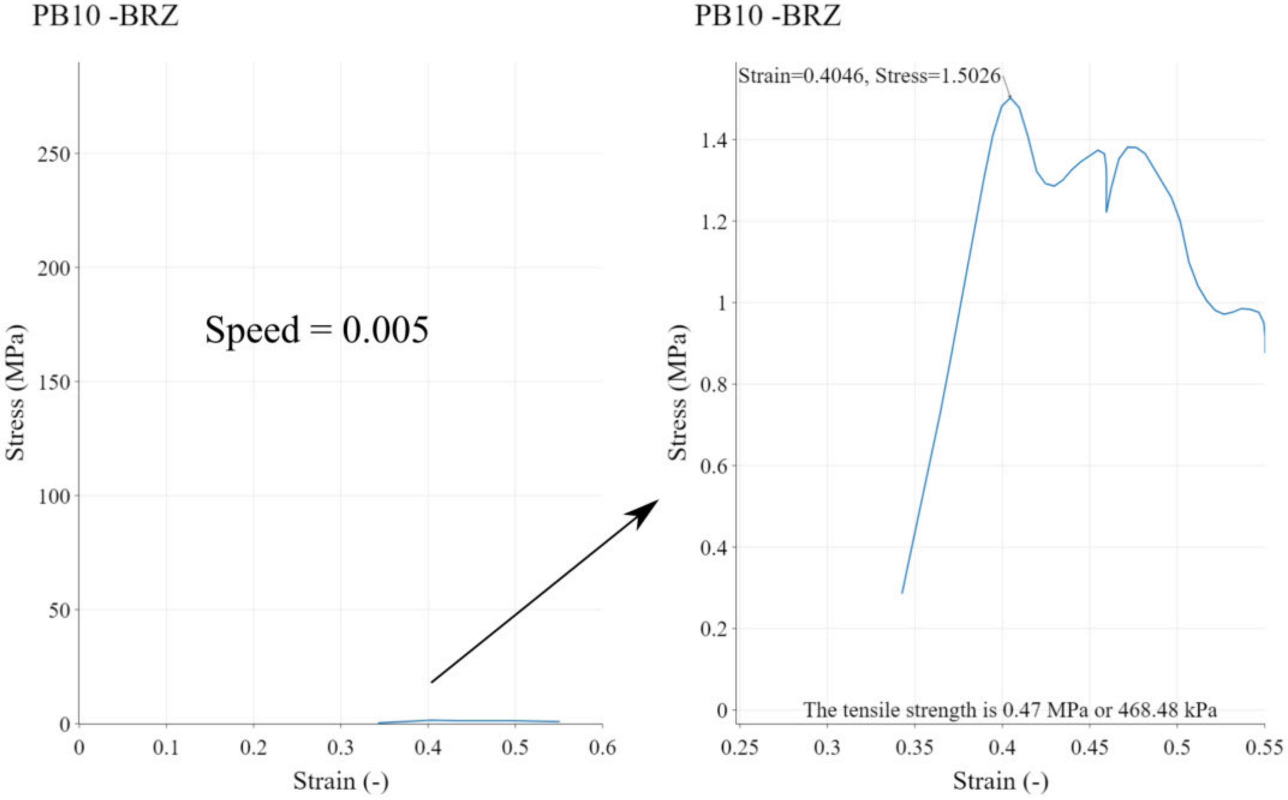
PB10 -BRZ

PB10 -BRZ

Speed = 0.005

Strain=0.4046, Stress=1.5026

The tensile strength is 0.47 MPa or 468.48 kPa

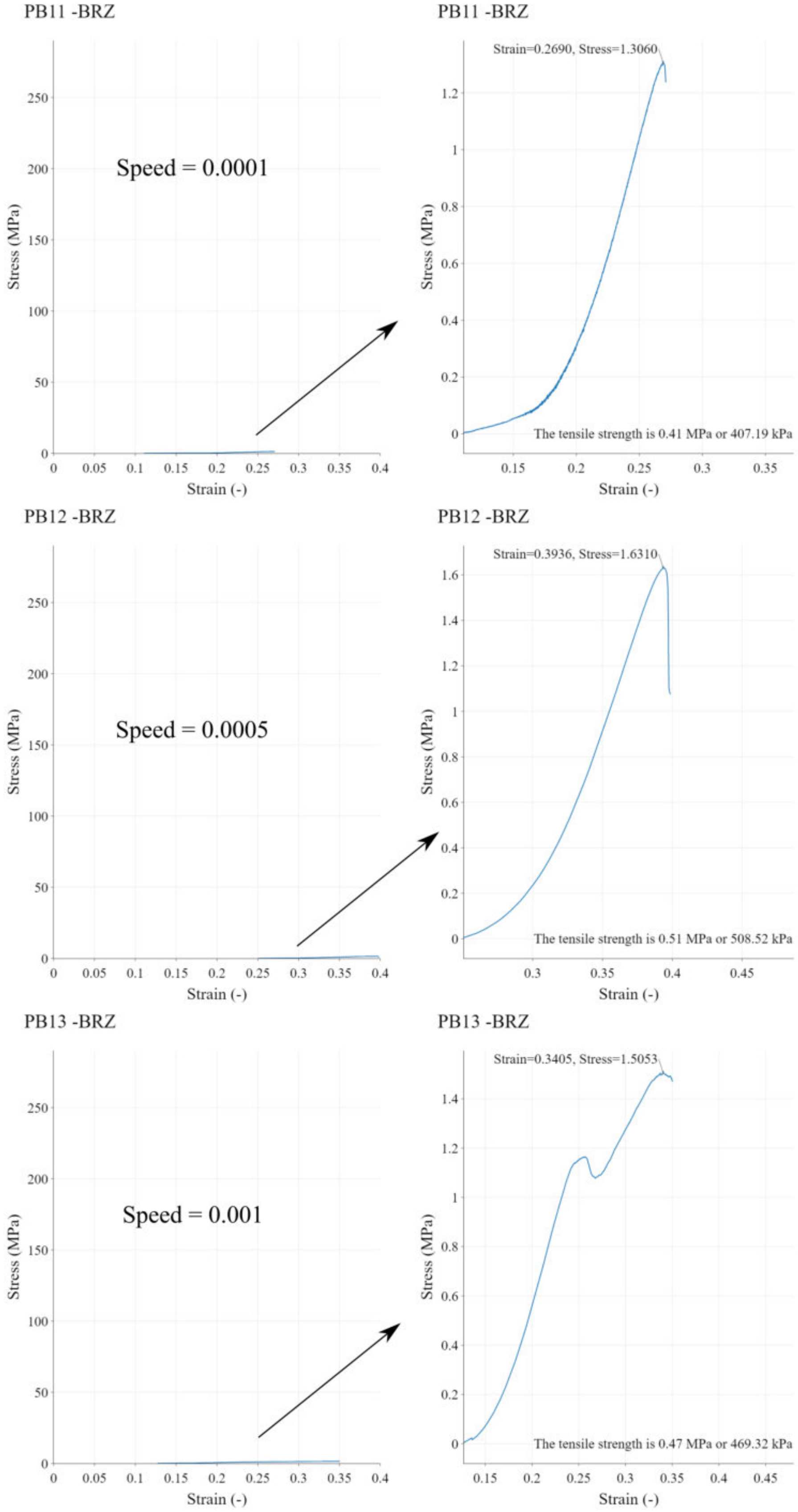

Figure B.1: Stress vs Strain plots of German samples

B.2 UCS and Triaxial test

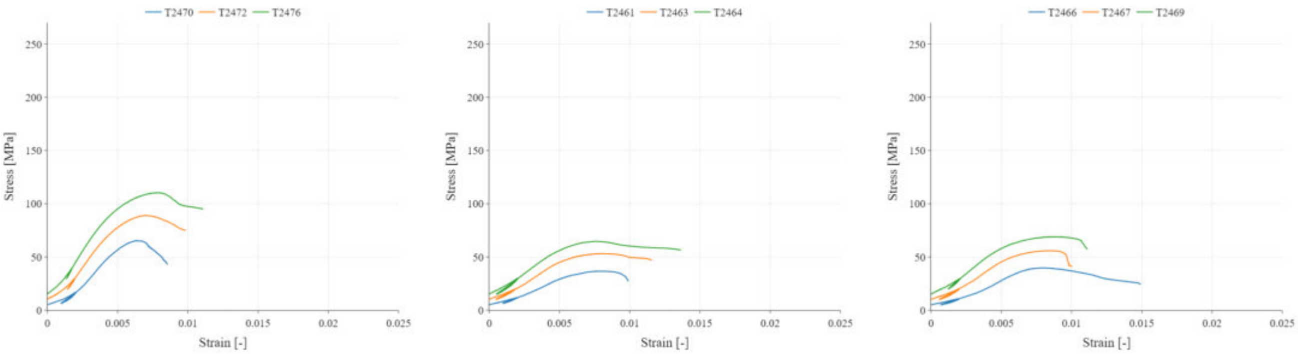

Figure B.2: Stress vs Strain plots of Norwegian samples

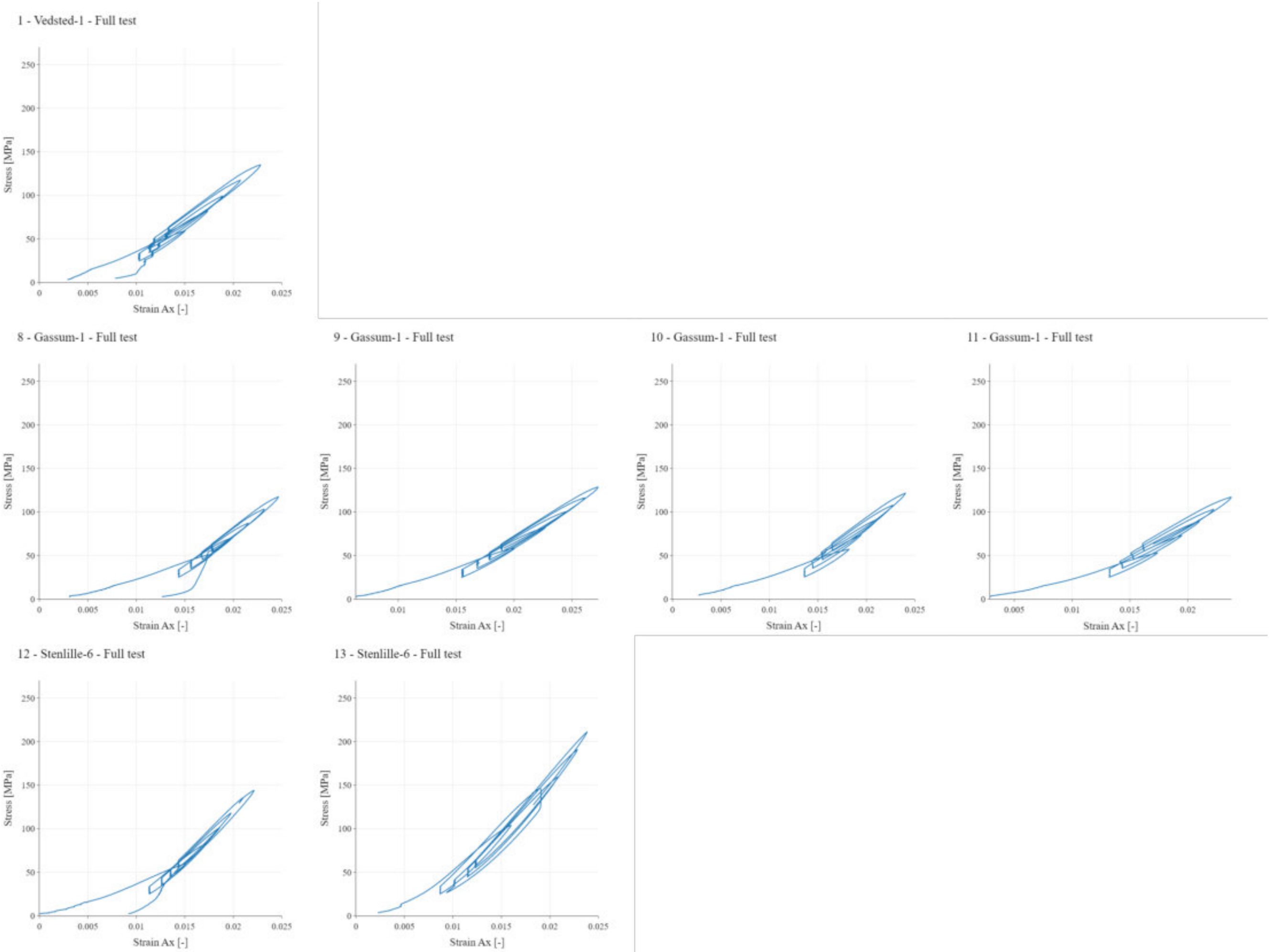

Figure B.3: Stress vs Strain plots of Danish samples

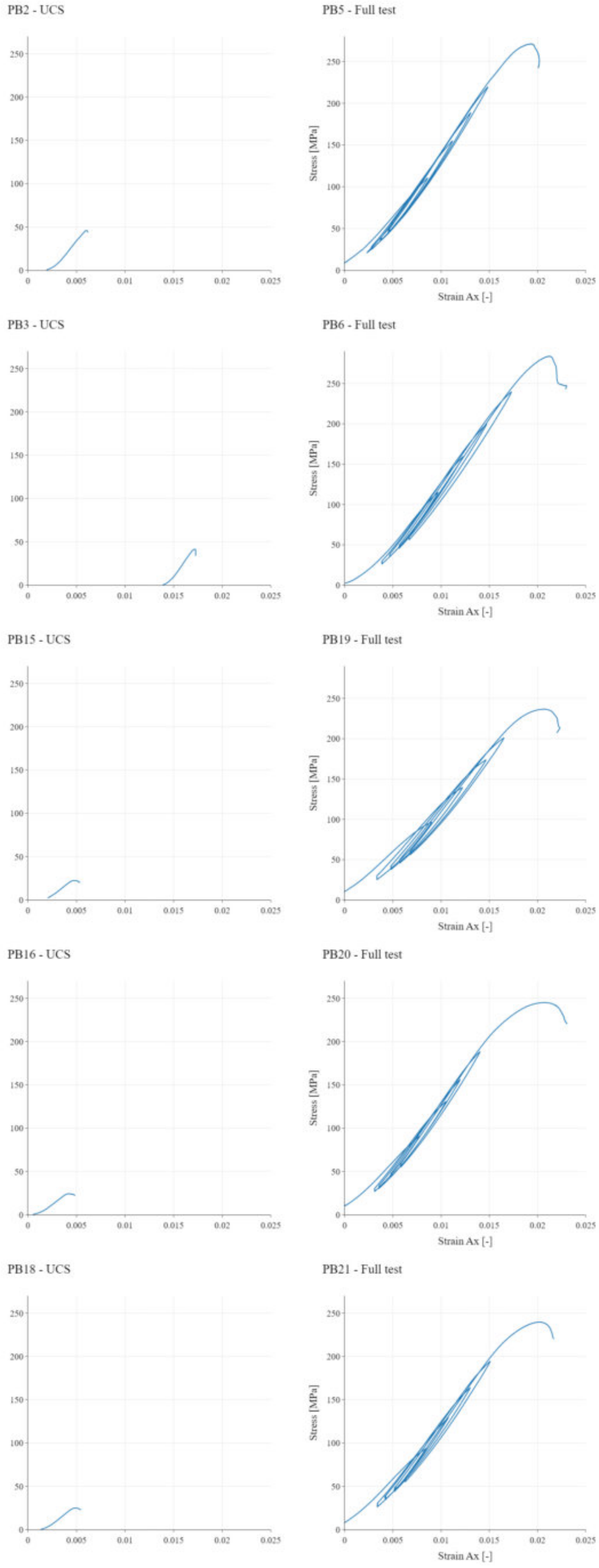

Figure B.4: Stress vs Strain plots of German samples

C Depth related plots

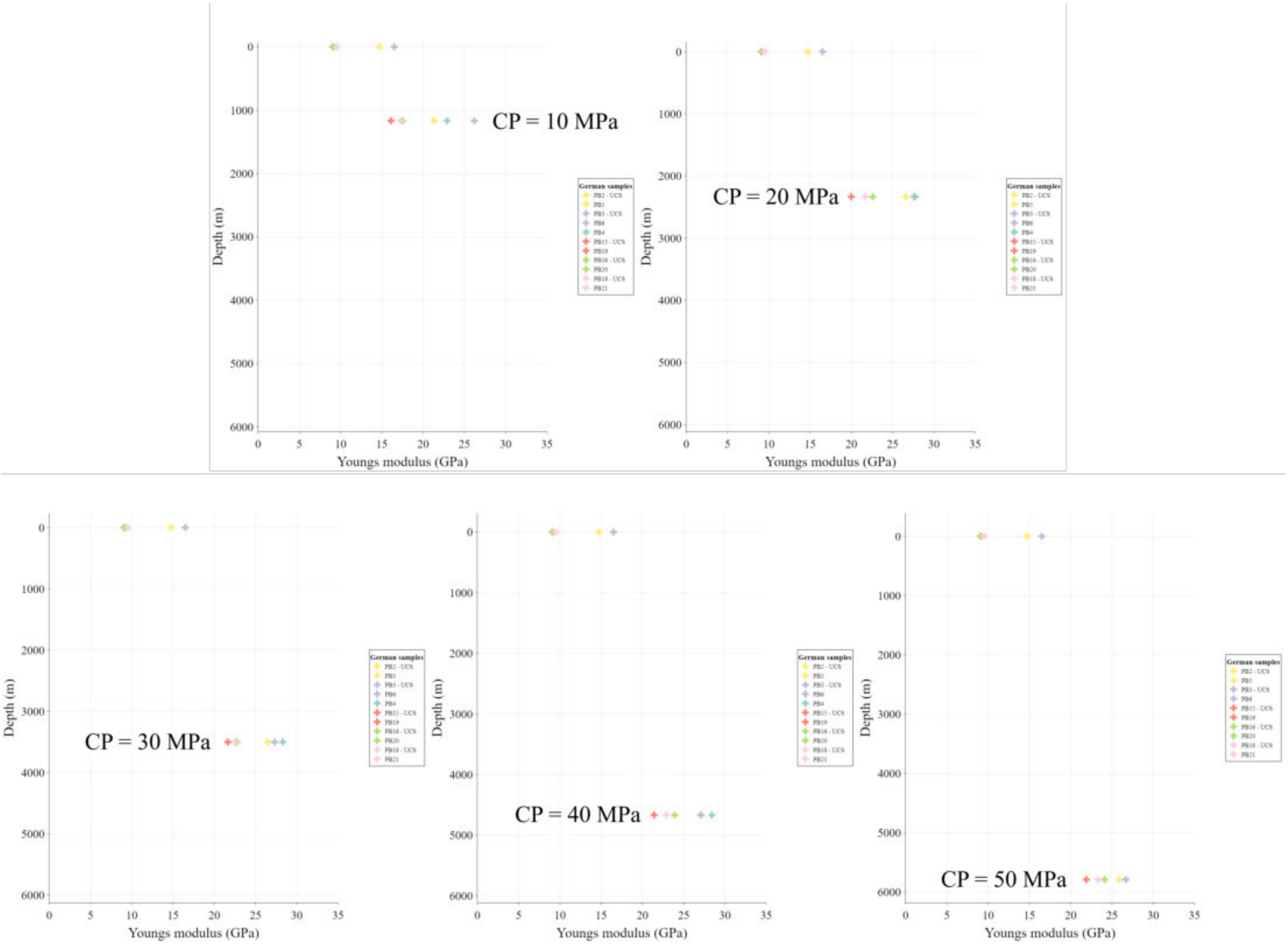

Figure C.1: Depth vs Young's modulus plots of German samples based on the different confining pressures. Depth - CP relation obtained from Douma et al. 2019

D Mohr Coulomb envelopes

D.1 Failure envelopes

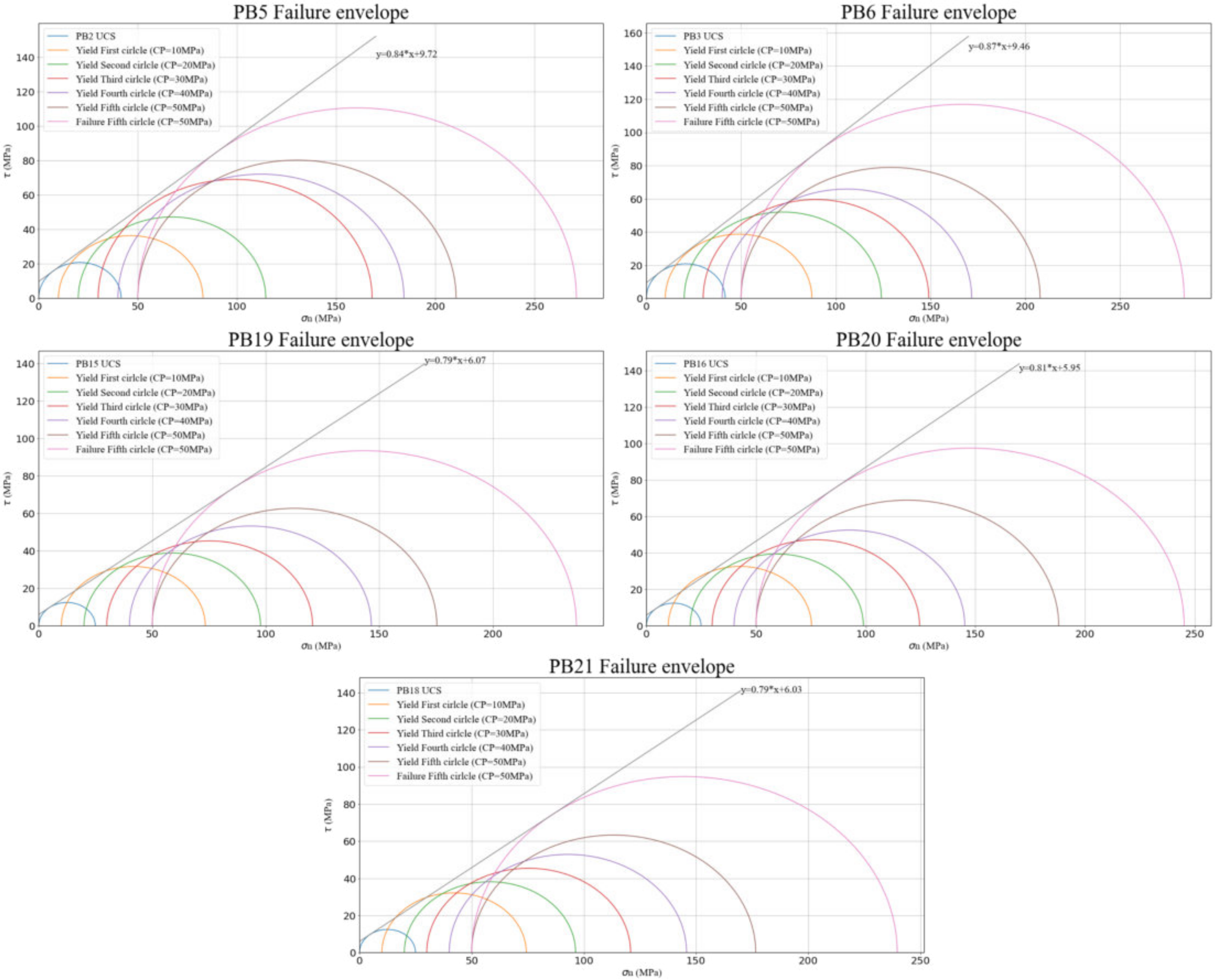

PB5 Failure envelope

PB6 Failure envelope

PB19 Failure envelope

PB20 Failure envelope

PB21 Failure envelope

Figure D.1: Mohr Coulomb circles and failure envelope of the German samples. samples tested with UCS were correlated with the samples tested with the triaxial setup

D.2 Yield envelopes

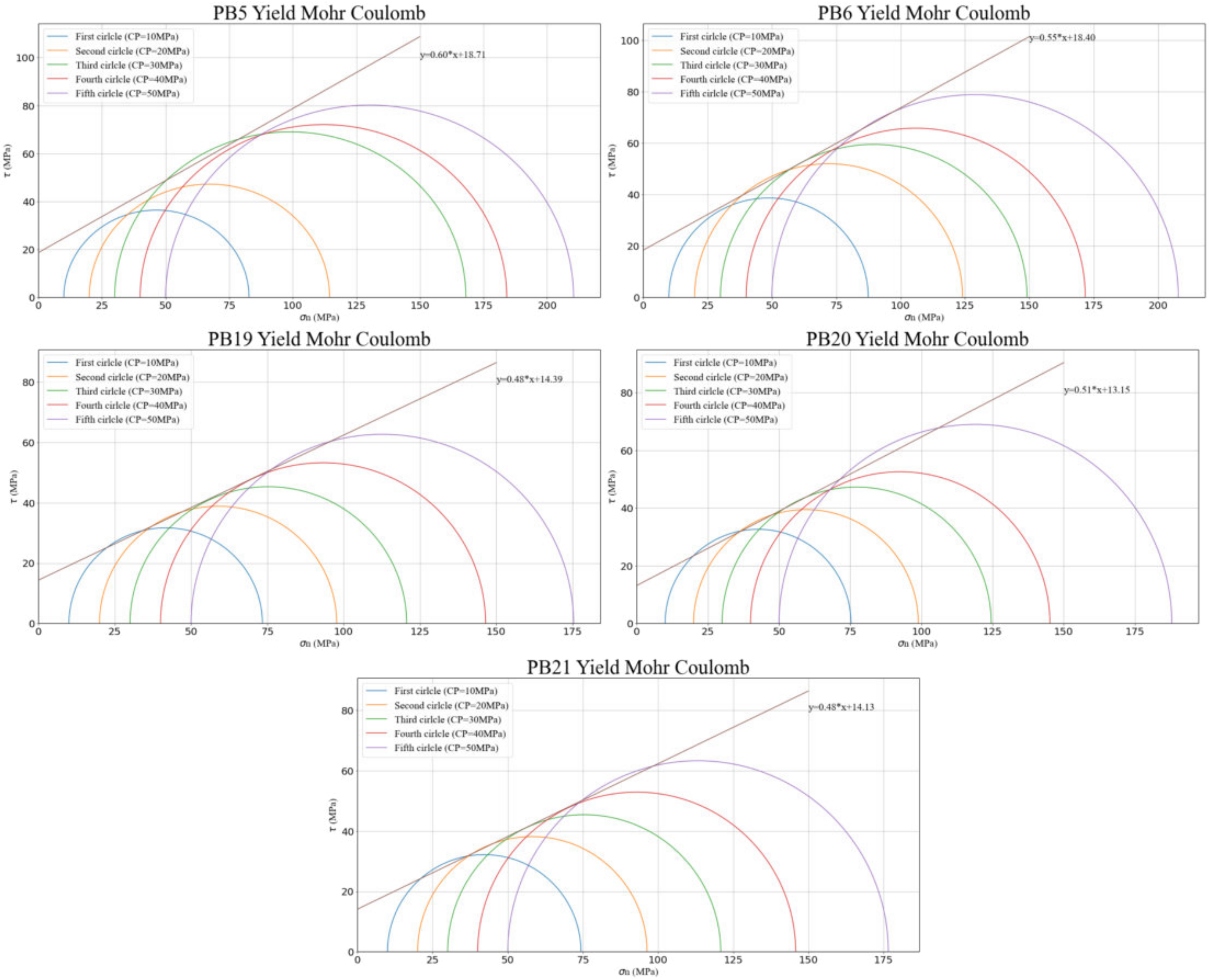

Figure D.2: Mohr Coulomb circles and yield envelope of the German samples

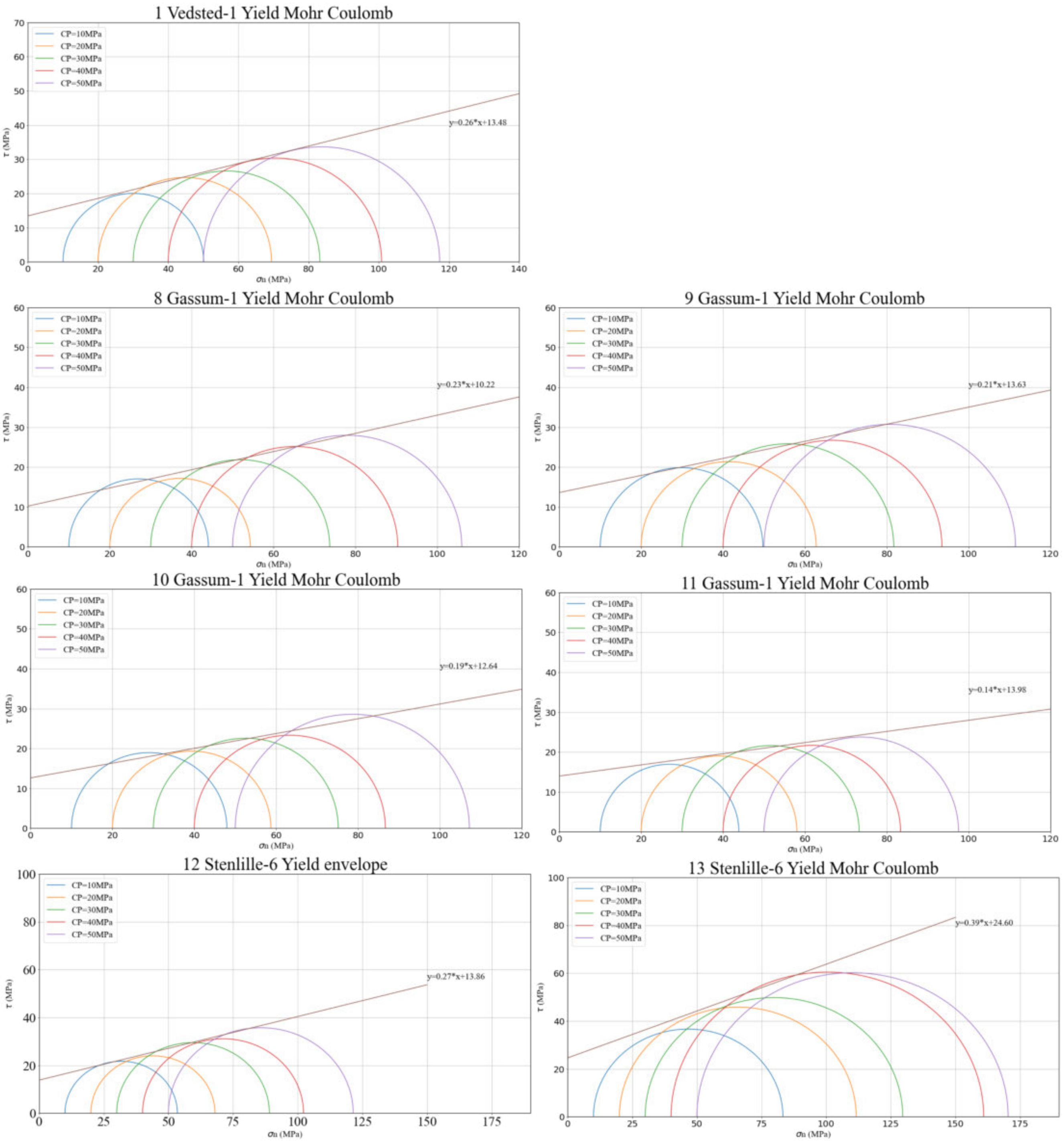

Figure D.3: Mohr Coulomb circles and yield envelope of the Danish samples

E Wave velocity

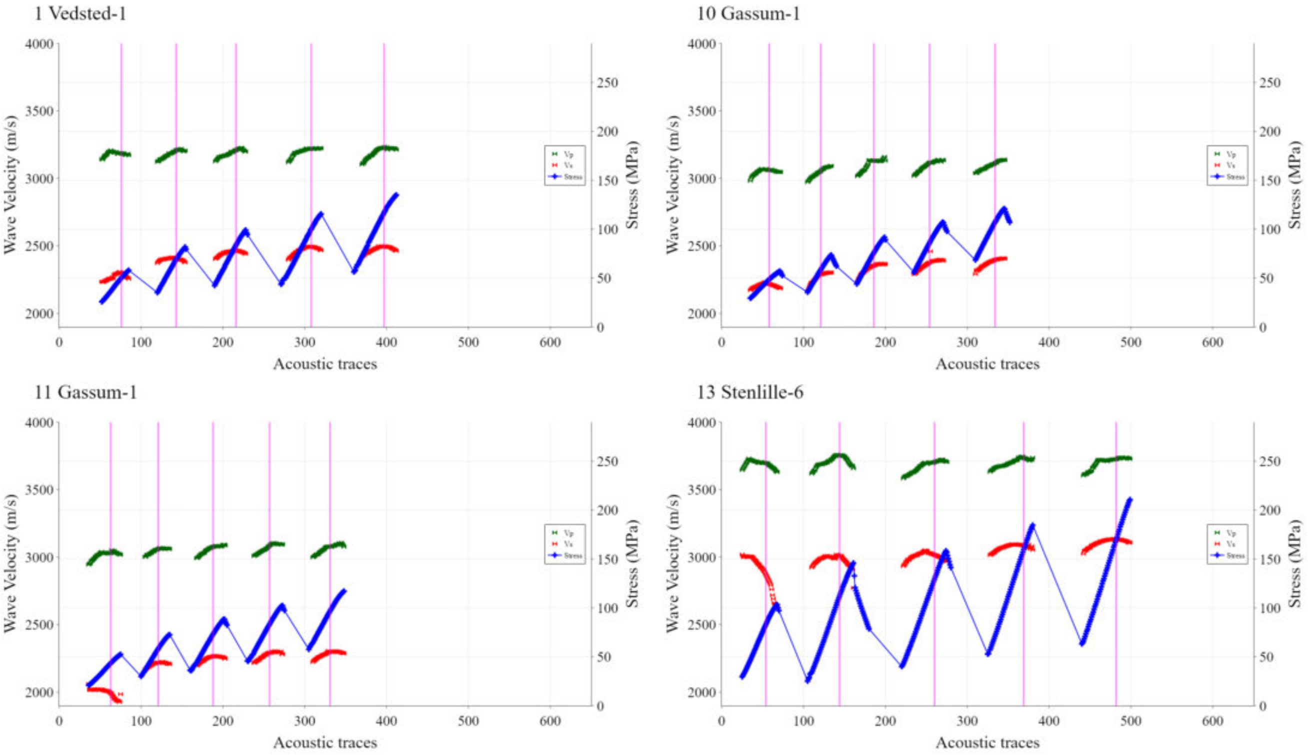

Figure E.1: Wave velocities and Axial Stress vs Acoustic traces of the Danish samples

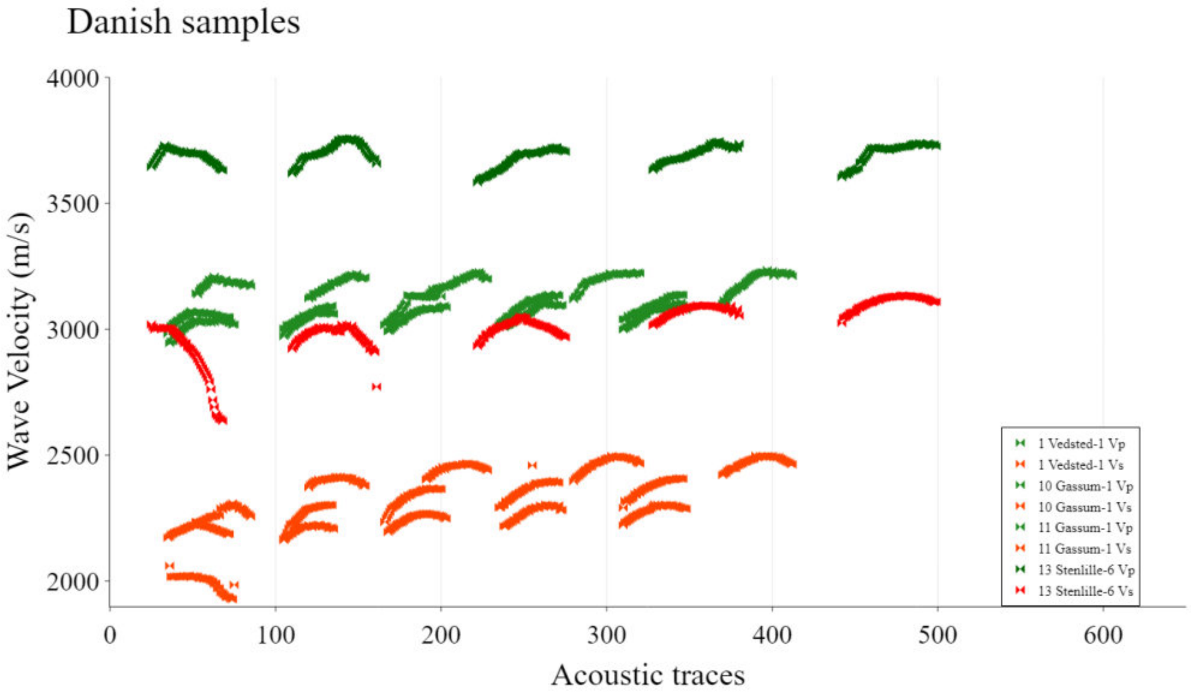

Figure E.2: Combination of the velocities vs Acoustic traces of the Danish samples

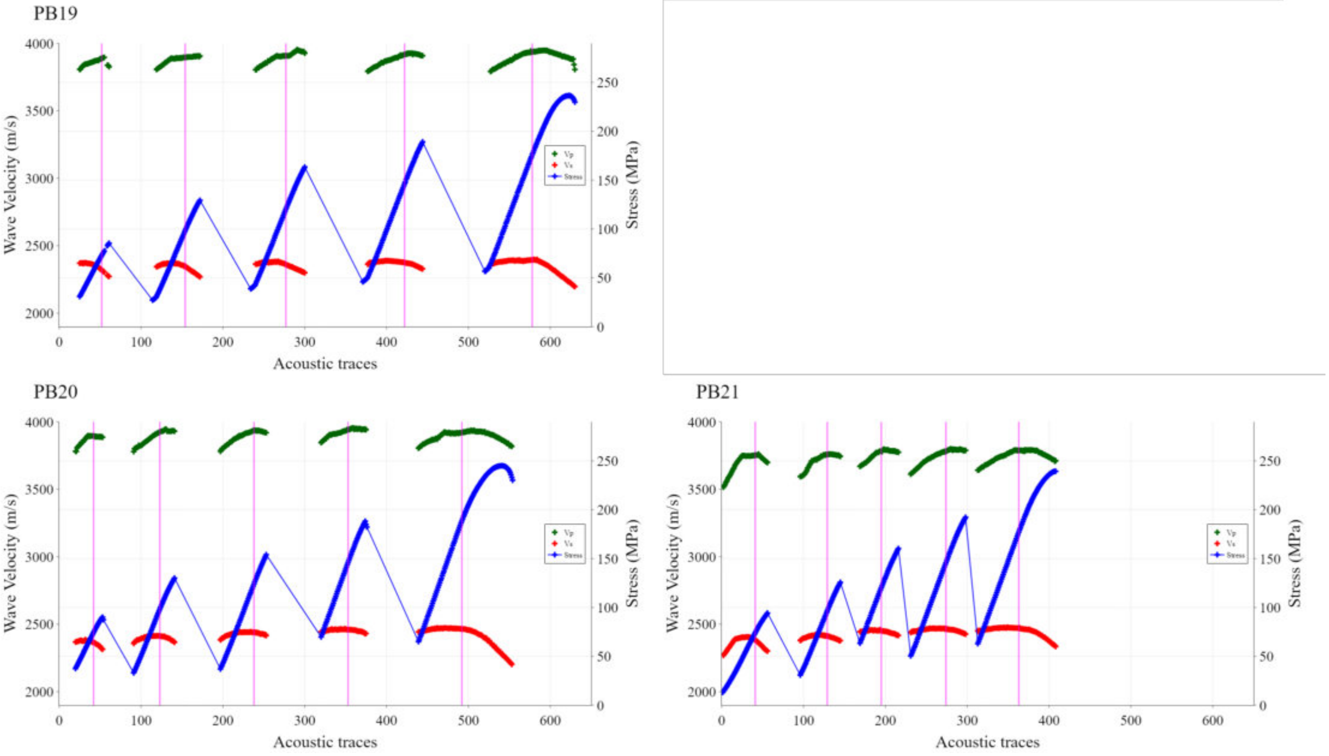

Figure E.3: Wave velocities and Axial Stress vs Acoustic traces of the German samples

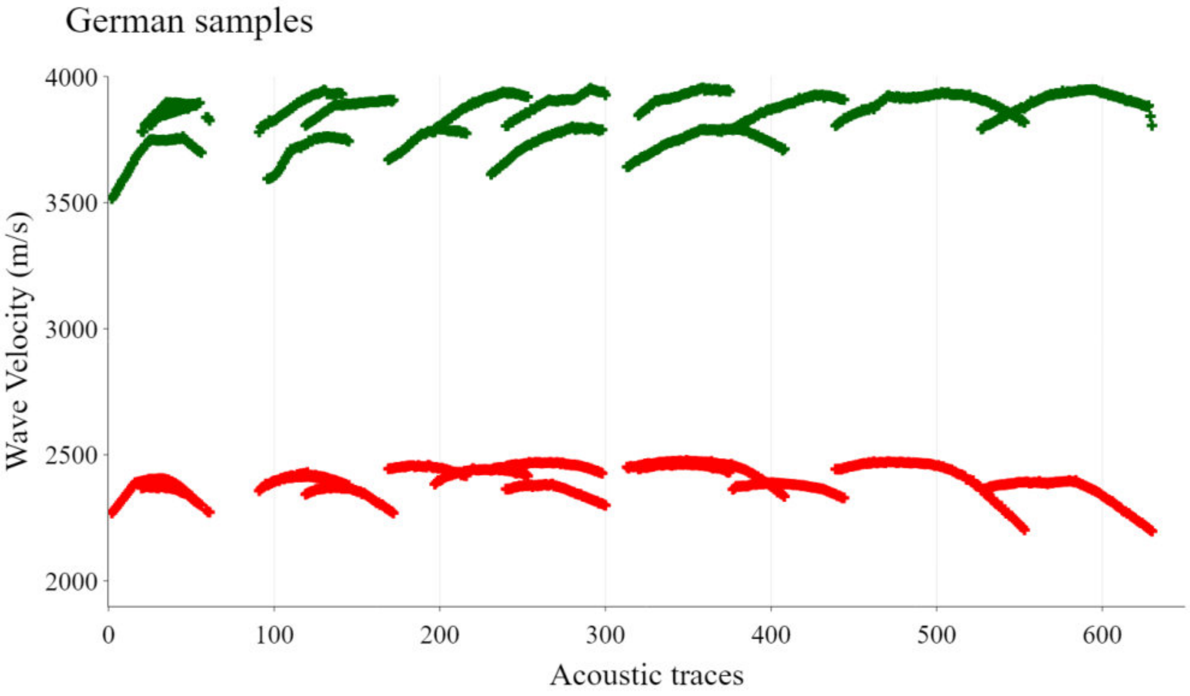

Figure E.4: Combination of the velocities vs Acoustic traces of the German samples

F Micro CT imaging

Danish Sample 1

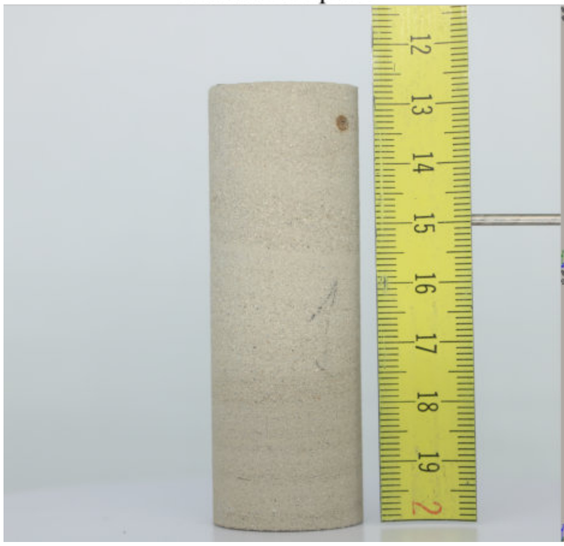

Region of interest

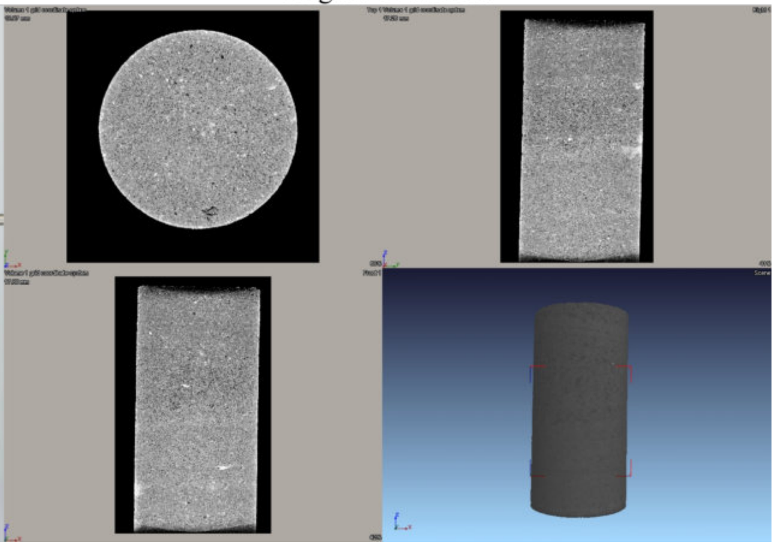

Connected void space

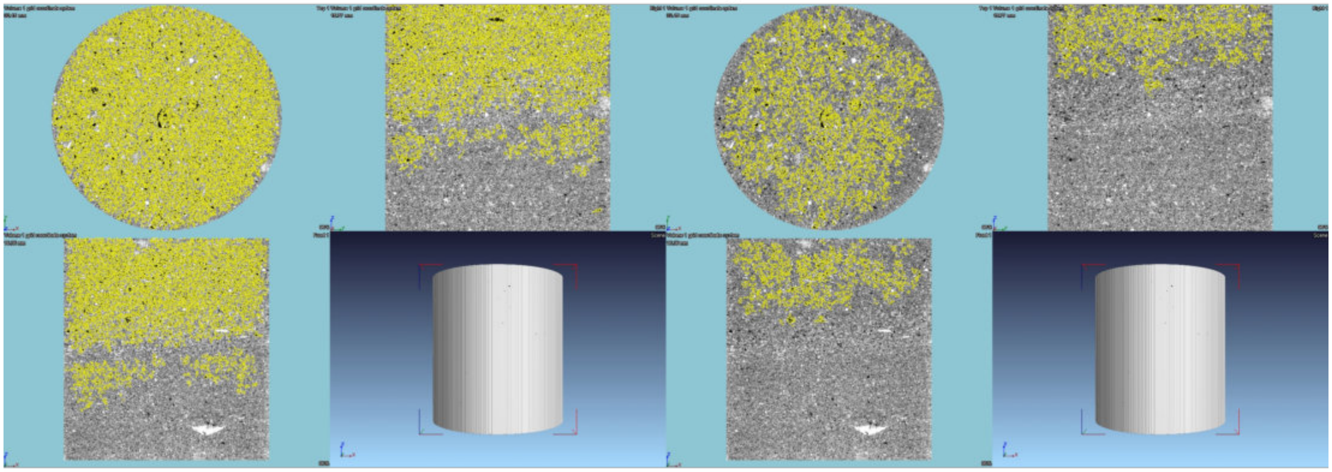

Tolerance = 1000

Tolerance = 900

Danish Sample 8

Region of interest

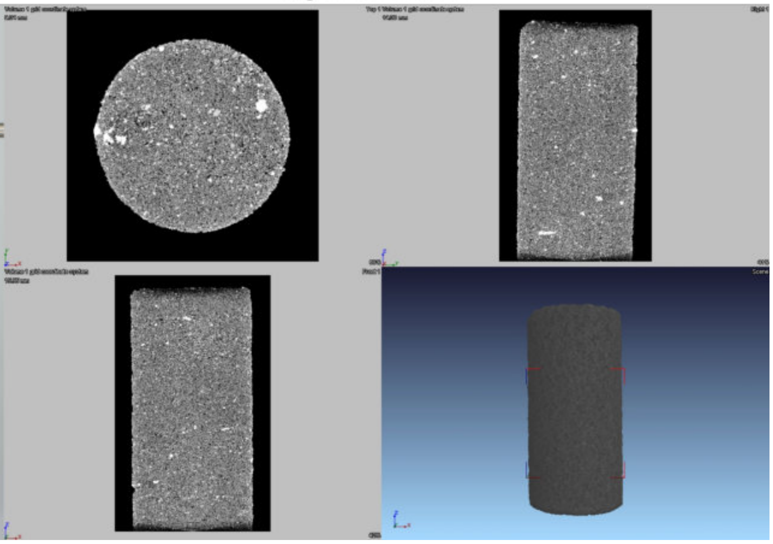

Connected void space

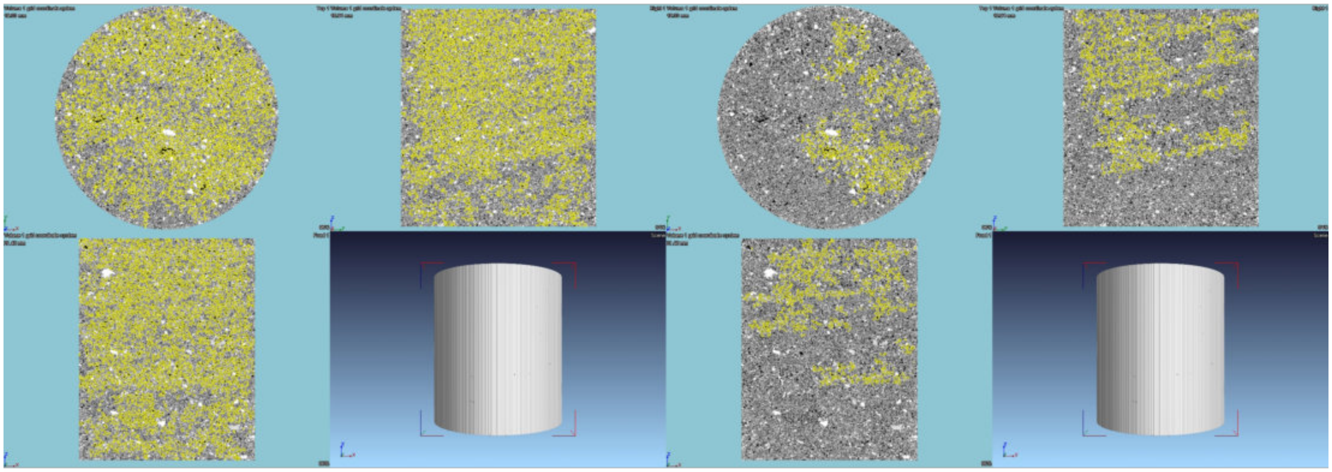

Tolerance = 800

Tolerance = 700

Danish Sample 12

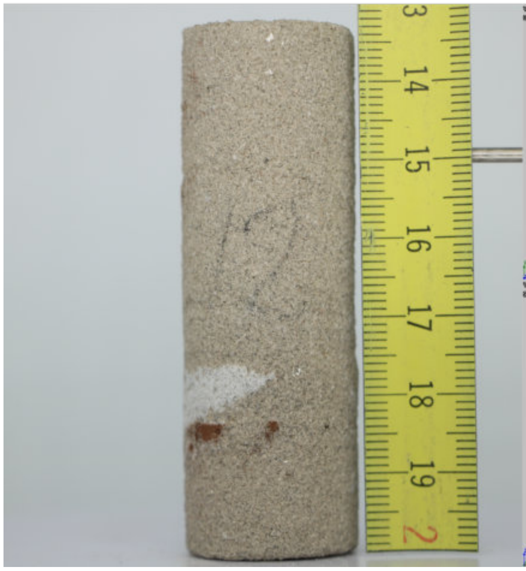

Region of interest

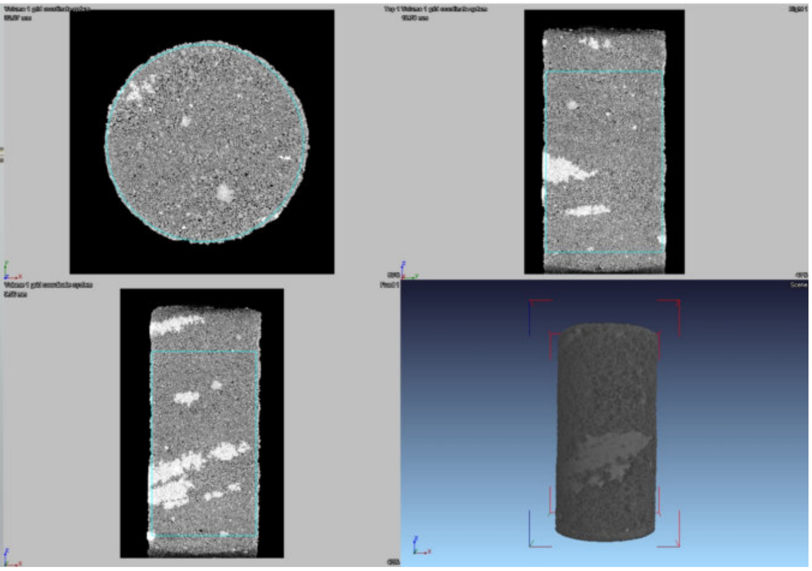

Connected void space

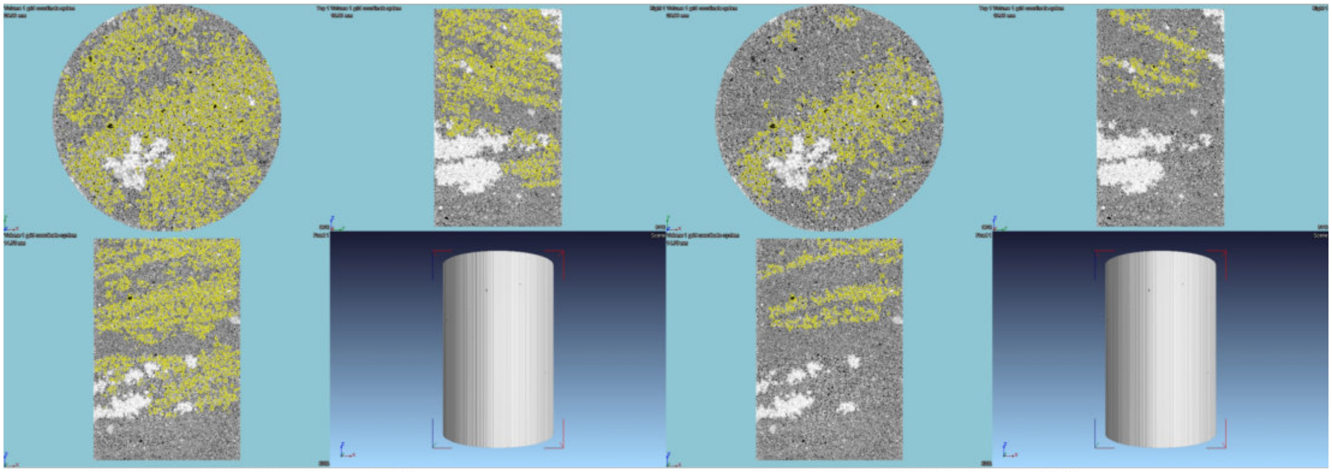

Tolerance = 1300

Tolerance = 1200

Danish Sample 13

Region of interest

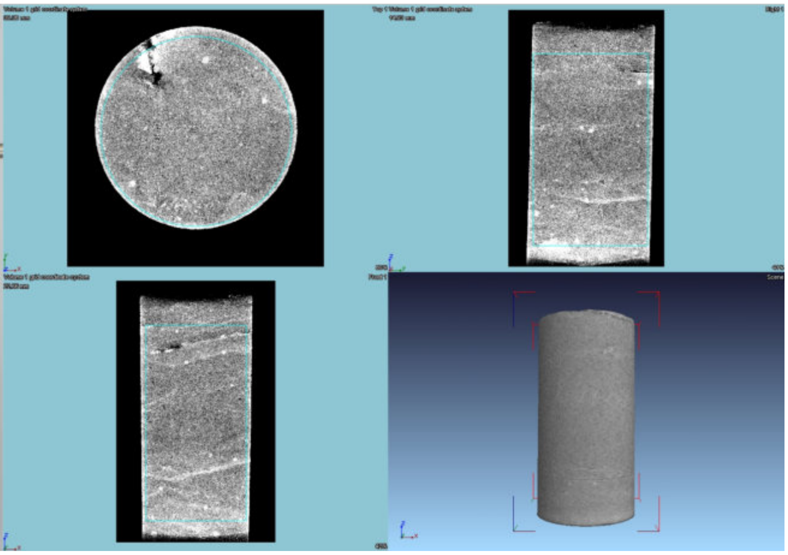

Connected void space

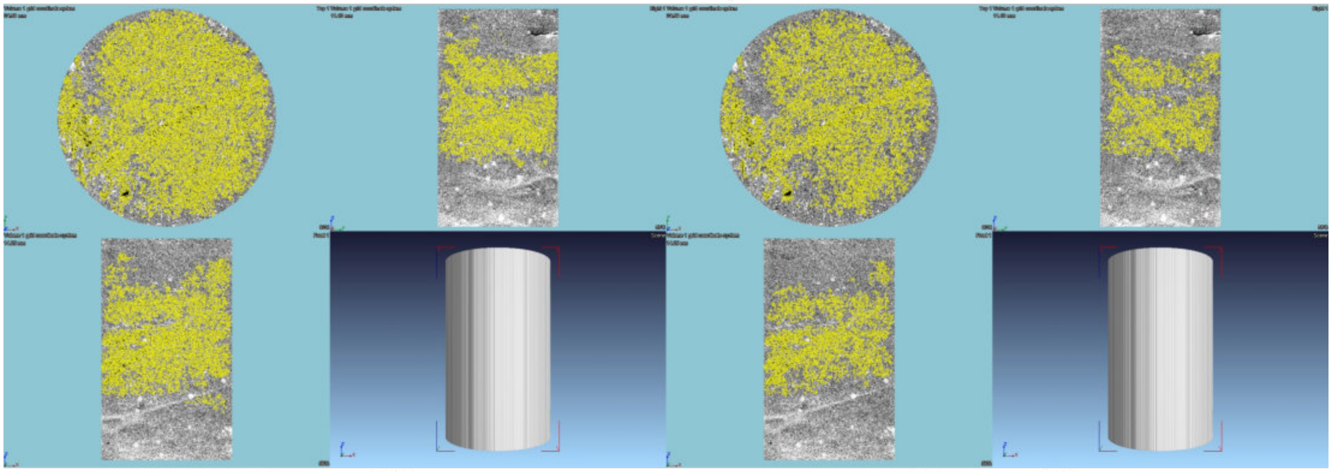

Tolerance = 1200

Tolerance = 1100

Danish Sample 117

Region of interest

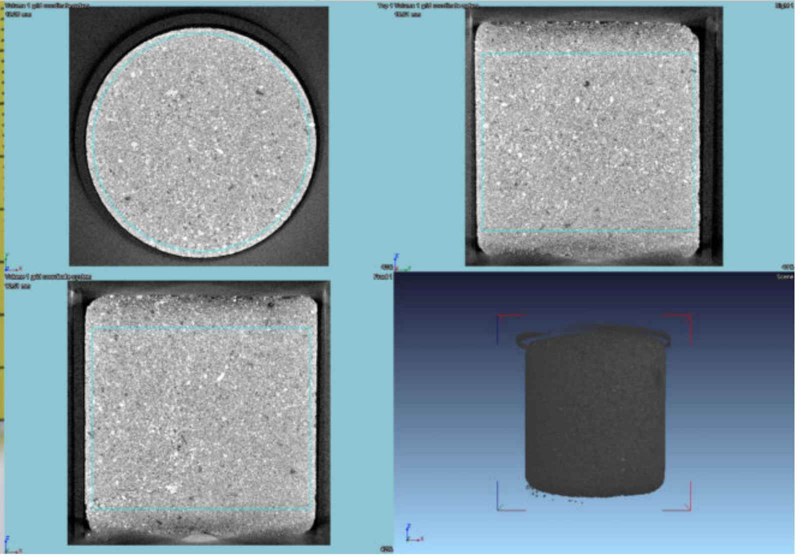

Connected void space

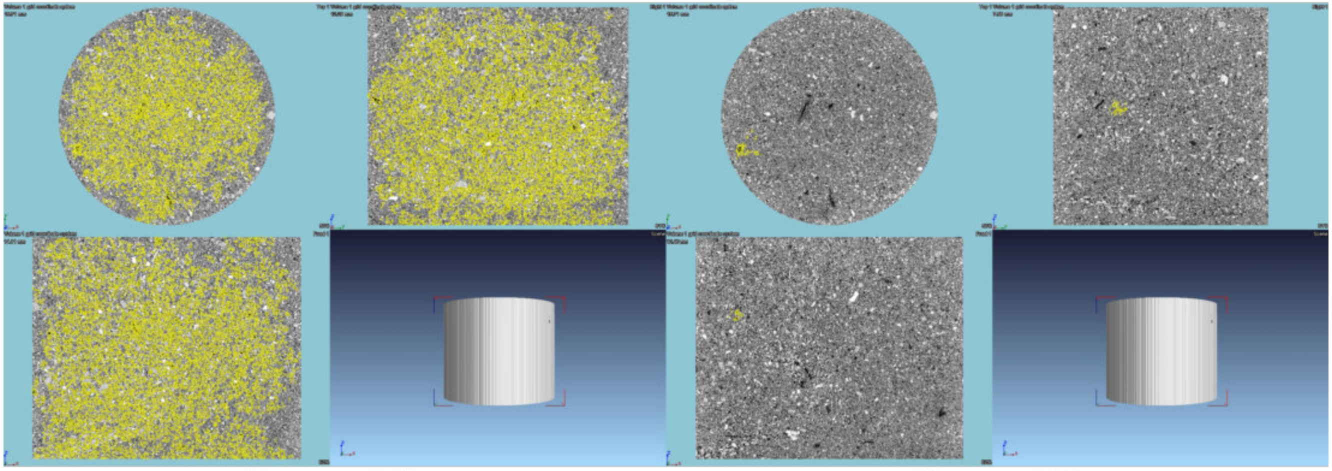

Tolerance = 1200

Tolerance = 1100

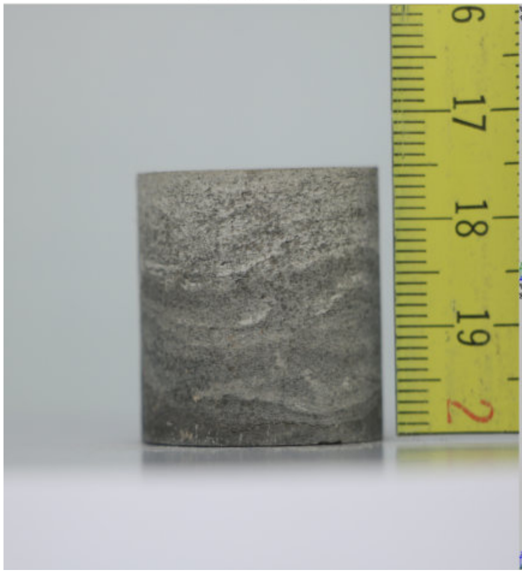

Danish Sample 137

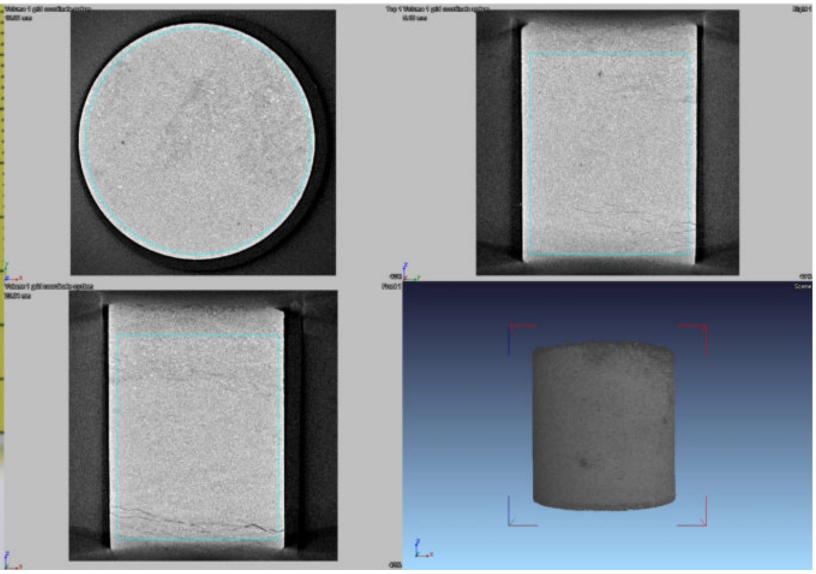

Region of interest

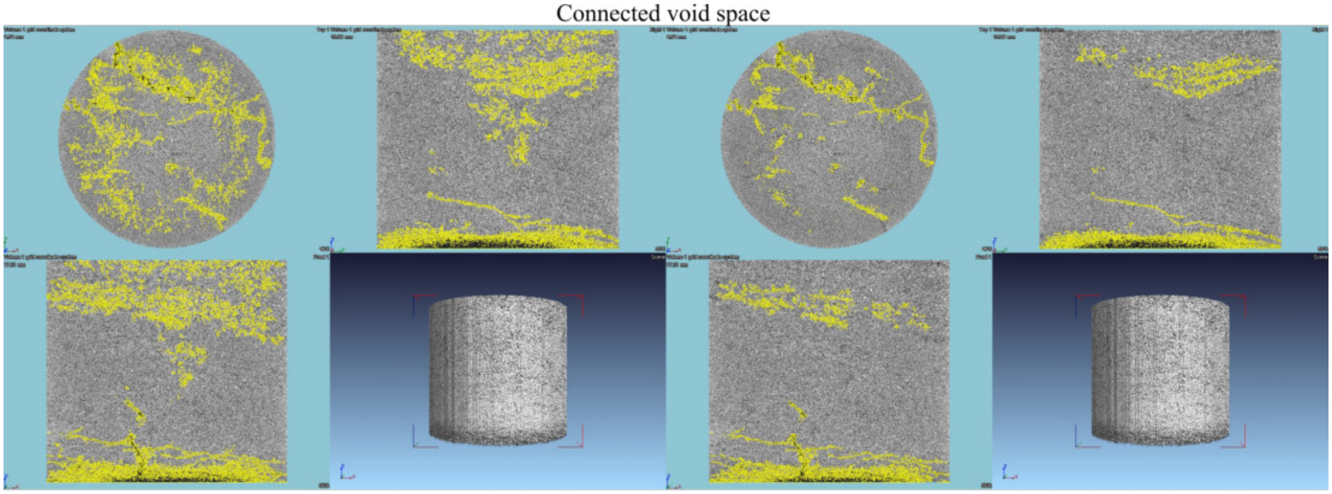

Connected void space

Tolerance = 1200

Tolerance = 1100

G Pictures

G.1 Danish samples

Figure G.1: Sample 1

Figure G.2: Sample 2

Figure G.3: Sample 3

Figure G.4: Sample 4

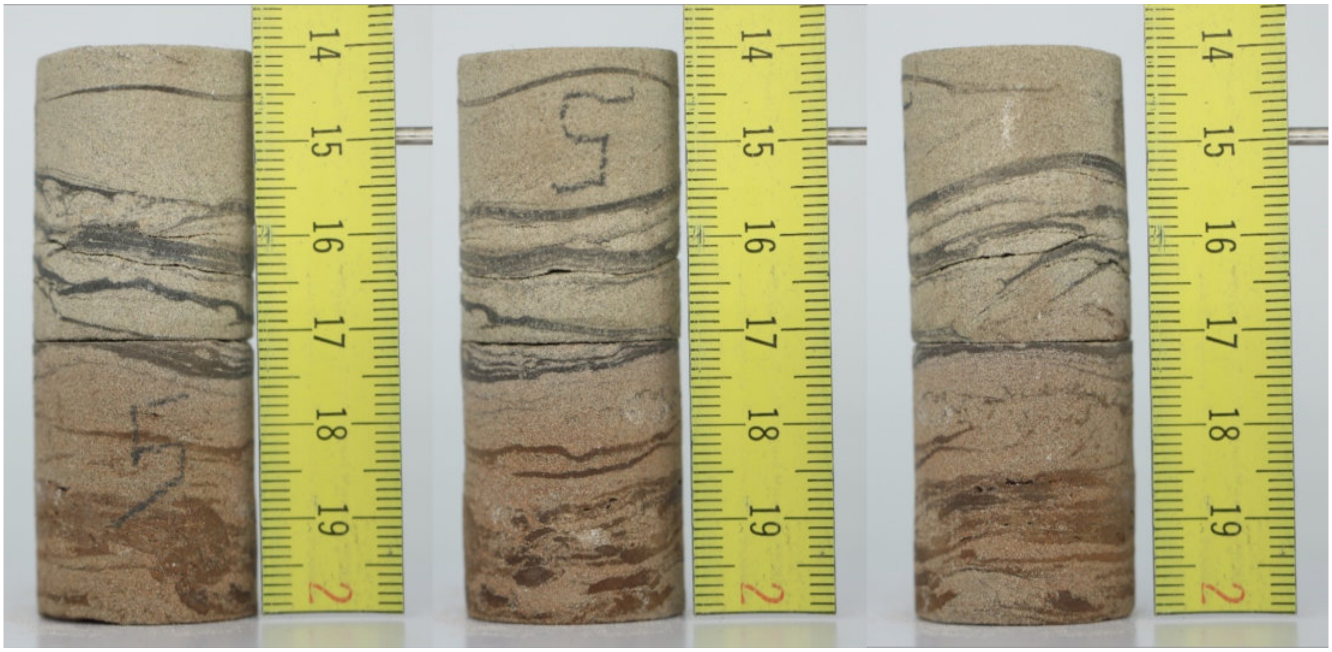

Figure G.5: Sample 5

Figure G.6: Sample 6

Figure G.7: Sample 7

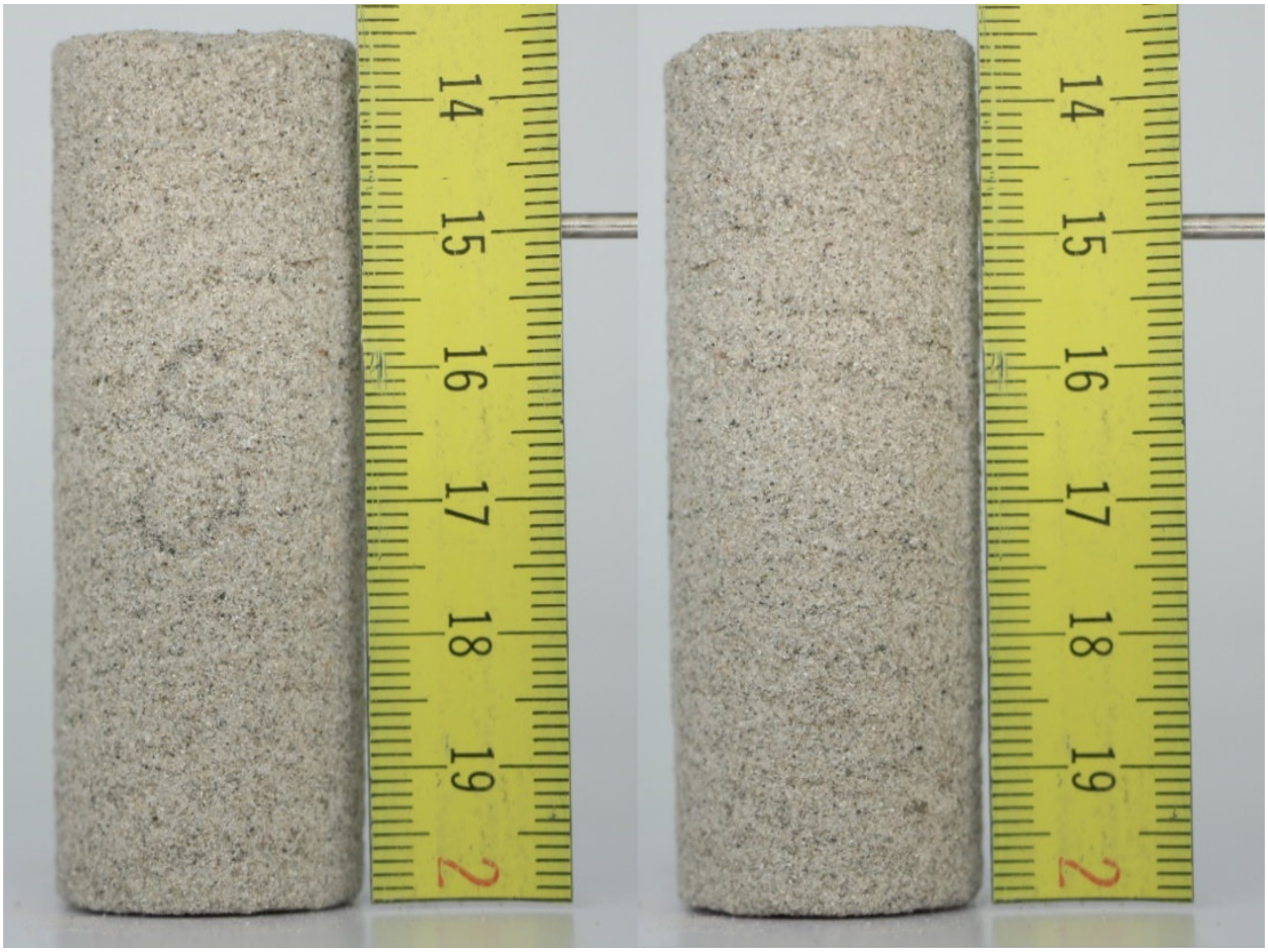

Figure G.8: Sample 8

Figure G.9: Sample 9

Figure G.10: Sample 10

Figure G.11: Sample 11

Figure G.12: Sample 12

Figure G.13: Sample 13

Figure G.14: Sample 109

Figure G.15: Sample 117

Figure G.16: Sample 133

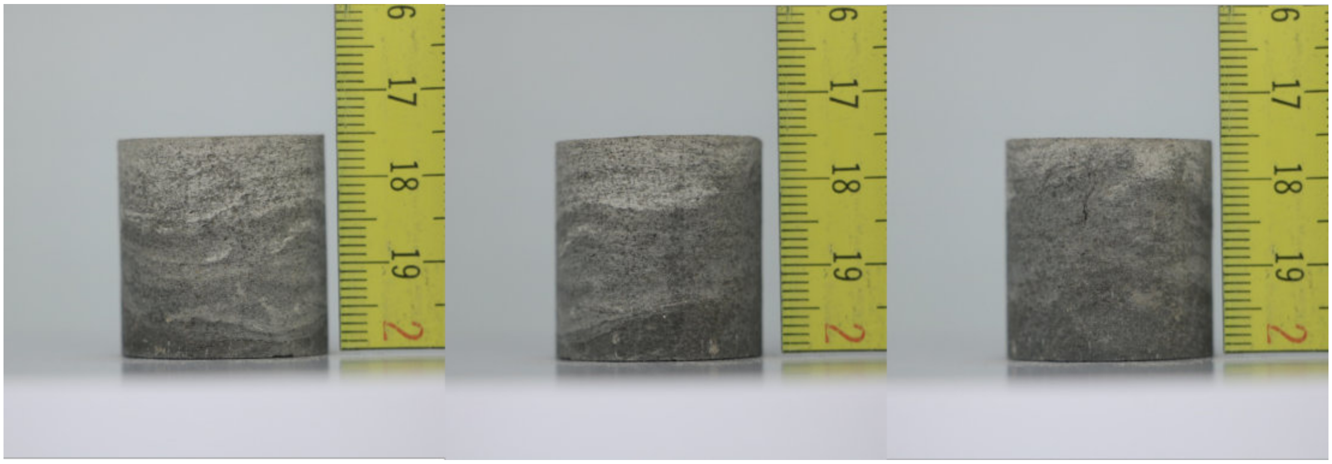

Figure G.17: Sample 137

Figure G.18: Sample 145

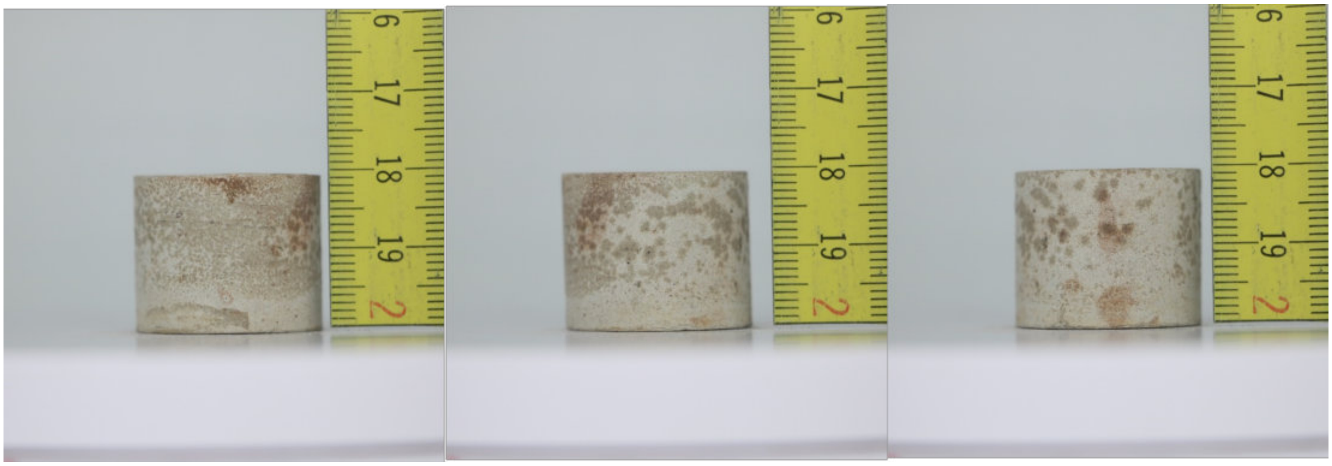

Figure G.19: Sample 201

Figure G.20: Sample 221

G.2 Norwegian samples

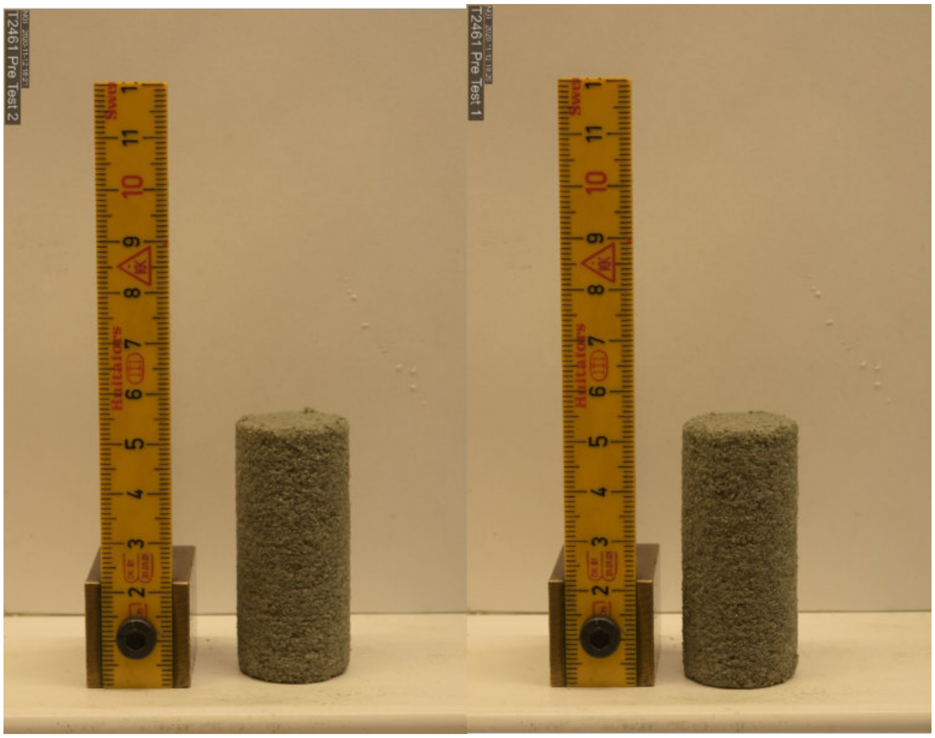

Figure G.21: Sample T2461

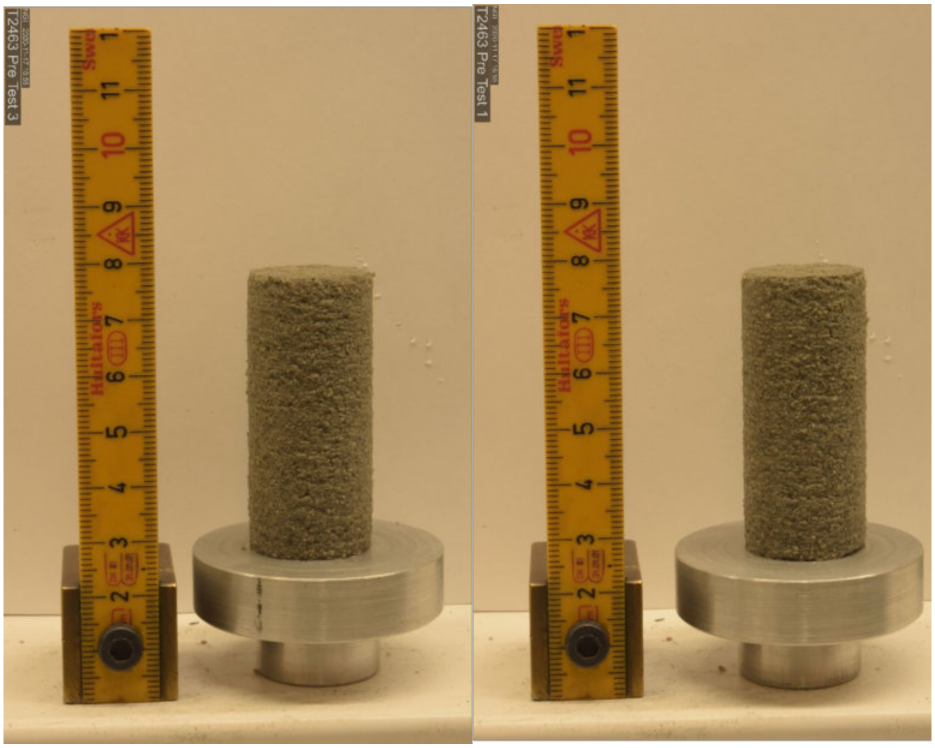

Figure G.22: Sample T2463

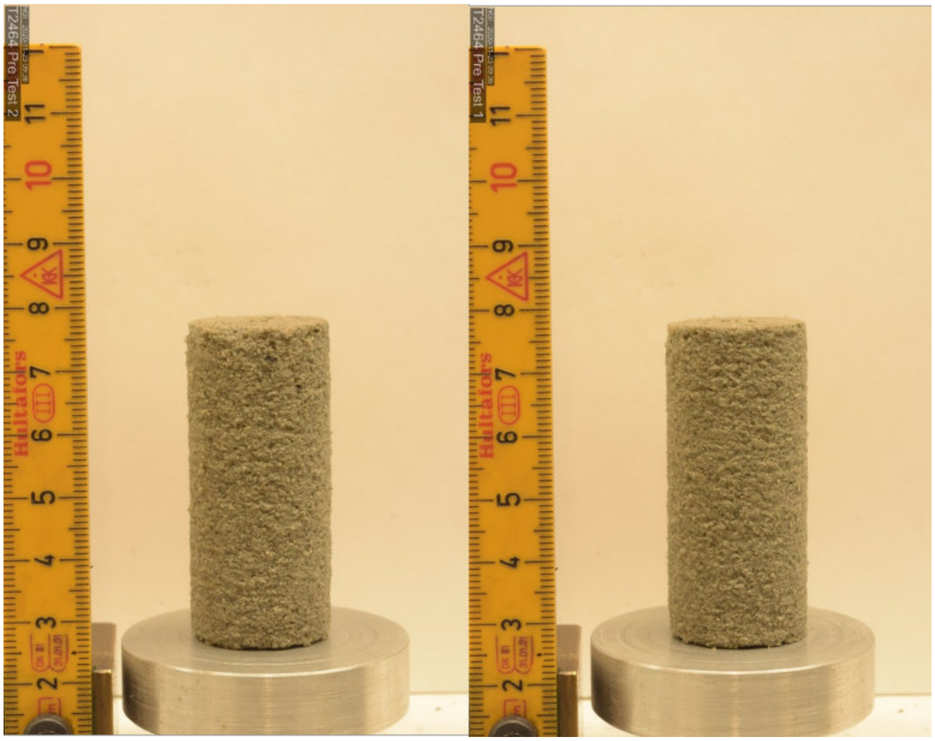

Figure G.23: Sample T2464

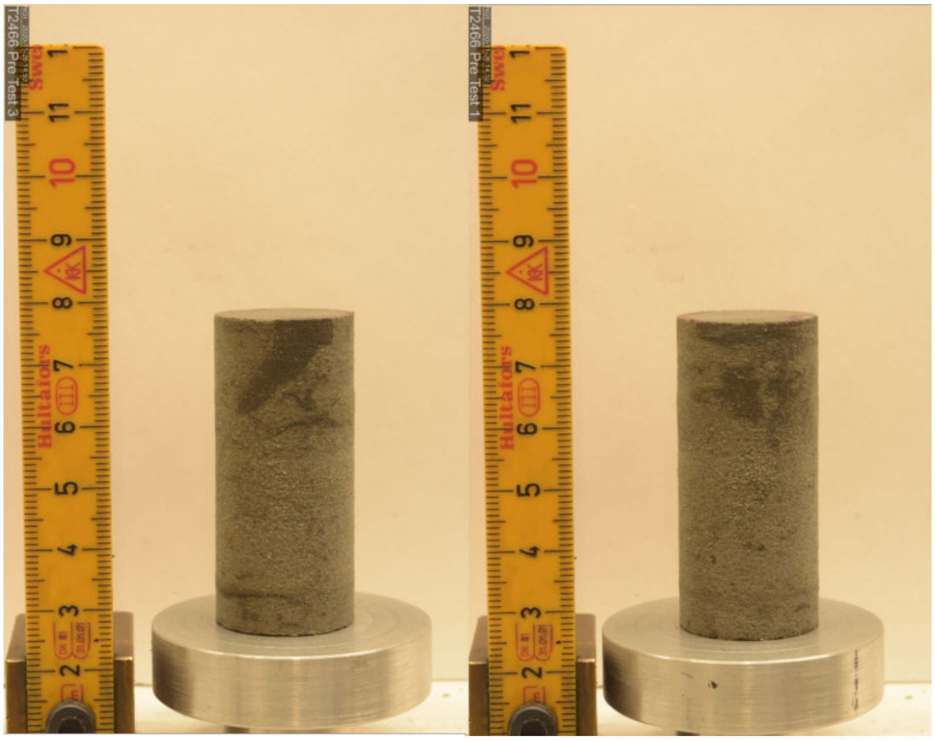

Figure G.24: Sample T2466

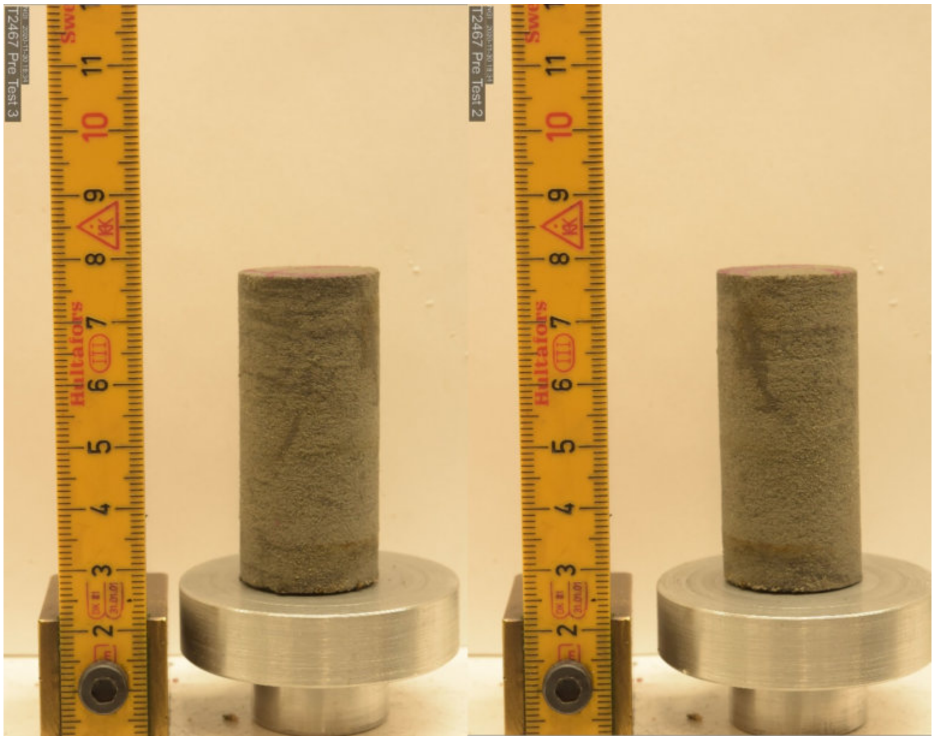

Figure G.25: Sample T2467

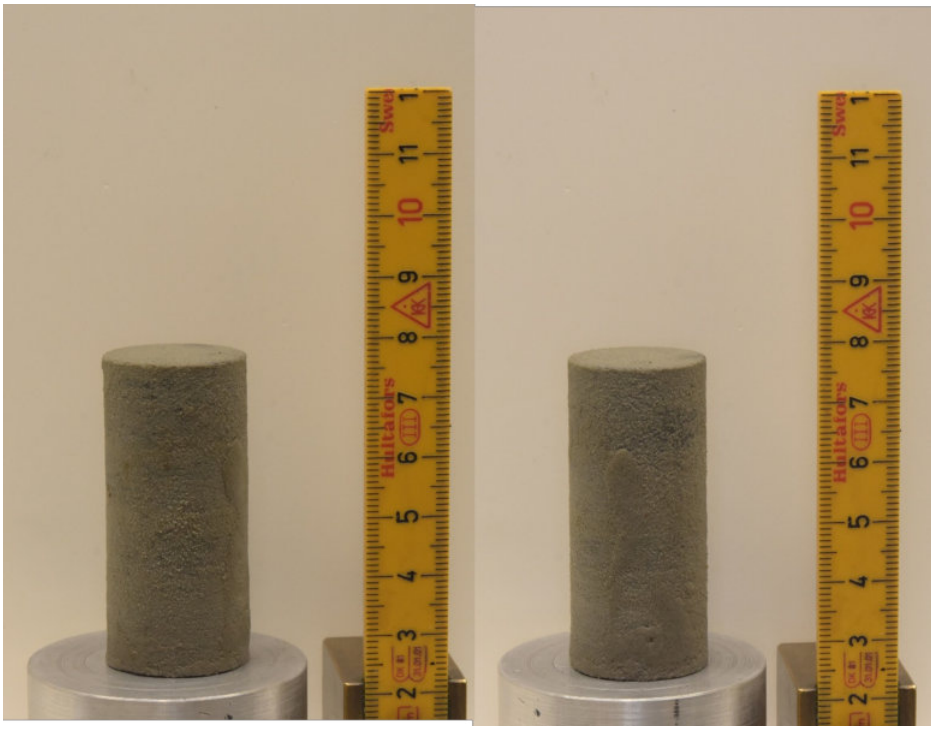

Figure G.26: Sample T2469

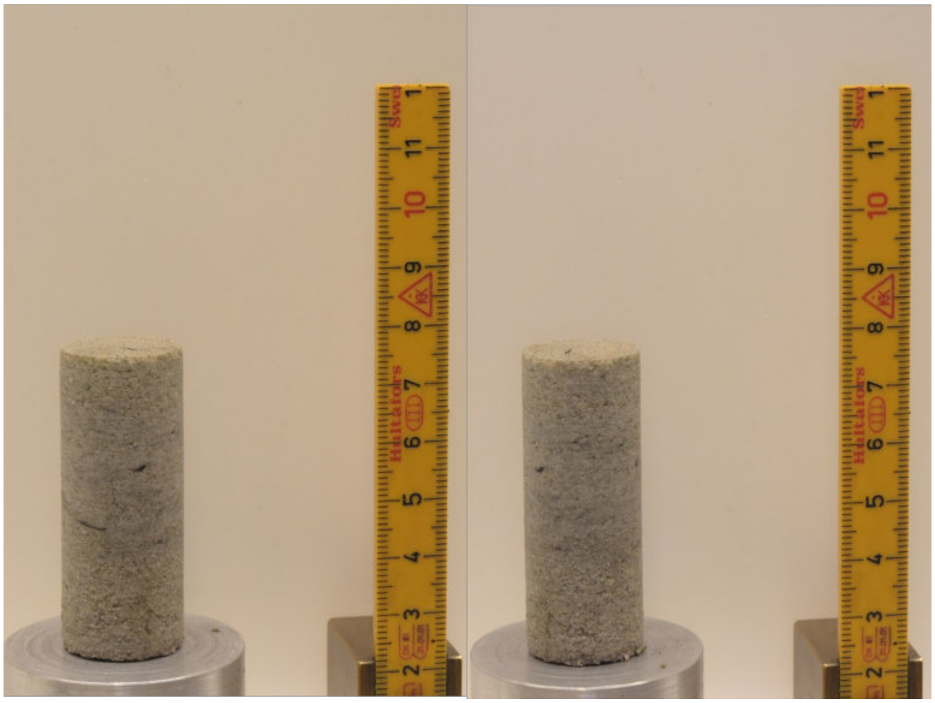

Figure G.27: Sample T2470

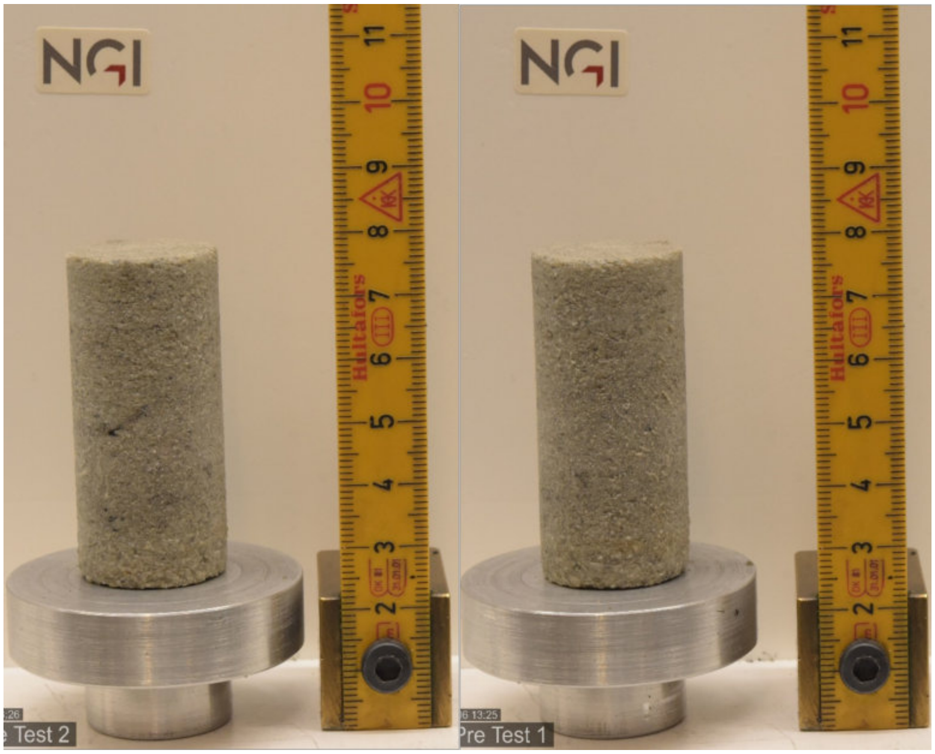

Figure G.28: Sample T2472

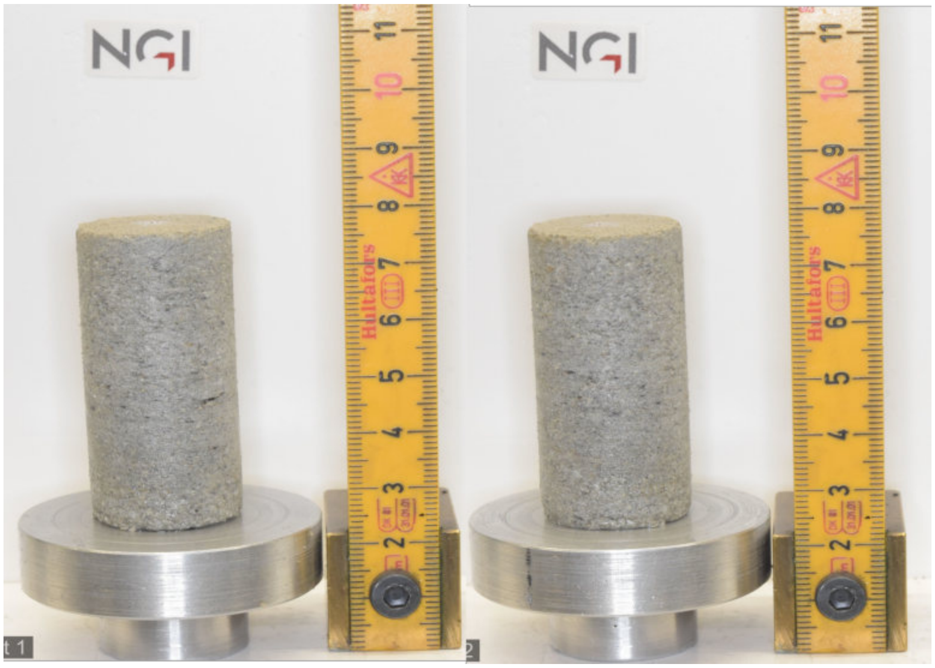

Figure G.29: Sample T2476

G.3 Machines

Figure G.30: Coring machine. Cores being made to the Red Felser sandstone block from Germany

Figure G.31: Saw machine Qcut 400 A

Figure G.32: Oven used to dry the samples. Temperature = 60°C

Figure G.33: Helium pycnometer used to measure the volume and density of the dried samples before testing

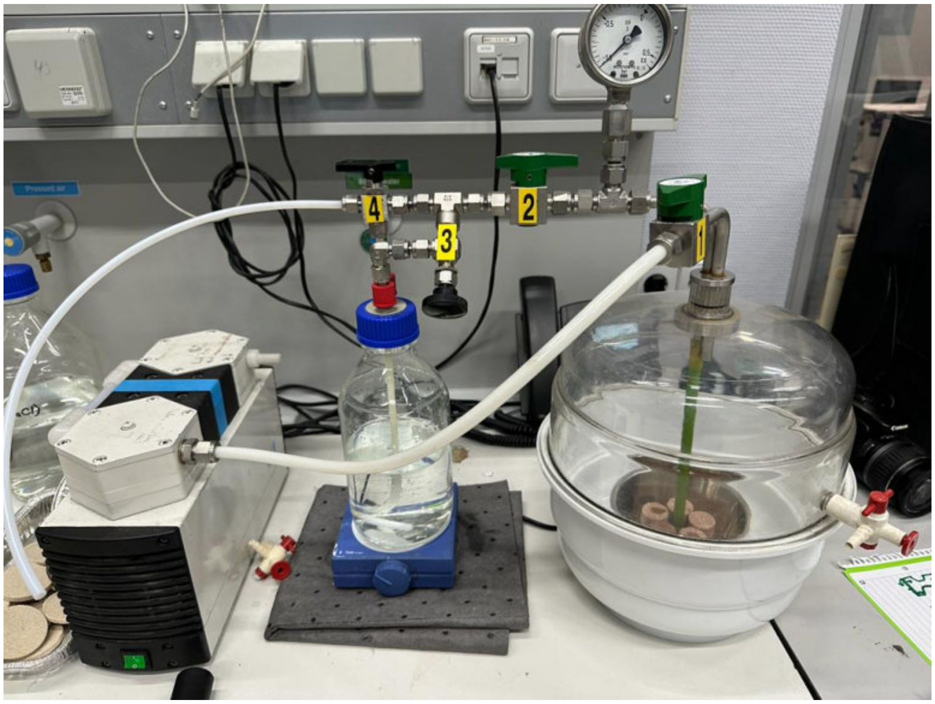

Figure G.34: Vaccum chamber where samples were saturated with tap water

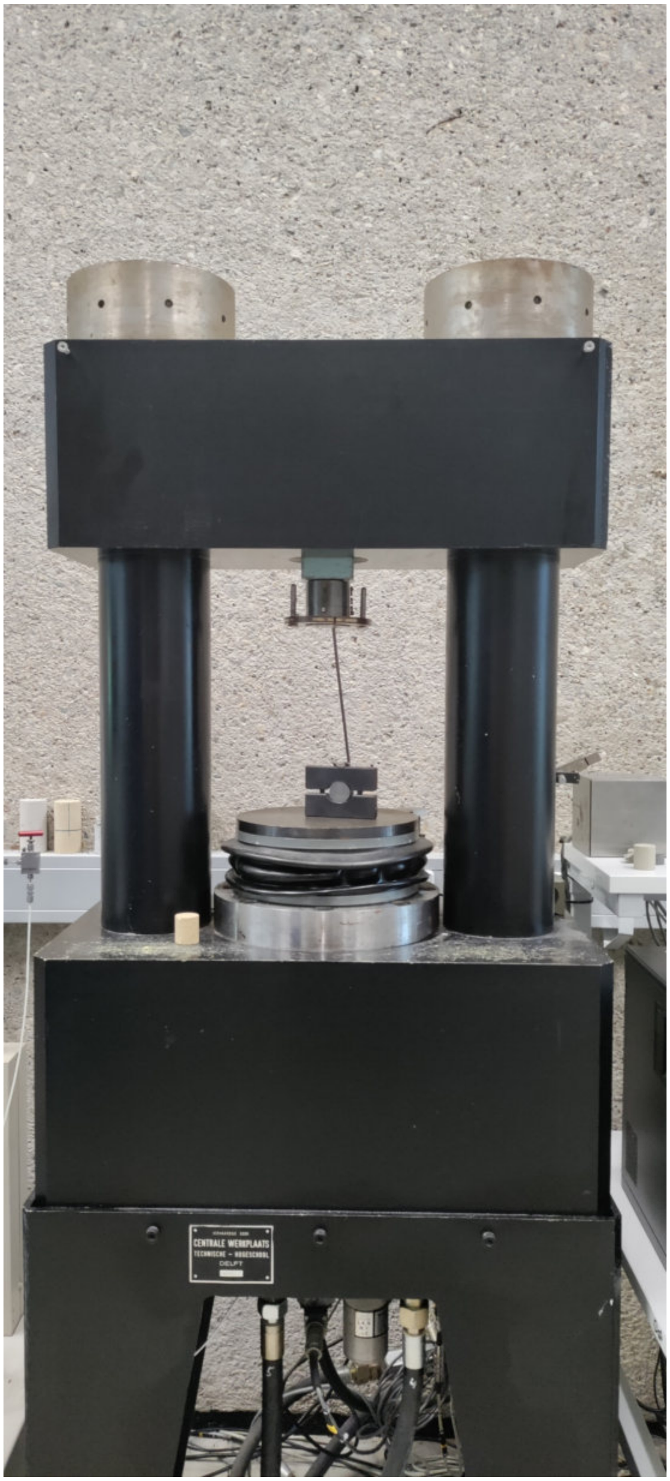

Figure G.35: UCS 50kN machine used for Brazilian tests

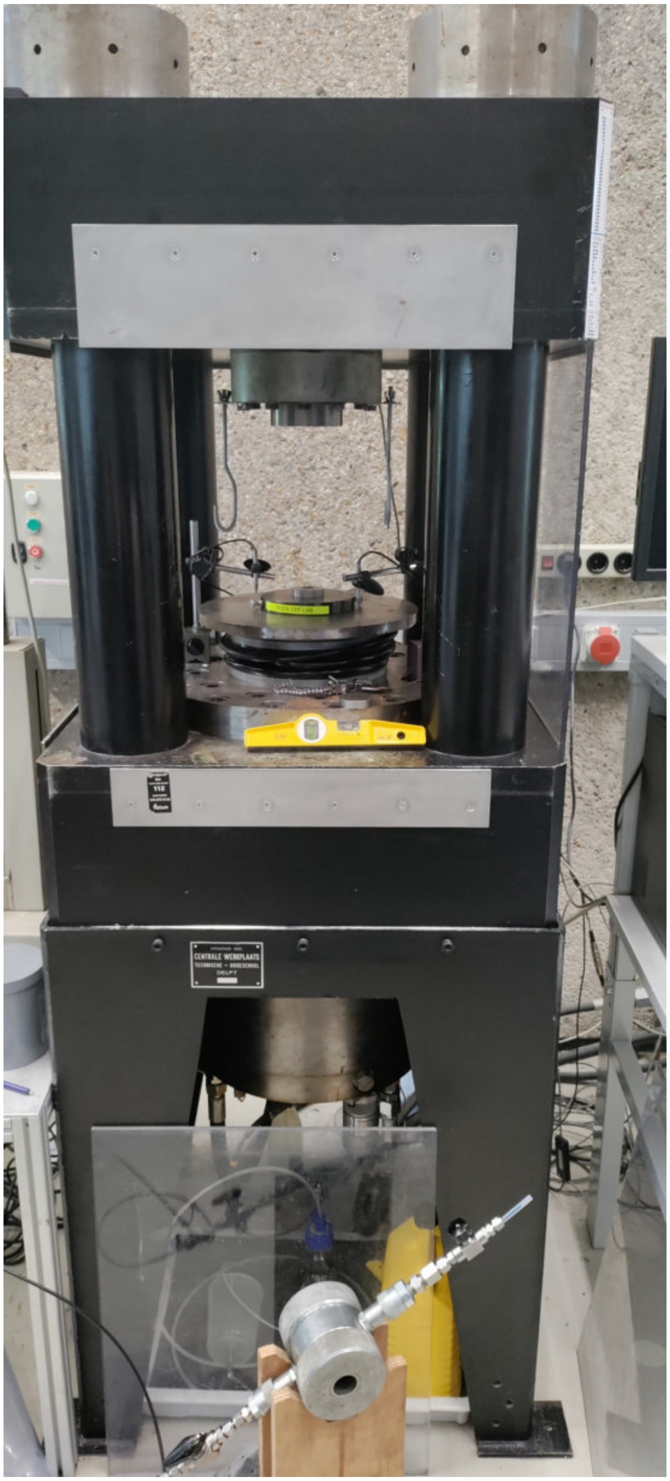

Figure G.36: UCS 500kN machine used for UCS and Triaxial tests